8-2000

Theoretical Prediction of Nuclear Quadrupole Resonance Spectra of Aluminum, Bromine and Nitrogen Compounds via First Principles Calculations

Chris Harwell
Louisiana State University and Agricultural and Mechanical College

Follow this and additional works at: https://repository.lsu.edu/gradschool_disstheses

THEORETICAL PREDICTION OF NUCLEAR QUADRUPOLE RESONANCE SPECTRA OF ALUMINUM, BROMINE AND NITROGEN COMPOUNDS VIA FIRST PRINCIPLES CALCULATIONS

A Dissertation

Submitted to the Graduate Faculty of the
Louisiana State University and
Agricultural and Mechanical College
in partial fulfillment of the
requirements for the degree of
Doctor of Philosophy

in

The Department of Chemistry

by
Chris Harwell
B.S., High Point University, 1996
August 2000

©2000

Chris Robert Harwell

To my senior editor and friend April Kabbash.

ACKNOWLEDGMENTS

I acknowledge the following people for their contributions to my research and this work:

- Randy Hall, Les Butler, Neil Kestner, Britt Thomas, Joel Tohline

- Rich Kurtz, Frank Fronczek

- Pam Bryant, Anthony Mrse, Earl Emery

- Andy Kolchin, Jose Gascon, Akilah Shelby, William Scullin, Sarah Hickey

- Jeff Rathbone

- April Kabbash

TABLE OF CONTENTS

ABSTRACT

We study the interaction of the electric field gradient (EFG) and the nuclear quadrupole moment of ^{81}Br, ^{27}Al and ^{14}N nuclei via *ab initio* quantum chemistry calculations. The primary goal is to predict the nuclear magnetic resonance (NMR) spectral parameters of interesting materials and assist in interpretation of their spectra. The calculations predict NMR spectral parameters for:

1. ^{27}Al nuclei in andalusite, sillimanite and kyanite – three polymorphs of Al_2SiO_5 – for assigning NMR signals to crystallographic sites, as a zeolite model and studying the effect of structural changes due to temperature $(25\text{-}1000^oC)$;

2. ^{14}N nuclei in tetryl and tetryl mimics to predict transition frequencies for the detection of explosives;

3. ^{81}Br nuclei in brominated aromatic flame retardants and models to assist in spectra interpretation for judging dispersal in high impact polystyrene;

4. ^{27}Al nuclei in cyclic $(N\text{-}Al)_x$ molecules for their similarity to the industrially important catalyst methyl-aluminum-oxane.

The calculations use standard quantum chemistry computer programs. We examine single molecules with molecular orbital (MO) theory and full crys-

tals with full potential linearized augmented plane wave (FP-LAPW) density functional theory. We also explore parts of full crystals by using MO theory for a small atom cluster and point charges for surrounding atoms. The MO calculations employ the restricted Hartree-Fock and the Becke's 3-parameter Lee-Yang-Parr hybridized density functional theory methods. We compare calculated spectral parameters among the different methods and with literature values acquired from experiment. The FP-LAPW method best predicts the spectral parameters and magnitudes, though it does rely on good quality crystal data being available. For MO theory a fairly large basis set of at least triple zeta quality with additional polarization and tight functions is necessary for accurate spectral parameters, and this method works well for single-molecules for which crystal data may not be available.

CHAPTER 1

INTRODUCTION

With this work we aim to advance materials analysis with predictions of spectral parameters. We evaluate electric-field-gradient (EFG) calculation methods for systems to which these methods have not been applied. It is important that these methods be carefully evaluated because EFGs are very difficult properties to calculate — they are extremely sensitive to structure and are themselves a stringent test of wavefunction quality.[1] We then predict nuclear magnetic resonance (NMR) and nuclear quadrupole resonance (NQR) spectral parameters via EFG calculations for systems of current world-wide interest. Specifically, predictions of spectral parameters enable highly useful materials analysis and imaging techniques.

Materials analysis and imaging is very important to public and industrial sectors involved in detecting specific compounds within materials or within the environment — security, infrastructure, health and the environment. The application of these techniques is broad, ranging from detecting the presence of certain chemical species to evaluating movement or stress changes that may occur with time. Imaging methods which are non-invasive, portable and flexible are desired. Resonance methods which detect subtle interactions between nuclei and their surroundings possess these highly desirable

attributes. Examples which can examine quadrupolar nuclei are NMR and NQR. [1, 2, 3] Quadrupolar nuclei are present in a wide range of materials including organometallics, zeolites, clays, cements, catalysts, ceramics, fire retardants, polymers and flame retardants. In order for these imaging methods to be used certain parameters are needed to describe the interaction observed; these parameters dictate the hardware for an instrument, the spectral area which the instrument tunes in and are vital to spectral interpretation. It is these parameters which we calculate.

Faster single processors and parallel computing techniques allow us to push calculation methods to give good predictions for application to materials analysis and imaging. With recent increases in computing power, good quality calculations for these parameters are now feasible. Using a single central processing unit for a calculation, we can accomplish as much as 8-12 times more work than we could just five years ago. Because of improvements in and application of parallel computing techniques to these faster single processors, we are able to accomplish even more work by running a single calculation with many single processors. More computer power also means that we can test and extend existing methods of calculation; we can now more completely describe electronic structure and better estimate many-body effects or how electron density depends on instantaneous electron positions. These computing improvements enable quality predictions for use in materials analysis.

The applications to materials analysis for the spectral parameters we predict are interesting. The bromine-containing molecules are flame retardants and models. Flame retardants can be found in common products such as computer monitor and television cabinet plastic. Because flame retardant dispersal within the plastic is unknown an economic application of these

predictions is to assist in determining and thus improving their dispersal.[4] An additional application of predictions for bromine-containing molecules is environmental; because certain bromine-containing molecules are suspected of contributing to environmental problems such as ozone depletion the predictions will assist by detecting and distinguishing between them.[5] The nitrogen-containing molecules are explosives and models and as a result parameter predictions for these have environmental and security applications; they can assist in detection and thus remediation of explosives from military sites and can assist in instrument development such as airport security scanners.[6] Some of the aluminum-containing systems are zeolites. The predictions for these also have environmental applications, such as helping to answer the question of how long a toxic waste may stay immobile in a storage cement. The remaining aluminum-containing systems are catalysts and models. The predictions for these have economic implications; predictions will help elucidate catalytic structure and thus mechanisms for polyolefin production. Polyolefins make up plastics in many household products and in 1998 2.8 billion pounds of olefins were produced.[7] While the work here is specific and detailed it is upon such details that big-picture contributions are built.

1.1 Historical Background

Figuring out electronic configuration and nuclear coordinates is one of the most fundamental and exciting aspects of chemistry. It shows where atoms are located within molecules, between which atoms bonds form, and the types of bonds that form. It can even be the fingerprint of an entire chemical compound or a distinct sign for a family of compounds. This information

serves as a building block to more abstract chemical information that is useful to gain insight into nature and improve man-made products.

An extremely interesting method of determining this information is to study the subtle interactions of one nucleus with its surroundings — other nuclei and electrons.[8, 9, 10, 2, 11, 1] One of these interactions is the nuclear quadrupole interaction (NQI). This is the basis for many spectroscopic techniques including NMR, NQR, Mössbauer spectroscopy, time-differential perturbed-angular-correlations (TDPAC), and some aspects of microwave spectroscopy. A few reviews serve to describe NQI studies on simple metallic solids via experiment[12, 13, 14]. A more recent review on solid-state NMR spectroscopy methods is also available[15]. Experimental studies of the NQI use atomic emission[16], atomic and molecular beams through electric fields[17, 18], microwaves[19, 20, 21], radio waves[11], magnets, nuclear radiation, the Doppler shift, and even explosives[22, 23, 24]. Predicting the NQI with existing theories serves to test and improve the theories and interpretation of the experiments.

The initial contributions to the knowledge of the NQI are largely of concept and discovery. In 1931 Pauli and Racah first suggest the idea of an asymmetric nuclear charge distribution [25, 26]. The interaction of this asymmetric charge distribution with its surroundings is the NQI which Schmidt and Schuler first detect in 1935 as a departure from the interval rule in the hyperfine structure of the atom Europium [27]. In 1936 Casimir publishes *On the Interaction Between Atomic Nuclei and Electrons*, giving the theory of the effect of a nuclear quadrupole moment on atomic energy levels [8]. In 1939 Kellog, Rabi, Ramsey, and Zacharias are the first to observe NQI in molecules with the molecule HD, showing the deuteron to be a prolate spheroid spinning about its major axis [28, 29]. Prolate is extended length-

wise and rotating an ellipse around its long axis creates a prolate spheroid. Then almost immediately Nordsieck and others perform analytic calculations on explicit wavefunctions, to obtain the nuclear quadrupole moment (Q) and the EFG. They combine Q and EFG to compare to the experimentally determined nuclear quadrupole coupling constant (NQCC).[30, 31, 32]

The concepts and validating discoveries of the earlier period lead to more NQI studies, especially in chemistry. In 1949 Townes and Dailey excellently describe how NQCCs provide important information for molecular structure theory [33]. Dehmelt and Kruger in 1951 discover pure NQR where energy transitions of the quadrupolar nucleus are directly observed (versus its manifestation as line broadening and uneven Zeeman level splitting in NMR). Both NMR and NQR obtain information about the NQI, but NMR uses a magnet, while NQR does not [34]. NQCCs for a wide variety of molecules become readily accessible experimental quantities.[35, 36] Cuprite (Cu_2O) becomes the first crystalline substance to which the NQR method is applied to yield a nuclear quadrupole resonance frequency [37].

The progress of present day EFG calculations, as our research employs, is possible because of computer programs applying self-consistent field molecular orbital theory (SCF-MO or MO) and density functional theory (DFT). These were recently recognized with the Nobel Prize in chemistry [38]. In 1951 Roothaan begins work on an iterative self-consistent procedure for calculating the expansion coefficients to create wavefunctions from basis sets (SCF-MO)[39, 40]. In 1969 when E. A. C. Lucken publishes *Nuclear Quadrupole Coupling Constants*, he discusses calculations of EFGs via SCF-MO for small molecules [1]. In the early 1970s John A. Pople and others develop the currently pervasive and popular commercial computer program Gaussian [41, 42]. It and similar programs implement SCF-MO theory with Gaussian

basis sets, dramatically improving speed for calculating chemically interesting molecular properties. The use of computers to solve problems too tedious and time-consuming to work out by hand is not only really cool, but is taken seriously by government funding agencies; in 1977 the National Science Foundation and the Department of Energy jointly fund National Resources for Computations in Chemistry and the popular and free-for-academic-use program GAMESS[43] (General Atomic and Molecular Electronic Structure System), which is created from HONDO and other extant quantum chemistry programs. In the mid 1960's Kohn and Sham develop DFT, but it is not until two decades later that it becomes popular in chemistry [44, 45, 46]. These developments only trace all the efforts that contribute to the electronic structure computer programs which we now use to calculate the gradient of the electric field at a quadrupolar nucleus and thus study its interactions with the asymmetric nuclear charge distribution.

There are many, many EFG calculations in the literature. Lucken mentions many EFG calculations in his book and he points out that NQCC calculations are a sensitive test of complicated self-consistent wavefunctions [1]. People study EFGs by calculations:

1. to measure distortion from perfect tetrahedral or octahedral symmetry, because the EFG vanishes if it is located in a perfectly centrosymmetric environment such as a tetrahedron or octahedron.[33, 47];

2. to investigate lattice or next nearest neighbor molecule effects;

3. to study the effects of hydrogen bonding [48, 49, 50, 51, 52, 53, 54, 55, 56];

4. to study the hydrogen bonded and isolated states of the H_3O^+ ion in p-toluenesulfonic acid monohydrate with ^{17}O[57];

5. to study the effects of hydrogen bonding for amide functional group [58, 59];

6. to compare experimentally determined nuclear quadrupole moments with those obtained from EFG calculations and NQCC measurements [60, 61, 62, 63, 64, 65, 66, 67, 68, 69];

7. to determine chemical bond ionicity or covalency [70, 71];

8. to compare the relative effect of functional groups in organic molecules [72, 73] and in straight-chain chloroalkenes [74];

9. to obtain the orientation of a small probe molecule relative to cavities, surfaces, or other molecules [75, 76];

10. in superconducting ceramic high-T_c materials [77, 78], semiconductors [79], iron-nickel alloys [80], Zn compounds such as spinels and chalcogens [81, 82, 83], and square-pyramidal complexes with Co, Rh, and Ir [84];

11. in extremely toxic Be compounds [85];

12. in mercurous and mercuric halides [86];

13. in clusters representing Sn(II) and Sn(IV) compounds [87];

14. in single-molecule and crystalline S compounds [88];

15. in N containing compounds such as purines, pyrimidines, amides, thioamides, azoles, and azines [89, 90, 91, 92] and even the explosive RDX[93];

16. and EFG polarizabilities in small molecules [94, 95, 96].

Clearly, the EFG literature is rich and growing rapidly. A few sources recommend themselves for introduction to the field and focus on chemi-

cal information. Townes and Dailey link EFG information and spectra – such as observed nuclear quadrupole effects – to chemically interesting electronic structure, chemical coordination, ionicity and symmetry of surrounding atoms [33]. Butler and Keiter provide a tutorial including pictures to help visualize important concepts; a discussion of octahedral, axial and low symmetry situations; and an example of interpreting static structure and bonding from the spectra of a deuterated site using NMR spectroscopic parameters [97]. Lucken's book lays down some mathematical framework for quadrupolar Hamiltonians, discusses many different experimental approaches for obtaining quadrupolar information and gives an overview of experimental results up to 1970 [1].

Some newer sources are important because they are investigating important questions about extremely accurate EFG calculation. They examine such items as relativity and picture change effects [98, 99, 100]. The systems they study are extremely small – single atoms or the occasional diatomic molecule. We do not use these methods because they are too computationally demanding for the larger systems in which we are interested. These methods refine nuclear quadrupole moment values by examining atoms and small systems such as F_2 [101], CuCl, AgCl and AuCl [102], AlF and AlCl [103] They do provide useful estimates of the error we incur by neglecting relativistic effects. For example atomic calculations suggest that relativity can effect the EFG of a single Al atom, through changes in p electron density, as much as $\frac{1}{10}$MHz [99]. Relativity is a greater concern for systems with much larger atoms such as silver and gold chlorides and the biggest effect on the EFG of AuCl is from changes in the valence electron density [102].

Other sources are important because they answer questions about basis set completeness, or how large of a basis set is necessary to accurately predict

EFGs. This information is directly applicable to one of the methods we use. EFGs are particularly demanding properties to calculate. Some predict that even with immensely large sextuple zeta basis sets, such as cc-pV6Z, EFGs would not converge within 3 thousands of an atomic unit of the basis set limit. At that same level of convergence – but with only large triple zeta basis sets, such as cc-pV3Z – molecular electric dipole moments and molecular electric quadrupole moments converge for five diatomics, BF CO HF NO^+ N_2. [104] This study recommends at least triple zeta basis sets with polarization and tight functions, observing faster convergence with Hartee-Fock (HF) than coupled cluster theory with single and double excitations (CCSD). [104]

We intend for this work to add to the literature and advance materials analysis. Taking advantage of innovations in computational chemistry and computer resources, we calculate EFGs and predict NMR/NQR spectral parameters of nuclei for which few calculations exist – $^{8}1Br$, ^{14}N and ^{27}Al – and for systems which are larger than many examined and are of keen interest for imaging and materials analysis.

CHAPTER 2
METHODOLOGY

2.1   The Hartree-Fock Method

The Hartree-Fock method combines

1. molecular orbitals (MO) for representing the wave function,

2. the Hartree-Fock Hamiltonian for determining the energy, and

3. the self-consistent field (SCF) method for solving the variational equation to obtain the coefficients of linear combination which build molecular orbitals from basis sets.

2.1.1   Molecular Orbitals

The wavefunction, denoted by the capital greek letter Phi Φ, for the entire molecule or system is made up of molecular orbitals, denoted by the lowercase greek letter psi ψ. The molecular orbitals are built from a linear combination of atomic orbitals.

$$\psi_i = \sum_{\mu=1}^{n} c_{\mu i} \phi_\mu \tag{2.1}$$

In equation 2.1 ψ_i is the i-th molecular orbital, $c_{\mu i}$ are the coefficients of linear combination, ϕ_μ is the μ-th atomic orbital, and n is the number of atomic orbitals. In this context the terms basis function or contraction may also refer to an atomic orbital. A basis function may be a very simple mathematical

10

function which by itself does not represent all the properties of a physical atomic orbital.

The basis functions which we use are Gaussian type orbitals. Slater type orbitals are similar to the physical atomic orbitals of the hydrogen atom and depend on spherical harmonic functions Y_{lm}. Many Gaussian type orbitals approximate the shape of a single slater type orbital, but are still far faster for integral evaluation by computer. Equation 2.2 shows a Gaussian type orbital.

$$g(\alpha, l, m, n; x, y, z) = N e^{-\alpha r^2} x^l y^m z^n \tag{2.2}$$

In equation 2.2 N is a normalization constant, α is the exponent, x, y, z are Cartesian coordinates, l, m, n are integral exponents at Cartesian coordinates, and $r = x^2 + y^2 + z^2$. Just as the angular momentum quantum numbers in atoms designate s,p,d,f et cetera character, the sum of the l, m, n exponents, $L = l + m + n$, designates the same character in basis functions.

2.1.2 Hartree-Fock Hamiltonian

The Hartree-Fock (HF) method takes advantage of the fact that a single electron may be thought of as experiencing the average potential of all others in a system. HF searches for a solution to the Schrödinger equation,

$$\mathcal{H}_{HF}|\Phi\rangle = \mathcal{E}|\Phi\rangle \tag{2.3}$$

where $\mathcal{H}_{HF}$ is the HF Hamiltonian, Φ is the wave function, and $\mathcal{E}$ is the energy. The HF Hamiltonian is merely the sum of single electron operators, $f(i)$ called Fock operators,

$$\mathcal{H}_{HF} = \sum_i^N f(i) \tag{2.4}$$

where i is a counter over electrons. The HF equations are

$$f(1)|\phi_a\rangle = \epsilon_a|\phi_a\rangle \tag{2.5}$$

The Fock operator is the sum of two operators: the core-Hamiltonian operator and the effective one-electron potential operator,

$$f(1) = h(1) + \nu^{HF}(1). \tag{2.6}$$

The core-Hamiltonian operator evaluates the attraction to the nuclei of a single electron in terms of the kinetic and potential energy,

$$h(1) = -\frac{1}{2}\nabla^2 - \sum_A \frac{Z_A}{r_{1A}} \tag{2.7}$$

where the index A is over nuclei. The effective one-electron potential operator is also the sum of two operators: the Coulomb ($\mathcal{J}$) and the exchange ($\mathcal{K}$) operators.

$$\nu^{HF}(1) = \sum_b \{\mathcal{J}_b(1) - \mathcal{K}_b(1)\} \tag{2.8}$$

In equation 2.8 the index b is over electrons. The Coulomb operator is fairly concrete; it has a classical analog and expresses the fact that two negative charges repel each other. The Coulomb operator in this case approximates the two-electron interaction – which ought to involve the instantaneous positions of electrons – with an average one-electron potential.

$$\mathcal{J}_b = \int dx_2 \frac{|\phi_b(2)|^2}{r_{12}} \tag{2.9}$$

A simple potential uniquely defined at a local point in space exists for the Coulomb operator; it is local.

The exchange operator is much more abstract; it has no classical analog and enforces indistinguishability. Because electrons are fermions the exchange operator is necessary. Electrons are fermions because they are indistinguishable from each other; you are not able to label them or tell them apart. If two switch positions the initial and final energy should be the same and the wavefunctions should also be identical. To account for

the indistinguishability of electrons the wave function in the HF method is a slater determinant of spin orbitals. Determinants are antisymmetric. Using an antisymmetric linear combination of product of spin-orbitals for the wavefunction is the Fock part of Hartree-Fock.

The exchange operator enforces this antisymmetry by simply switching electron positions ($\phi_b \leftrightarrow \phi_a$) in equation 2.10 to those in equation 2.11.

$$\mathcal{J}_b \phi_a(1) = \left[\int dx_2 \phi_b^*(2) \frac{1}{r_{12}} \phi_b(2) \right] \phi_a(1) \tag{2.10}$$

$$\mathcal{K}_b \phi_a(1) = \left[\int dx_2 \phi_b^*(2) \frac{1}{r_{12}} \phi_a(2) \right] \phi_b(1) \tag{2.11}$$

A simple potential does not exist for the exchange operator that is uniquely defined at a local point in space; it is nonlocal.

The HF method uses several items to solve the Schrödinger equation: an average one-electron potential for the Coulomb interaction between electrons, electron switching to satisfy the indistinguishability requirement for exchange, the core-Hamiltonian for the electron kinetic energy and electron-nuclei potential energy.

2.1.3 Variational Equation

The HF method searches for the orbitals ϕ_μ that minimize the energy. This search is made using the Rayleigh-Ritz method within variation theory. Because we do not know the exact energies and wavefunction we need a method which allows us to refine an initial guess toward a more precise solution. Variation theory is one of these methods. The variation principle states that, with a wavefunction which satisfies the boundary conditions of the problem and which is well-behaved, the expectation value of the Hamiltonian is an upper bound to the ground state energy. That is, we can be sure that the energy of an approximate wavefunction is always too high.

In variation theory one begins with a guess and then varies some part of that guess to find a minimum in a property. In the Rayleigh-Ritz method the coefficients in a linear combination of fixed basis functions are the part that is varied. These coefficients are the same as the $c_{\mu i}$ in equation 2.1, which are the coefficients of linear combination which build molecular orbitals from basis sets. The coefficients are changed until they give the smallest possible Rayleigh ratio. The Rayleigh ratio or variational integral, $\mathcal{W}$ is

$$\mathcal{W} = \frac{\langle \psi^* | \mathcal{H}_{HF} | \psi \rangle}{\langle \psi^* | \psi \rangle}. \tag{2.12}$$

The minimum energy corresponds to the minimum of this integral. Substituting equation 2.1 into equation 2.12 gives:

$$\mathcal{W} = \frac{\sum_{\mu\nu} c_\mu c_\nu \langle \phi_\mu | \mathcal{H}_{HF} | \phi_\nu \rangle}{\sum_{\mu\nu} c_\mu c_\nu \langle \phi_\mu | \phi_\nu \rangle} = \frac{\sum_{\mu\nu} c_\mu c_\nu H_{\mu\nu}}{\sum_{\mu\nu} c_\mu c_\nu S_{\mu\nu}} \tag{2.13}$$

where the operator $\mathcal{H}$ has been replaced with the shorthand notation for integrals with $H_{\mu\nu} \equiv \langle \phi_\mu | \mathcal{H}_{HF} | \phi_\nu \rangle$ and the overlap integral $S_{\mu\nu} \equiv \langle \phi_\mu | \phi_\nu \rangle$. In equation 2.13 μ and ν are indices over atomic orbitals.

For the minimization of the variational integral two conditions on the orbitals are:

- each is normalized $\langle \phi_\mu(1) | \phi_\nu(1) \rangle = 1, \mu = \nu$;

- each is orthogonal to the others $\langle \phi_\mu(1) | \phi_\nu(1) \rangle = 0, \mu \neq \nu$.

We find the minimum of this integral by differentiating with respect to each coefficient in turn and setting to zero the partial derivative of the variational integral, $\mathcal{W}$, with respect to each coefficient, c_ξ, $\partial \mathcal{W} / \partial c_\xi = 0$.

$$
\begin{aligned}
\frac{\partial \mathcal{W}}{\partial c_\xi} &= \frac{\sum_\nu c_\nu H_{\xi\nu} + \sum_\mu c_\mu H_{\mu\xi}}{\sum_{\mu\nu} c_\mu c_\nu S_{\mu\nu}} - \frac{\left(\sum_\nu c_\nu S_{\xi\nu} + \sum_\mu c_\mu S_{\mu\xi} \right) \sum_{\mu\nu} c_\mu c_\nu H_{\mu\nu}}{\left(\sum_{\mu\nu} c_\mu c_\nu S_{\mu\nu} \right)^2} \\
&= \frac{\sum_\nu c_\nu \left(H_{\xi\nu} - \mathcal{W} S_{\xi\nu} \right)}{\sum_{\mu\nu} c_\mu c_\nu S_{\mu\nu}} + \frac{\sum_\mu c_\mu \left(H_{\mu\xi} - \mathcal{W} S_{\mu\xi} \right)}{\sum_{\mu\nu} c_\mu c_\nu S_{\mu\nu}} \\
&= 0
\end{aligned}
\tag{2.14}
$$

In equation 2.14 the index ξ is over the coefficients of linear combination. When the numerator in equation 2.14 is zero this corresponds to the minimum for which we are looking. To find the case when the numerator is zero we must solve these equations:

$$\sum_\mu c_\mu \left(H_{\mu\xi} - \mathcal{W}S_{\mu\xi}\right) = 0 \tag{2.15}$$

These equations comprise a set of simultaneous equations for the coefficients c_μ and are called the secular equations. In order to find solutions to equations 2.15 the secular determinant,

$$det\, |H_{\mu\xi} - \mathcal{W}S_{\mu\xi}| = 0 \tag{2.16}$$

must be zero. Solving equation 2.16 gives a set of values of $\mathcal{W}$ as the roots of the corresponding polynomial. The lowest value in this set is the best value of the energy for the ground state of this system with the selected basis set. Using this lowest value, we find the coefficients in the linear combination by solving the set of secular equations with this value of $\mathcal{W}$.

Application of the variation theorem to the HF SCF method allows us to calculate an upper bound for the energy.

2.1.4 Hartree-Fock-Roothaan Equations

An integral part of the current HF SCF method is the expansion of MOs ψ_i as a linear combination of a set of one-electron basis function ϕ_i, shown in equation 2.1. Roothaan proposed this in 1951.

Substitution of this expansion (equation 2.1) into the HF equations (equation 2.5) and subsequent multiplication by the complex conjugate of the basis functions, ϕ^*, and integration gives the Hartree-Fock-Roothaan equations:

$$\Sigma_{s=1}^b c_{si}(F_{rs} - \epsilon_i S_{rs}) = 0, r = 1, 2, ..., b \tag{2.17}$$

It is the solutions to these equations that are sought during the SCF method. The SCF method is an iterative process because the F_{rs} integrals depend on the orbitals ψ_i, and the orbitals depend on the coefficients c_{is}, which are what is really being sought in the first place. This interdependency forces a set up step before the SCF actually commences.

2.1.5 HF-SCF

With the details of basis functions and MOs, the HF operator, and the variational equation out of the way we can now see a sketch of the steps taken in the HF SCF method. Please see figure 2.1.

This sequence produces an electronic density with which property calculations such as the electric field gradient at a nucleus are made.

2.2 Density Functional Theory

The energy in density functional theory is expressed as a function of the density,

$$E_{tot}(\rho_\uparrow, \rho_\downarrow) = T_s(\rho_\uparrow, \rho_\downarrow) + E_{ee}(\rho_\uparrow, \rho_\downarrow) + E_{Ne}(\rho_\uparrow, \rho_\downarrow) + E_{xc}(\rho_\uparrow, \rho_\downarrow) + E_{NN}, \quad (2.18)$$

where $(\rho_\uparrow, \rho_\downarrow)$ are the spin densities, E_{tot} is the total energy, T_s is the kinetic energy of the non-interacting particles, E_{ee} is the electron-electron repulsion energy, E_{Ne} is the nuclear-electron attraction energy, E_{xc} is the exchange correlation energy, and E_{NN} is the repulsive Coulomb energy of the fixed nuclei.

The total energy is minimized similar to the molecular orbital method. Minimization of the energy is done by using the variational principle and constructing the spin densities from orbitals χ_{ik}^σ.

$$\rho_\sigma(r) = \sum_{i,j} \rho_{ik}^\sigma |\chi_{ik}^\sigma(r)|^2 \quad (2.19)$$

1. input

   - atom positions
   - charge
   - spin multiplicity
   - choose basis functions

2. set up

   - compute one-electron integrals
   - guess initial MOs: guess occupied MO expressions as linear combination of basis functions
   - compute two-electron integrals
   - compute Fock operator F using initial MOs
   - compute matrix elements $F_{rs} = \langle\phi_r|F|\phi_s\rangle, S_{rs} = \langle\phi_r|\phi_s\rangle$
   - solve secular equation for improved coefficients
   - compute improved MOs from improved set of coefficients

3. SCF cycle

   - compute Fock operator F using improved MOs
   - compute matrix elements $F_{rs} = \langle\phi_r|F|\phi_s\rangle, S_{rs} = \langle\phi_r|\phi_s\rangle$
   - solve secular equation, improved coefficients $det(F_{rs} - \epsilon_i S_{rs}) = 0$
   - compute improved MOs from improved set of coefficients
   - check change in energies and/or densities
     - if change too big, go back to SCF cycle start
     - if change small enough, stop; this is a self-consistent field.

Figure 2.1: Steps for typical HF *ab initio* calculation.

In this equation ρ_{ik}^σ are occupation numbers that satisfy this condition $0 \leq \rho_{ik}^\sigma \leq 1/w_k$, where w_k is the weight of point k from symmetry requirements. From here variation of E_{tot} gives the Kohn-Sham equations:

$$[-\nabla^2 + V_{Ne} + V_{ee} + V_{xc}^\sigma]\chi_{ik}^\sigma(r) = \epsilon_{ik}^\sigma(r)\chi_{ik}^\sigma. \tag{2.20}$$

The solution of these equations is an iterative process and is done self-consistently. This iteration is required because the Kohn-Sham orbitals require the knowledge of the potentials, the potentials depend on the density, and the density comes from the orbitals.

2.2.1 Exchange Correlation Functionals

Traditional exchange correlation functionals divide into two categories:

local includes only the electron spin densities in the exchange and correlation functional. $X\alpha$ is an example.

$$\mu_{xc} \equiv \mu_{xc}(\rho_\uparrow, \rho_\downarrow) \tag{2.21}$$

where $(\rho_\uparrow, \rho_\downarrow)$ are the up and down spin densities respectively and μ_{xc} is the exchange correlation functional.

nonlocal or gradient-corrected, includes the electron spin densities and the gradients of the electron spin densities. The generalized gradient approximation (GGA) is an example.

$$\mu_{xc} \equiv \mu_{xc}(\rho_\uparrow, \rho_\downarrow, \nabla\rho_\uparrow, \nabla\rho_\downarrow) \tag{2.22}$$

where $(\nabla\rho_\uparrow, \nabla\rho_\downarrow)$ are the gradients of the up and down spin densities.

Hybrid density functionals combine traditional functionals and Hartree-Fock. They define the exchange functional as a linear combination of Hartree-Fock, local and gradient-corrected exchange terms. They define the correlation functional as local or gradient-corrected terms or a combination of local

and gradient corrected terms.[105, p119] An example is Becke's 3 Parameter Lee-Yang-Parr (B3LYP) method. Becke's 1988 gradient-corrected, exchange functional is combined with a parameterization of the gradient-corrected Lee-Yang-Parr (LYP) correlation functionals. [106, 107, 108, 109, 110, 111, 106, 112]

2.3 The Full Potential Linearized Augmented Plane Wave Method

We calculate EFGs using the WIEN[113] computer program. This program implements full-crystal density functional theory with the full potential linearized augmented plane wave method (FP-LAPW)[114]. Exchange and correlation are included with the GGA [115, 116]. GGA is preferred for EFGs[117, 118]. Linear variation of the LAPW provides the solution to the Kohn-Sham equations (equation 2.20). The FP-LAPW method divides the unit cell of a crystal into two parts:

1. spheres around the atoms and

2. an interstitial region.

Inside the atomic spheres is a linear combination of the product of radial functions and spherical harmonics, while a plane wave expansion is in the interstitial region.

For each atomic sphere the radial functions, $u_l(r, E_l)$, and spherical harmonics, $Y_{lm}(r)$, combine according to this equation,

$$\phi_{k_n} = \sum_{lm}[A_{lm}u_l(r, E_l) + B_{lm}\dot{u}_l(r, E_l)]Y_{lm}(\hat{r}). \qquad (2.23)$$

In this equation $u_l(r, E_l)$ is the regular solution of the radial Schrödinger equation at the origin for energy E_l of the appropriate l-like character band

and the spherical part of the potential within the atomic sphere, $\dot{u}_l(r, E_l)$ is the energy derivate at E_l of u_l. The radial function is linearized by the linear combination of u_l and $\dot{u}_l$. These atomic-like functions augment the interstitial region plane waves; the coefficients A_{lm} and B_{lm} are set to match the value and slope of this linearized radial function within an atomic sphere to a corresponding basis function in the interstitial region. The coefficients A_{lm} and B_{lm} are also functions of k_n defined next.

The basis set in the interstitial region is a plane wave expansion,

$$\phi_{k_n} = \frac{1}{\sqrt{w}} e^{i k_n r}. \tag{2.24}$$

The reciprocal lattice vectors are K_n and the wave vector inside the first Brillouin zone is k. These combine to define k_n, $k_n = k + K_n$.

The combination of atomic-like functions within the spheres and the plane waves in the interstitial region form the LAPW basis. This LAPW basis is the basis upon which the Kohn-Sham equations (equation 2.20) are expanded using the Rayleigh-Ritz variational principle to determine the coefficients c_n,

$$\psi_k = \sum_n c_n \phi_{k_n}. \tag{2.25}$$

Inside the atomic spheres, spherical harmonics up to $l = 6$ are used. This is a full potential method; no shape approximations are made for the potential or the electronic charge. The plane wave expansion is limited by computer main memory size; for each k-point plane wave coefficients must be calculated by diagonalizing a matrix with dimensions equal to the number of K vectors. Including the other molecules and symmetry from the crystal is a distinct advantage for accurate EFG tensor orientations as compared to the embedded-cluster MO approach.

2.4 The EFG and Spectral Parameters

2.4.1 Quadrupolar Interaction Energy and Hamiltonian.

The energy of the NQI is the nuclear quadrupole coupling energy, $E_Q = -\frac{1}{6}Q\cdot V$, the inner product of two symmetric second rank tensors: the nuclear quadrupole moment and the electric field gradient. Casimir, Lucken, and Slichter derive the quadrupolar Hamiltonian with varying degrees of detail and rigor[8, 119, 120, 102]. The quadrupolar Hamiltonian operator obtains the quadrupolar energy by acting on a wave function; it will express the electrostatic energy difference between electrons in the field of a nuclear point charge and electrons in the field of a nuclear quadrupole. One may begin with the classical expression for the interaction energy of a charge distribution with density ρ in an external potential V, $E = \int \rho(r)V(r)d\tau$. Here the charge distribution ρ is that of the nucleus of interest, the center of which is the origin and the external potential V is due to all charge (electrons and other nuclei) outside the nucleus of interest. Then expand the potential V in a Taylor series about the origin. Substitute this back into the energy equation and examine only the third term:

$$\frac{1}{2!}\sum_{\alpha,\beta} V_{\alpha,\beta} \int x_\alpha x_\beta \rho d\tau \qquad (2.26)$$

where we use this notation $V_{\alpha,\beta} \equiv \frac{\partial^2 V}{\partial x_\alpha \partial x_\beta}$ for the gradient of the potential with respect to length evaluated at $r = 0$ with the different Cartesian components are represented by subscripts $\{x_\alpha(\alpha : 1,2,3) : x,y,z\}$. This is the quadrupolar term where the electric field gradient from electrons and other nuclei interacts with the quadrupole moment of the nuclear charge distribution. Then simplify using 1) Laplace's equation, $\nabla^2 V = 0$, to show that the diagonal EFG tensor is traceless and 2) clever definitions to subtract out

the spherical terms which are independent of nuclear orientation. Obtain the quantum mechanical expression from the currently classical expression by replacing the classical variable for density with the quantum mechanical operator. Simplify the sum over all nuclear particles to only charged particles — protons. Finally, substituting the resulting expressions for the quantum mechanical nuclear quadrupole operator and the simplified electric field gradient we obtain the quadrupolar Hamiltonian $\mathcal{H}_Q = \frac{1}{6} \sum_{\alpha,\beta} V_{\alpha,\beta} \mathcal{Q}_{\alpha,\beta}^{(op)}$.

2.4.2 Charge Distribution Within The Nucleus: The Quadrupole Moment

A nucleus is a continuous charge distribution with a net charge equal to the number of protons in the nucleus. We use an expansion of multipoles to represent the continuous charge distribution as a sum, which requires the distance between a point and an arbitrary charge distribution to be large compared to the size of the distribution. Then the potential at these points can always be written as a sum of separate potential distributions due to monopoles, dipoles, quadrupoles, octupoles and on until the desired level of accuracy is achieved.[121] Examples of these distributions are shown in figure 2.2.

Many nuclei may be represented as a monopole or single point of charge, but some nuclei may not. They are not spherically symmetric — their neutrons and protons are mashed together in just such a way as to defy representation as a single charged point. In fact, some cannot even be represented by two points — a dipole. Instead, they must be modeled by a quadrupole — four charged points or two dipoles placed so that they have no net monopole or net dipole moments, do not coincide, and their electric effects at a distance do not quite cancel.

Monopole

Dipole

Quadrupole

Octupole
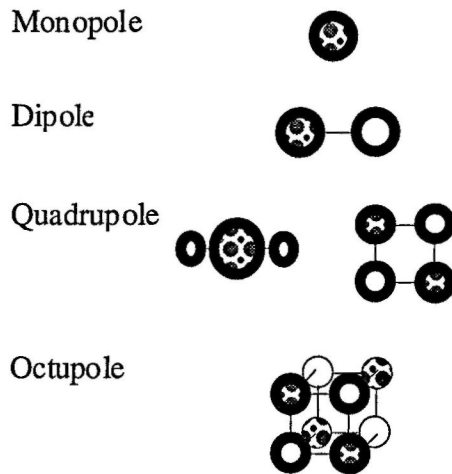
Figure 2.2: Multipole examples, different patterns represent opposite charges.

I I

$Q > 0$ $Q < 0$
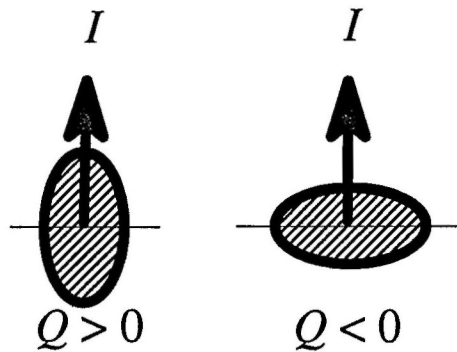
Figure 2.3: Orientation of nucleus with respect to spin for positive and negative Q. Q refers to the nuclear quadrupole moment and I to the spin axis.

Nuclei with spin $I \geq \frac{1}{2}$ have just such a shape that they require a quadrupole to represent the nuclear charge distribution; they posses a quadrupole moment. Their charge distribution is actually ellipsoidal, having cylindrical symmetry. As shown in figure 2.3, the nucleus may take on two orientations with respect to the spin axis: parallel or perpendicular[9]. The nuclei we study — ^{81}Br, ^{27}Al and ^{14}N — are parallel to the spin axis. The axis of cylindrical symmetry is perpendicular to the spin axis in ^{6}Li, ^{7}Li, ^{9}Li and ^{17}O. We reduce the nuclear quadrupole moment tensor to a single parameter because

the nucleus is in a state of definite angular momentum; charge distributions within nuclei are cylindrically symmetric along their spin axis. This parameter is the nuclear quadrupole moment and is given the symbol Q.

2.4.3 Charge Distribution Outside The Nucleus: The EFG Tensor

Outside the nucleus of interest the charge distribution contains two parts: electrons and protons from other nuclei. Other nuclei are treated as point charges because the distance between protons within a nucleus is much smaller than the distance between our point of interest and other electrons. We obtain the electron distribution from a self consistent field wave function. The charge distribution creates an electric field. It is the gradient of the electric field which interacts with the quadrupolar moment of the nucleus. The EFG tensor is the second derivative, with respect to distance, of the electrostatic potential.

2.4.4 NMR Spectral Parameters

The interaction between the nuclear-electric-quadrupole moment and the electric-field gradient from the surrounding charge can be completely described by five parameters. Because we usually compare the results of our calculations to NMR we will refer to them as the NMR spectral parameters. The EFG is diagonalizable into the principal axis system; all off-diagonal elements are zero.

$$\begin{bmatrix} \frac{\partial^2 V}{\partial x \partial x} & 0 & 0 \\ 0 & \frac{\partial^2 V}{\partial y \partial y} & 0 \\ 0 & 0 & \frac{\partial^2 V}{\partial z \partial z} \end{bmatrix}$$

It is traceless; the three diagonal components sum to zero.

$$\frac{\partial^2 V}{\partial x \partial x} + \frac{\partial^2 V}{\partial y \partial y} + \frac{\partial^2 V}{\partial z \partial z} = 0$$

By convention the three remaining components are ordered by absolute magnitude

$$|\frac{\partial^2 V}{\partial x \partial x}| \leq |\frac{\partial^2 V}{\partial y \partial y}| \leq |\frac{\partial^2 V}{\partial z \partial z}|$$

also denoted

$$|q_{xx}| \leq |q_{yy}| \leq |q_{zz}|.$$

The largest component, q_{zz}, is also denoted q. Because the EFG is traceless, it can be characterized by two independent components, C_q and η, whose definitions follow.

1. The nuclear quadrupole coupling constant,

$$C_q \equiv e^2 q Q/h \tag{2.27}$$

where e is the charge of an electron, q is the largest component of the EFG tensor in the principle axis system, Q is the nuclear-electric-quadrupole moment and h is Planck's constant.

Table 2.1: Note for Q we use the common unit millibarns, mb, the conversion to S.I. units is 1barn $\equiv 10^{-28} m^2$. We also give the conversion of q_{zz} to C_q from the output of [a] GAMESS and Gaussian which reports EFGs in atomic units (L^{-3}) with the older negative sign EFG convention, and [b] WIEN which reports EFGs in $V m^{-2} \times 10^{21}$.

nucleus	Q	ref.	conversion factor ($q_{zz} \rightarrow C_q$)	
			$\frac{MHz}{au}$ [a]	$\frac{MHz}{Vm^{-2}}$ [b]
^{27}Al	146.6(1.0)	[103]	-34.446	3.5448×10^{21}
^{14}N	20.44(3)	[122]	-4.8034	0.49431×10^{21}
^{81}Br	276(4)	[65]	-64.85	6.674×10^{21}

2. The asymmetry parameter describes the distortion of the EFG from axial symmetry and is labeled with the Greek letter eta η

$$\eta \equiv \frac{q_{xx} - q_{yy}}{q_{zz}} \tag{2.28}$$

$$\eta = \begin{cases} 0 & \text{symmetric} \\ 1 & \text{asymmetric} \end{cases}$$

$\eta = 0$ means cylindrical symmetry with the two smaller components equal in magnitude ($q_{xx} = q_{yy}$) and the largest component is twice as large, as in the case of a single terminal bond. Some examples for $\eta = 0$ are isolated terminal sites such as Al in AlCl or Br in 1-bromobenzene (as isolation decreases η can increase slightly, for example, $\eta \approx 0.15$ for Br in hexabromobenzene). Another example of $\eta = 0$ is a tetrahedral Al coordinated with three of the same type of atom and one of a different type, such as Al in $H_3AlN(CH_3)_3$. In other words, the gradient of the electric field is dominated by a single direction, as is the case for atoms at the end of isolated terminal bonds and atoms in a tetrahedral coordination with 3 of one kind of atom and 1 of another.

$\eta = 1$ means very asymmetric and that the two largest components are equal in magnitude but opposite in sign and the smallest component is zero. The molecule $[\{Me_2Al\}\{NMe_2\}]_2$ in the MAO models chapter is an example.

3. To determine the angles between the principal axis system and the lab axis system, α, β and γ, we take the inverse cosine of the largest component of each eigenvector.

$$\alpha = \cos^{-1}(\vec{q}_{xx,largest}) \tag{2.29}$$

$$\beta = \cos^{-1}(\vec{q}_{yy,largest}) \tag{2.30}$$

$$\gamma = \cos^{-1}(\vec{q}_{zz,largest}) \tag{2.31}$$

where $\vec{q}_{xx,largest}$ is the largest component of the eigenvector $\vec{q}_{xx}$ for the smallest eigenvalue q_{xx} of the diagonal EFG and the same notation for the eigenvectors for the other two diagonal EFG eigenvalues q_{yy}

and q_{zz}. If given the values of angles α, β and γ one can obtain the largest component of each eigenvalue by using the corresponding inverse operation. That is, because $x = \cos y$ then $y = \cos^{-1} x$.

$$\vec{q}_{x,largest} = \cos \alpha \tag{2.32}$$

$$\vec{q}_{y,largest} = \cos \beta \tag{2.33}$$

$$\vec{q}_{z,largest} = \cos \gamma \tag{2.34}$$

2.4.5 Conversion of NMR Spectral Parameters to NQR Frequencies

Direct transitions occur between quadrupolar energy levels when the EFG axes are fixed in space. These transitions correspond to the nucleus taking different orientations with respect to the EFG axes. For a majority of experiments with which we compare our results this transition takes place in the crystalline solid phase. For the solid phase the EFG axes can be considered fixed because in the solid phase vibrations are small.

2.4.6 Quadrupolar Hamiltonian

In order to relate the EFG to NQR frequencies, ν, we need to consider the interaction of nuclear spin, I, and the electronic wavefunctions for different angular momentum states, m. The Hamiltonian for pure quadrupolar resonance is [119, p36]

$$\mathcal{H}_Q = A \left\{ 3\mathbf{I}_z^2 - \mathbf{I}^2 - \frac{\eta}{2} \left(\mathbf{I}_+^2 + \mathbf{I}_-^2 \right) \right\} \tag{2.35}$$

where $A \equiv \frac{e^2 Q q_{zz}}{4I(2I-1)}$. The matrix elements between angular momentum states for $\Delta m = 0$ are

$$< m|\mathbf{I}_z|m' >= m\delta_{m,m'} \tag{2.36}$$

and for $\Delta m = \pm 1$ are

$$< m|\mathbf{I}_x \pm i\mathbf{I}_y|m' >= [(I \pm m)(I \mp m + 1)]^{\frac{1}{2}} \delta_{m \mp 1, m''} \tag{2.37}$$

For $\eta \neq 0$, when the EFG is not axially symmetric the off-diagonal matrix elements between the angular momentum eigenfunctions for $\Delta m = 2$ are needed. They are

$$< m'|\mathcal{H}_Q|m >= \frac{A\eta}{z}[(I \mp m - 1)(I \mp m)(I \pm m + 1)(I \pm m + 2)]^{\frac{1}{2}} \delta_{m',m \pm 2}. \quad (2.38)$$

This means that for EFGs without axial symmetry, even states separated by $\Delta m = 2$ mix. This requires diagonalization to obtain the interaction energy.

Nuclei with Half-integral Spin

The expression relating the EFG and the NQR frequency for nuclei with half-integral spin, I — such as ^{81}Br $(I = \frac{3}{2})$ and ^{27}Al $(I = \frac{5}{2})$ — is the secular equation for diagonalization of the angular momentum matrix.[119, p38]

For spin $I = \frac{3}{2}$ the angular momentum states m may be $|\frac{3}{2}|$ and $|\frac{1}{2}|$

$$E_m = E_{|\frac{3}{2}|} = 3A\left(1 + \frac{\eta^2}{2}\right)^2 \quad (2.39)$$

$$E_m = E_{|\frac{1}{2}|} = -3A\left(1 + \frac{\eta^2}{3}\right)^2 \quad (2.40)$$

The secular equation for $I = \frac{3}{2}$ is

$$E^2 - 3\eta^2 - 9 = 0. \quad (2.41)$$

Only one transition is observed for $I = \frac{3}{2}$ because asymmetry does not remove the $\pm m$ degeneracy. Finally, for nuclei with $I = \frac{3}{2}$, the relationship between the EFG and the NQR frequency is

$$\nu = \frac{e^2 Q q_{zz}}{2h}\left(1 + \frac{\eta^2}{3}\right)^{\frac{1}{2}}. \quad (2.42)$$

For other spin values, including $I = \frac{5}{2}$ for ^{27}Al, the situation is more complex and so is the secular equation. The secular equation for $I = \frac{5}{2}$ is

$$E^3 - (3\eta^2 + 21)E^2 - 20(1 - \eta^2) = 0 \quad (2.43)$$

Because of the additional complexity the secular equation must be solved numerically for different values of η. For the $I = \frac{5}{2}$ case one obtains three energy states. For example, an approximate solution for $\eta \leq 0.1$ is

$$E_{|\frac{5}{2}|} = A\left(10 + \frac{\eta^2}{9}\right) \tag{2.44}$$

$$E_{|\frac{3}{2}|} = A\left(-2 + 3\eta^2\right) \tag{2.45}$$

$$E_{|\frac{1}{2}|} = A\left(-8 - \frac{32\eta^2}{9}\right). \tag{2.46}$$

For $I = \frac{5}{2}$ two transitions are observed. Finally, for nuclei with $I = \frac{5}{2}$, the relationship between the EFG and the NQR frequency for $\eta \leq 0.1$ is

$$\nu\left(\frac{5}{2} \to \frac{3}{2}\right) = \frac{3e^2Qq}{10h}\left(1 - \frac{11}{54}\eta^2\right) \tag{2.47}$$

$$\nu\left(\frac{3}{2} \to \frac{1}{2}\right) = \frac{3e^2Qq}{20h}\left(1 + \frac{5}{54}\eta^2\right) \tag{2.48}$$

Nuclei with Integral Spin

The expression relating the EFG and the NQR frequency for nuclei with integral spin I — such as ^{14}N ($I = 1$) — is the secular equation for diagonalization of the angular momentum $m = \pm 1$ sub-matrix.[119, p39]

$$(A - E_\pm)^2 = A^2\eta^2 \tag{2.49}$$

$$E_\pm = A(1 \pm \eta). \tag{2.50}$$

$$\nu_\pm = \frac{3e^2Qq_{zz}}{4h}\left(1 \pm \frac{\eta}{3}\right) \tag{2.51}$$

The ground state, E_0, is $-2A$ and the resonance line is split into a doublet with frequencies ν_+ and ν_-. The low frequency angular momentum transition of $\Delta m = 0$ is also possible between the two energy levels E_+ and E_-:

$$\nu_d = \nu_+ - \nu_-. \tag{2.52}$$

CHAPTER 3

THEORETICAL APPROACH

3.1 Theoretical Approach

We use three major approaches:

1. single-molecule MO,

2. full-crystal FP-LAPW DFT (full linearized augmented plane wave density functional theory),

3. embedded-cluster MO.

For the first method, single-molecule MO, we use *ab initio* MO as implemented in the computer programs GAMESS [43] or Gaussian [41] to calculate the wavefunction, obtain the EFG tensor expectation value, and convert this into C_q, η and other desired data. These programs use gaussian type orbitals as a basis for expansion of the electron density in the region immediately surrounding an atom. The single molecule nuclear coordinates may come from experiment or may be built with a molecular builder program such as Spartan [123]. The coordinates are then optimized [124, 125] by varying the symmetry adjusted degrees of freedom for nuclear coordinates to reach the minimum energy. This is the actual potential minimum in the absence of vibrational motion. Alone this method does not include the explicit effects

of charge outside this single molecule. In solids these effects are due to other molecules in the crystal. It does include the electron cloud and its polarization: a far superior wavefunction to the often used simple point charge models. These point charge models often do not even include all atoms within a molecule, and they ineffectively represent the electron cloud polarization as a single Sternheimer parameter. To date we have not accounted for vibrational, relativistic or spin-orbit effects, believing these to be small. The single-molecule MO method is fast for small molecules and becomes increasingly time-consuming for larger molecules and more electrons. In addition, the single-molecule MO method may be applied to molecules of materials for which the crystal structure is unknown or that do not have a regularly repeating pattern.

For the second method, full-crystal FP-LAPW DFT, we use the WIEN [113] computer program. This program implements Kohn-Sham DFT [45, 46] by the full linearized augmented plane wave method [114]. This includes the infinite crystal lattice as a basis of plane waves augmented by radial functions and spherical harmonics within spheres to represent atomic contributions to the electron density. No shape approximations are made for the potential or the electronic charge density. Nuclear coordinates are taken from X-ray determination and cannot be easily optimized for minimum energy or forces with current computational resources and minimization algorithms. This method may partially include relativistic effects. Exchange and correlation are included to the extent of the functional used, which may be either the local spin density approximation (LSDA) [126, 127, 128] or generalized gradient approximation (GGA) [115, 116]. GGA is preferred for EFGs. Including the other molecules and symmetry from the crystal is an advantage over MO, providing EFG tensor orientations closer to those in a solid. The full-crystal

FP-LAPW DFT method is in general slower than the single-molecule MO, though DFT scales better for larger systems. The full-crystal FP-LAPW DFT method may be applied only to systems for which the crystal structure is known or may easily be deduced and have a regular repeating pattern. Though some efforts have been made to use it for single molecules by increasing the distance between molecules in the unit cell [129], this method is primarily used for crystals.

The third method we employ is the embedded-cluster MO MO method. In this method there are two regions:

1. the inner region consists of the nucleus of interest and immediate neighbors for which all-electron basis sets are used,

2. the outer region is an arbitrary number of atoms represented as point charges.

This method is useful for representing crystals and nonrepeating patterns of structure, not possible with WIEN. More details are in the andalusite section. Both the MO and full-crystal FP-LAPW DFT treat the nucleus as a single point charge, while solving for the electronic structure. This model is widely used by chemists and such an approximation may be adequate for answering questions about the quadrupolar interaction as well. When visualizing the interaction it should be kept in mind that this mathematical approximation is a computationally expedient simplification. The nucleus is not a single point charge, but is a collection of neutrons and protons.

3.2 Projects

To date our research consists of seven projects calculating the nuclear quadrupole coupling constants C_q, the asymmetry parameter η and EFG tensor

orientations for ^{14}N, ^{27}Al and ^{81}Br. We briefly examine two systems to validate our use of the methods:

1. diatomic aluminum halides (AlF and AlCl) with single-molecule MO and

2. corundum (α–Al_2O_3) with full-crystal FP-LAPW DFT.

Then, we seriously study five additional systems that have recent NQR data:

1. ^{27}Al nuclei in andalusite, a zeolite model – for characterizing the rare five-coordinate Al site, assigning NMR signals to crystallographic sites, and testing the full crystal DFT and the embedded-cluster MO methods for predicting EFGs;

2. ^{27}Al nuclei in andalusite, sillimanite and kyanite, three polymorphs of Al_2SiO_5 – for assigning NMR signals to crystallographic sites, and studying the effect of structural changes on ^{27}Al NMR spectral parameters due to temperature (25-1000^oC);

3. ^{81}Br nuclei in brominated aromatic flame retardants and models to assist in spectra interpretation for judging dispersal in high impact polystyrene;

4. ^{14}N nuclei in tetryl and tetryl mimics to predict the transition frequencies and thereby assist in detection of explosives;

5. ^{27}Al nuclei in cyclic $(N-Al)_x$ molecules for their similarity to the industrially important catalyst methyl-aluminum-oxane.

More detail will be discussed in the following chapters.

CHAPTER 4

ALUMINUM HALIDES, AlCl, AlF

4.1 Introduction

We explore the single-molecule MO approach for determining EFGs with two diatomic aluminum halide molecules: AlF and AlCl. Both the ^{27}Al NQCCs and Al-X bond distances are available from single experiments for each molecule [1, 130, 131]. More recent experimental values for ^{27}Al NQCCs are also available [132, 103], but they do not report the Al-X distance. A recent theory paper is in agreement with the AlF bond length [133] and recent work on improving the value of the ^{27}Al quadrupole moment examines both molecules in-depth, considering both relativistic and correlation contributions [103]. These molecules are perfect for exploratory calculations; calculations are fast because they are small with only 22 and 30 electrons.

4.2 Method

We examine four atomic basis sets for building molecular orbitals: 1) STO-3G 2) Pople 6-31G 3) Pople 6-311G 4) Dunning cc-pVXZ (X=2,3,4) [43, 41, 134]. For each basis set we calculate the wavefunction using the Restricted Hartree-Fock Self Consistent Field Method (RHF-SCF or RHF) and again with Møller-Plesset Second Level Perturbation Theory (MP2) as an approximate measure of the effect correlation has on the EFG at the aluminum nucleus.

34

4.3 Results and Discussion

We present the C_q of AlF and AlCl calculated at fixed and optimized center-to-center Al-X distances in figures 4.1 and 4.2. Results from four basis sets and two methods are in table 4.1.

We discuss the results of the diatomic aluminum halide calculations in terms of geometry and the quadrupole coupling constant as a function of that geometry. Because there are no angles and both are linear molecules, the Al-X distance is the only parameter to optimize for minimum energy. We calculate EFGs at both the experimentally determined and the optimized distance. The ratio of quadrupole coupling constant from AlCl to that of AlF presents an opportunity to examine the results independent of the quadrupole moment. We briefly examine the convergence of C_q with basis set.

4.3.1 Geometry

Two items present a context for the discussion of bond lengths: 1) bond lengths from calculations refer to the actual potential minimum in the absence of vibrational motion, while those from experiments are an average over zero-point vibrational motions. These may differ by 0.01Å according to Pople et al. [135]. 2) mean absolute deviations from experiment using the MO method range from 0.060 with RHF/STO-3G to 0.010 for MP2/6-31G(d) and 0.005 Å with MP4/6-311G(d,p). [135] Comparison of experimentally and theoretically determined bond distances for Al-F and Al-Cl shows errors less than 10% and closer to 1% in the best cases 6-31G(1d), 6-31G(3df), 6-311G(3df), cc-pV3Z and cc-pV4Z. With the addition of polarization functions to basis sets, the C_q from optimized distance calculations agree better with those performed at the experimental distance.

Table 4.1: AlCl and AlF calculated ^{27}Al nuclear quadrupole coupling constants C_q in megahertz with center-to-center distances d in Angstroms a) fixed at the value from experiment and b) optimized. Optimized distances are also shown. Experiment for Al-F: $C_q = -37.60$, $d = 1.65437$ and for Al-Cl $C_q = -29.20$, $d = 2.21298$.

basis set	a) C_q RHF	a) C_q MP2	b) C_q RHF	b) C_q MP2	d RHF	d MP2
			Al-F			
STO-3G	-46.23	-39.31	-47.02	-39.94	1.615	1.618
6-31G	-31.20	-28.78	-28.70	-25.70	1.709	1.730
6-31G(1d)	-33.46	-31.48	-33.76	-30.75	1.649	1.670
6-31G(2d)	-32.82	-30.48	-33.58	-30.08	1.641	1.663
6-31G(3d)	-32.41	-30.09	-32.97	-29.41	1.644	1.669
6-31G(3d1f)	-33.50	-31.23	-34.20	-30.58	1.642	1.667
6-311G	-40.49	-37.39	-37.18	-33.23	1.711	1.735
6-311G(1d)	-41.13	-38.70	-40.41	-30.92	1.666	1.763
6-311G(2d)	-41.14	-38.44	-41.84	-37.69	1.645	1.667
6-311G(3d)	-40.87	-38.02	-41.36	-36.84	1.648	1.674
6-311G(3d1f)	-41.11	-38.26	-41.76	-37.25	1.646	1.671
cc-pV2Z	-31.88	-29.82	-30.15	-27.55	1.690	1.708
cc-pV3Z	-41.03	-38.21	-41.15	-36.69	1.653	1.678
cc-pV4Z	-42.42	-39.54	-43.23	-38.45	1.643	1.671
			Al-Cl			
STO-3G	-30.16	-28.20	-29.39	-27.59	2.163	2.163
6-31G	-24.87	-22.89	-20.39	-18.79	2.293	2.306
6-31G(1d)	-27.06	-25.15	-26.03	-24.91	2.160	2.138
6-31G(2d)	-26.30	-23.93	-25.24	-22.87	2.160	2.163
6-31G(3d)	-26.37	-23.98	-25.31	-22.95	2.158	2.160
6-31G(3d1f)	-27.26	-24.94	-26.51	-24.37	2.149	2.146
6-311G	-32.54	-30.19	-26.49	-24.11	2.275	2.296
6-311G(1d)	-34.40	-32.21	-33.21	-31.94	2.157	2.136
6-311G(2d)	-33.81	-31.09	-32.68	-29.91	2.156	2.158
6-311G(3d)	-33.91	-31.05	-32.91	-29.93	2.153	2.157
6-311G(3d1f)	-34.30	-31.49	-33.53	-30.81	2.148	2.146
cc-pV2Z	-26.90	-24.70	-24.89	-23.27	2.189	2.178
cc-pV3Z	-33.36	-30.57	-32.27	-29.77	2.154	2.149
cc-pV4Z	-34.86	-32.01	-33.96	-31.43	2.149	2.143
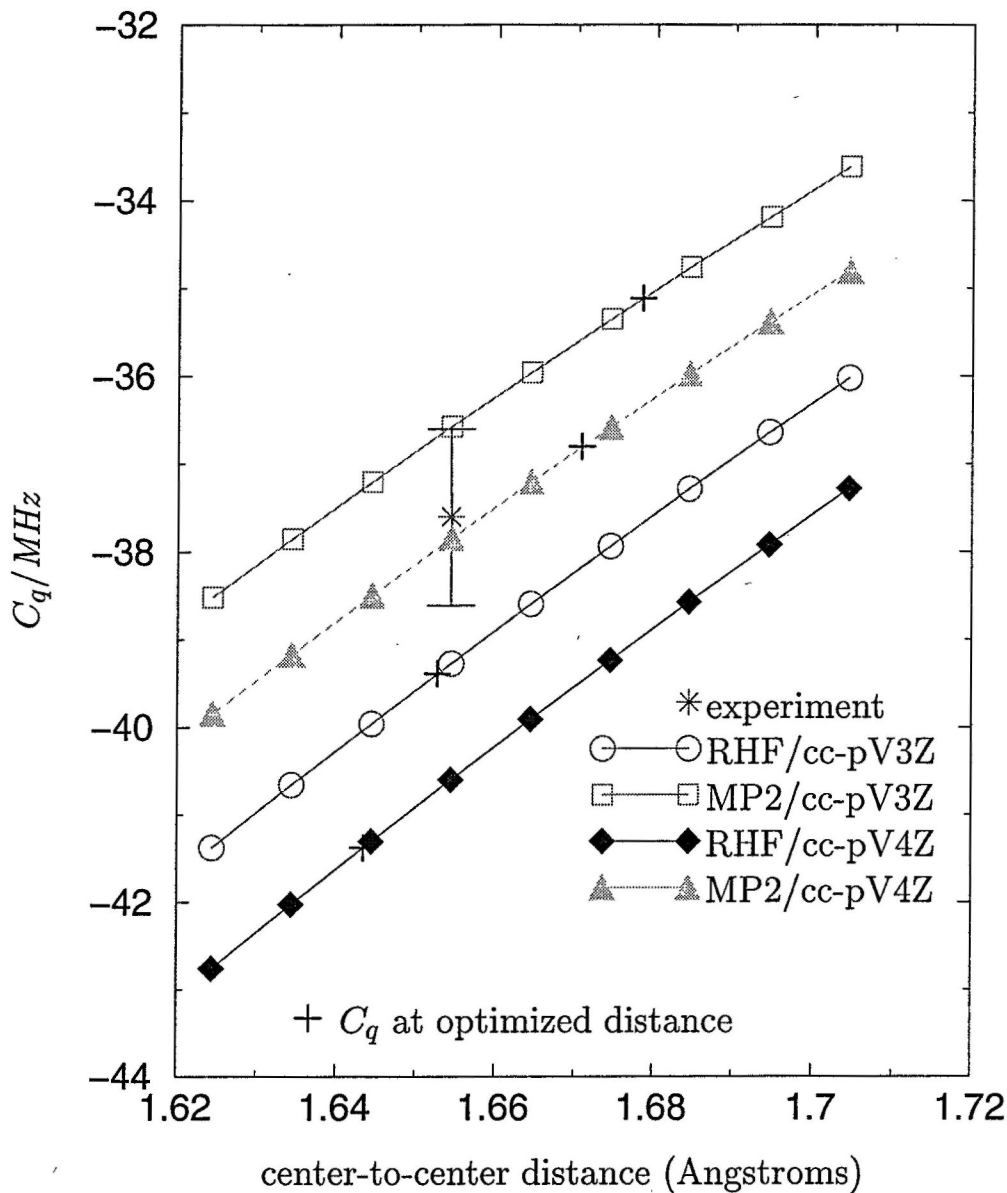
Figure 4.1: AlF ^{27}Al nuclear quadrupole coupling constants C_q in megahertz from RHF and MP2 single point calculations with the cc-pV3Z and cc-pV4Z basis sets at a series of fixed distances in angstroms. Values are shown from optimization calculations with each basis set for comparison. The experimental center-to-center distance is 1.65437 ± 0.00001 Å and the experimental value for $C_q = -37.60 \pm 1.0$ *MHz*. [131]

4.3.2 C_q as a Function of Geometry

Let us compare the C_q from our optimized distance calculations to the experimental value reported from microwave spectroscopy. (cf. figures 4.1 and 4.2)
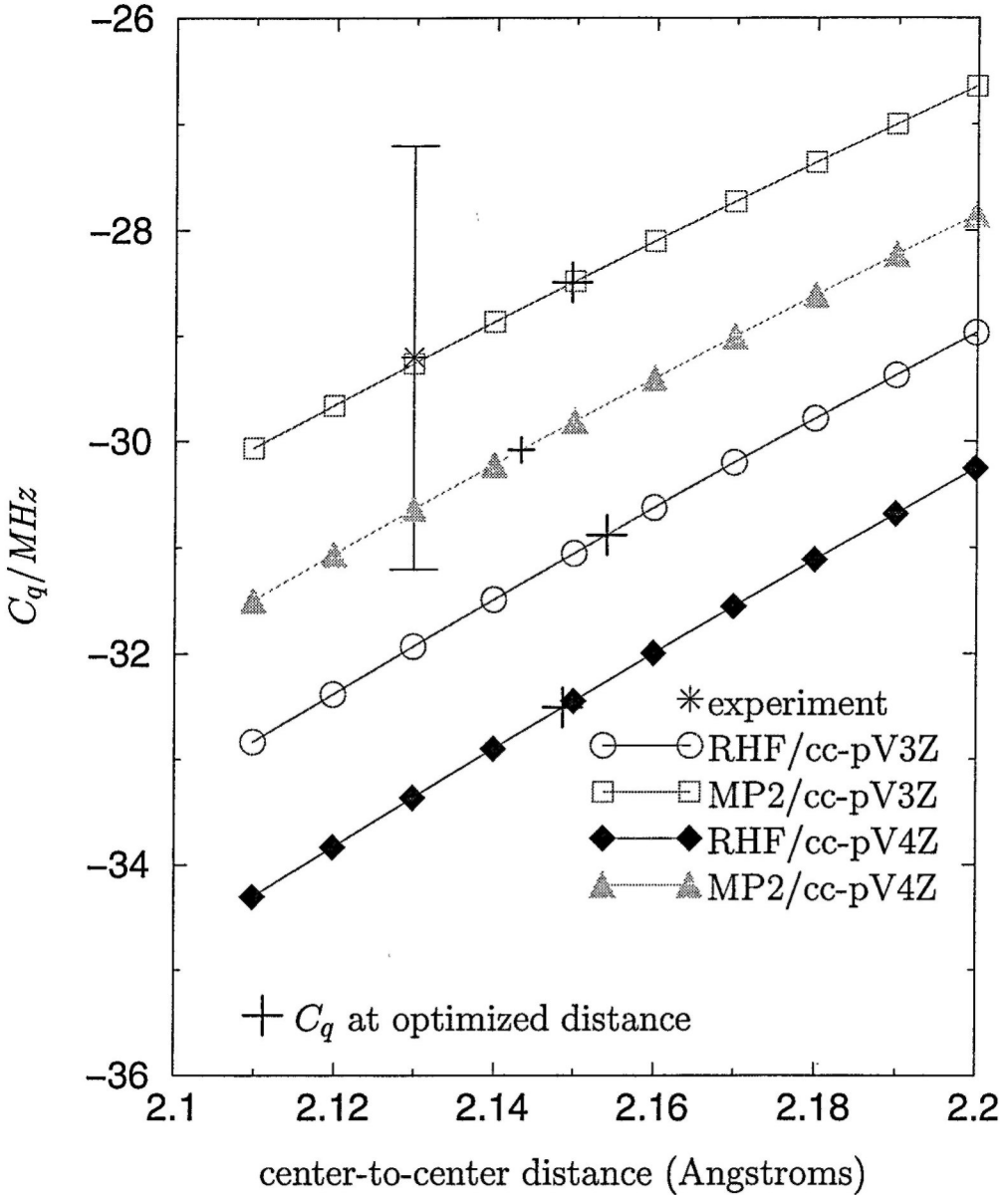
Figure 4.2: AlCl ^{27}Al nuclear quadrupole coupling constants C_q in megahertz from RHF and MP2 single point calculations with the cc-pV3Z and cc-pV4Z basis sets at a series of fixed distances in angstroms. Values are shown from optimization calculations with each basis set for comparison. The experimental center-to-center distance is 2.12983 ± 0.00001Å and the experimental value for $C_q = -29.20 \pm 2.0 MHz$. [131]

We have the advantage of knowing both the center-to-center distance and C_q, allowing us to see how accurate our prediction of C_q may be when neither

is known. Interestingly, a wavefunction which produces the correct nuclear coordinates does not always produce a C_q in agreement with experiment. For example, AlCl C_q from MP2/6-311G(3df) is only 0.99% off from experiment compared to 4.94% from MP2/cc-pV4Z, however center-to-center distance error is 0.75% and 0.52% respectively! A similar case may be found for AlF where C_q from MP2/STO-3G is 1.64% compared to -2.13% for MP2/cc-pV4Z and yet the error in center-to-center distance is -2.19% and .99% respectively. The effect of correlation on the EFG, measured $\frac{c_q^{MP2}-c_q^{RHF}}{c_q^{RHF}}$, is relatively constant at 6-10%, and is slightly higher for AlCl which has 8 more electrons than AlF. Using MP2 and the Pople 6-31G basis set the value of C_q is further from experiment than the RHF value. The opposite is true for the 6-311G and all of the cc-pVXZ basis sets; the MP2 value of C_q is closer to experiment than the RHF value. Perhaps the larger and more flexible basis sets yield a steeper gradient in the electron density and electron-electron correlation makes the gradient more shallow. For both molecules best agreement with experiment generally comes from the combination of MP2 and the larger basis sets: 6-311G(3df), cc-pV3Z and cc-pV4Z. We can conclude that a large basis set is essential and a method which includes correlation ought to be used for results to match experiment. Faster RHF calculations may be used to measure basis set convergence before including correlation. (cf. figures 4.1 and 4.2)

4.3.3 C_q Ratio, Q Independent

All the previous C_q value comparisons rely on the quadrupole coupling constant, Q. The ratio $C_q(\text{AlF})/C_q(\text{AlCl})$ is independent of Q. (cf. table 4.2) The combination of geometry optimization, RHF and the cc-pV3Z and cc-

pV4Z basis set best matches the C_q ratio of experiment. Several general items are worth noting:

1. optimized geometry calculations C_q ratios are closer to experiment than fixed experimental distance calculations;

2. for optimized geometry calculations, generally larger basis sets match experiment closest: 6-31G(3d), 6-31G(3d1f), cc-pV3Z and cc-pV4Z, with the exception of 6-311G;

3. for optimized geometry calculations, with the 6-31G(3d), 6-31G(3d1f), cc-pV3Z and cc-pV4Z basis sets, RHF fares better than MP2 at matching C_q ratios;

4. and RHF and MP2 C_q ratios from cc-pV3Z and cc-pV4Z are very close to each other.

Table 4.2: C_q ratios of calculated ^{27}Al nuclear quadrupole coupling constants, $C_q(\text{AlF})/C_q(\text{AlCl})$, a) fixed at the center-to-center distance from experiment and b) optimized. The ratio of experiment values is 1.29.

Basis Set	a) RHF	a) MP2	b) RHF	b) MP2
STO-3G	1.53	1.39	1.60	1.45
6-31G	1.25	1.26	1.41	1.37
6-31G(1d)	1.24	1:25	1.30	1.23
6-31G(2d)	1.25	1.27	1.33	1.32
6-31G(3d)	1.23	1.25	1.30	1.28
6-31G(3d1f)	1.23	1.25	1.29	1.26
6-311G	1.24	1.24	1.40	1.38
6-311G(1d)	1.20	1.20	1.22	0.97
6-311G(2d)	1.22	1.24	1.28	1.26
6-311G(3d)	1.21	1.22	1.26	1.23
6-311G(3d1f)	1.20	1.21	1.25	1.21
cc-pV2Z	1.19	1.21	1.21	1.18
cc-pV3Z	1.23	1.25	1.28	1.23
cc-pV4Z	1.22	1.24	1.27	1.22

4.3.4 Convergence

In principle, an infinitely large basis set and a method which includes all correlation (such as full configuration interaction) should give us an exact answer within the single-molecule MO method. In-practice this is not possible computationally, however we may measure our approach to this exact solution by considering how much change in a property like the EFG is seen with successively larger basis sets or methods which include more and more correlation. We consider basis set convergence with the cc-pVXZ basis sets, where X =2,3,4. The percent change in EFG from cc-pV2Z to cc-pV3Z is more than twenty, while from cc-pV3Z to cc-pV4Z is less than ten. Also, the C_q ratios from the cc-pV3Z and cc-pV4Z are very close to each other for both RHF and MP2. We can guess that we are approaching convergence, but are prevented from being sure because GAMESS does not support the higher angular momentum functions within the cc-pV5Z basis set.

4.4 Conclusion

Exploring the single-molecule MO approach for determining EFGs with these two diatomic aluminum halide molecules reveals that the EFG is sensitive to geometry, basis sets and correlation. The calculations which use optimized geometries and a large polarized basis set give the most reliable prediction of EFGs. The cc-pVXZ family of basis sets gives the most consistent results. RHF can be better than MP2 when comparing the ratio of C_q values among sites. Overall the calculations verify the ability of the single-MO approach to reliably predict EFGs for simple [27]Al compounds. They encourage the exploration of more complicated systems.

CHAPTER 5

CORUNDUM, α-Al$_2$O$_3$

5.1 Introduction

Corundum, $\alpha-$Al$_2$O$_3$, is well-known by crystallographers, experimentalists and theorists. Corundum is so thoroughly studied that X-ray crystallographers use it for instrument calibration[136, 137, 138]. This high degree of certainty regarding the crystal structure presents an excellent candidate for study with the full-crystal FP-LAPW DFT approach for determining EFGs. This is because the FP-LAPW DFT approach requires the coordinates of atoms to be specified as a periodic crystal structure. Corundum is also of interest to experimentalists who study it via NMR and NQR[139, 140, 141, 142, 143], variable temperature NMR[144] and such exotic NMR techniques as SQUID[141]. It is also the subject of the first complete measurement of the ^{27}Al chemical shift anisotropy[145]. Modern EFG calculations utilize a basis set and a self-consistent field method, examining the full crystal or a small atomic cluster[146, 147, 89, 148, 149, 144]. Early EFG calculations use only point charges and often employ a Sternheimer shielding constant to account for polarizability[150]. Other calculations on corundum examine questions regarding covalency and ionicity[151, 69, 152, 71]. Just as the diatomic aluminum halides serve as an excellent test of the MO approach, corundum is

an excellent test for the FP-LAPW DFT method because the structure is well-known and the EFGs have been well-studied from both experimental and theoretical perspectives.

While the cell is Al_4O_6[153], there is only one Al by symmetry in the structure. The single Al has nearly axial symmetry, and is octahedrally coordinated with the O atoms in a severely distorted octahedron; three O atoms are at a nearest-neighbor distance of 1.85505 Å and 3 more are at 1.97208 Å.

5.2 Method

We use WIEN97.1 for EFG calculations of corundum[113]. Each calculation uses for input the same: atomic coordinates(cf. table 5.1), unit cell parameters, and atomic sphere radii (R_{mt}). In atomic units (Bohr) the length of the unit cell axes are a=8.9983130, b=8.9983130, c=24.5432072. In degrees the angles between unit cell axes are $\alpha = 90$, $\beta = 90$ and $\gamma = 120$. The atomic sphere radii in atomic units (Bohr) are 1.83 for Al and 1.6 for O. The other parameters for the calculations are: k-points for integration of the Brillouin zone, G_{max} for the magnitude of the largest vector in the charge density Fourier expansion in a_o^{-1}, $R_{mt} \times K_{max}$ for the radius of the smallest sphere multiplied by the energy cut-off for the LAPW basis set expansion in $Bohr * Ry^{\frac{1}{2}}$. These divide into three groups:

group	$R_{mt} \times K_{max}$	G_{max}	k-points
1	8	15	1–1000
2	4–10	20	100
3	4–10	20	400

All other options are default for WIEN97.1. For more details see the methodology section.

Table 5.1: Corundum coordinates The fractional coordinates for corundum used in calculations.

x/a	y/b	z/c
Al, multiplicity 4		
.35220000	.35220000	.35220000
.64780000	.64780000	.64780000
.85220000	.85220000	.85220000
.14780000	.14780000	.14780000
O, multiplicity 6		
.55630000	.94370000	.25000000
.25000000	.55630000	.94370000
.94370000	.25000000	.55630000
.44370000	.05630000	.75000000
.75000000	.44370000	.05630000
.05630000	.75000000	.44370000

5.3   Results and Discussion

EFG data from experiment is available for both the ^{17}O and ^{27}Al sites in corundum, however our focus is only the Al site. In terms of absolute C_q, our results ($2.12 MHz$) compare favorably to other calculations. (cf. table 5.4) The other calculations with which we compare also include the full-crystal: Palmer et al. use the CRYSTAL computer program which employs Gaussian type orbitals[89, 152], Nagel et al. use the X-α method and variants[147]. Our results also compare fairly well to experiment ($\approx 2.39 MHz$). The FP-LAPW DFT method yields C_q near the values from experiment and similar to other methods of calculation.

We examine how the parameters for the FP-LAPW DFT method effect the EFG. First is the convergence of the EFG with basis set size using the parameter $R_{mt} \times K_{max}$, which is the radius of the smallest sphere multiplied by the energy cut-off for the plane wave expansion. As $R_{mt} \times K_{max}$ approaches 8, C_q converges to less than $\frac{1}{10} MHz$. (cf. table 5.2) Second is the convergence

Table 5.2: Calculated ^{27}Al nuclear quadrupole coupling constants C_q in megahertz for corundum with $R_{mt} \times K_{max} = 4$ through 10 with k-points=100 and 400.

$R_{mt} \times K_{max}$	C_q, k-points=100	C_q, k-points=400
3.94	1.89	1.91
4.96	2.24	2.17
6.00	2.06	2.16
7.00	2.14	2.14
8.00	2.08	2.08
8.99	2.02	2.10
10.00	2.18	2.12

Table 5.3: Calculated ^{27}Al nuclear quadrupole coupling constants C_q in megahertz for corundum with k-points=1 through 1000 and $R_{mt} \times K_{max} = 8$.

k-points	C_q
1	3.44
200	2.10
300	2.09
400	2.07
600	2.07
800	2.07
1000	2.07

Table 5.4: Corundum ^{27}Al C_q in megahertz, from the current work FP-LAPW DFT calculations, from experiment and several other calculation methods. For calculations the value of C_q is reported using the most recent value of the quadrupole moment[103]. ^{a} Palmer[89] used the CRYSTAL computer program and does not report the value used for the quadrupole moment and the values reported here have not been converted to used the most recent quadrupole moment. ^{b} Vorotilova used the TEXAS computer program. P indicates point, D dipole, Q quarupole, O octupole, N local and NL nonlocal.

Reference	C_q/MHz	η
experiment		
Pound[140]	2.393	
Vosegaard[145]	2.403	0.009
Chang[141]	2.39	0
Gravina[154]	2.389	0.091
calculations		
Palmer[89],66 functions	1.5493^a	0
Palmer[89],106 functions	2.9273^a	0
Palmer[89],126 functions	2.3702^a	0
Salasco[89, 152],136 functions	1.58^a	0
Palmer[89],186 functions	2.9207^a	0
Vorotilova[149],basis I	-1.64^b	
Vorotilova[149],basis II	-2.06^b	

following from table in [155] and converted to MHz

Bersohn(1958),LS(P)	1.429	
Artman(1964),LS(P+D)	0.878	
Sharma(1964),LS(P+D)	0.434	
Taylor(1968),ODM(L)	2.557	
Hafner(1968),LS(P+D+Q)	2.093	
LS(P+D+Q)	1.929	
Hafner(1970),LS(P+D+Q+O)	1.832	
LS(P+D+Q+O)	2.368	
Sawatzky(1970),ODM(L)	2.292	
Sharma(1970),ODM(NL)	2.394	
Nagel,MsXα	2.149	

this work FP-LAPW DFT

($R_{mt}\times K_{max}$=8, 400k-pts)	2.12	0

of the EFG with the number of k-points, which are used to integrate the Brillouin zone. As the number of k-points approaches 400 the EFG is well converged. (cf. table 5.3) The EFG converges as the basis set size, as measured by $R_{mt} \times K_{max}$ and the integration, as measured by k-points increase, giving confidence in this method for largely ionic crystals such as corundum.

5.4   Conclusion

The good match of our calculation to the calculations and measurements of others and the EFG convergence with $R_{mt} \times K_{max}$ and convergence with k-points encourages us to look into the ability of the full-crystal FP-LAPW DFT method for calculating the full EFG tensors in andalusite.

CHAPTER 6

ANDALUSITE

6.1 Introduction

Andalusite (Al_2SiO_5) is an exciting system; it contains 5- and 6-coordinate aluminum sites, the EFG tensors are available from single-crystal NQR, and the structure is available from X-ray crystallography [156]. This offers an unparalleled chance to test the abilities of the embedded-cluster MO and the FP-LAPW DFT methods.

Embedded cluster MO [157, 81, 158, 159, 160] and full-crystal DFT [161, 77, 162, 118, 117, 79, 163] methods calculate EFG tensors of solids. The most accurate embedded-cluster MO calculations use a small, charged cluster embedded in a lattice of point charges. Despite the relatively small cluster size, this approach gives good results for sites with some symmetry (such as axial symmetry): CaF_2 [159] and spinels. [81] It is useful to investigate the limits of an embedded cluster MO method because it can be used to study disordered systems, as opposed to full-crystal DFT approaches. Full-crystal DFT studies are successful in studying periodic systems; they provide

a benchmark for the embedded-cluster MO methods, as well as allowing study of highly asymmetric sites. These two methods have been applied to a variety of Al-containing systems. Corundum, α-Al_2O_3, is a test of calculations for systems with an infinite covalent network [147, 148, 71, 151, 70, 146, 164] and the subject of the first complete measurement of the ^{27}Al chemical shift anisotropy. [145] Small clusters are models for aluminosilicates and zeolites. [144, 165, 166, 167] DFT methods provide impressive accuracy for the ^{25}Mg and ^{17}O EFGs in the mineral forsterite, Mg_2SiO. [117]

6.2   Method

Using 115K X-ray crystallography data, we simulate the crystal lattice with two regions:

1. a small, negatively charged AlO_x cluster and

2. surrounding point charges given their oxidation numbers -2, +3, and +4 for O, Al, and Si sites.

857 point charges surround the 6-coordinate site (AlO_6^{-9}) and 858 the 5-coordinate site (AlO_5^{-7}). Both are neutral with 864 sites or 27 unit cells (3x3x3). With Hartree-Fock (HF) calculations we investigate the effect of polarization and diffuse functions on EFGs. Other studies employ both types of functions to study ionic and partially ionic crystals [49, 168, 82, 88, 169, 104, 170].

Similar to corundum, we also study andalusite with full-crystal FP-LAPW DFT. Coordinates are from the 115 K X-ray crystallography. A total of 10,000 plane waves are used. The magnitude of the largest vector in the charge density Fourier expansion (G_{max}) is 24 a_o^{-1}. The convergence cut-off ($R_{mt} \times K_{max}$) for the LAPW expansion ranges from 3 to 6.76. The smallest

atomic sphere radius (R_{mt}) is 1.2 a.u.; the magnitude of the largest K vector (K_{max}) is 5.63333 a_o^{-1}. The irreducible wedge of the Brillouin zone is sampled with up to 128 k-points shifted away from high symmetry directions. Additional calculations with up to 512 k-points show no qualitative differences. Convergence is tested in the same way as corundum and the values are comparable to those in a forsterite study [117]. Total energy is shown to be self consistent to .0001 Ryd for three consecutive iterations. More details are available in the published paper [156].

Table 6.1: ^{27}Al nuclear quadrupole coupling constants C_q in megahertz and asymmetry parameters η for andalusite from a) single-crystal NQR experiment, b) embedded-cluster MO calculation and c) full-crystal FP-LAPW DFT calculation.

site	C_q			η		
	a	b	c	a	b	c
5-coord.	5.8323(8)	+5.338	+5.578	0.6733(2)	0.584	0.764
6-coord.	15.261(7)	+15.969	+13.639	0.1029(3)	0.139	0.094
$C_q(6/5)$	2.62	2.99	2.45			

6.3   Results and Discussion

The results of full-crystal DFT calculations are given in tables 6.3 and 6.5. The highest level calculations proved very useful for assigning the NMR spectra [156] and yielded EFG tensors that differ from experiment by less than 1.153 MHz for the a,a component of the 6-coordinate site and 0.326 MHz for the a,a component of the 5-coordinate site. Consequently, C_q, η, and the EFG orientation are in excellent agreement with experiment at both Al sites. For example, the orientations of the EFG tensors are calculated to within 0.17^o (6-coordinate) and 1.56^o (5-coordinate). Examining the angles between the principal axis system and the crystal axis system in tables 6.3 and 6.5,

Table 6.2: ^{27}Al NMR spectral parameters for andalusite 6-coordinate site, Al$_1$. ^{a} RHF single point calculations.

	6-coordinate, Al$_1$			
	C_q	η	$\angle \vec{q}_{zz}, a$	$\angle \vec{q}_{yy}, c$
experiment	15.261	0.1029	28.49	0.00
basis set	embedded-cluster MO^a			
STO-3G	-9.159	0.5856	17.45	5.69
6-31G	-12.739	0.4533	24.77	6.70
increasing polarization				
6-31G(d)	-13.243	0.3396	25.24	4.43
6-31G(2d)	-12.985	0.3657	24.85	6.08
6-31G(3d)	-14.157	0.2341	27.02	4.47
6-31G(3df)	-16.686	0.1389	27.73	59.47
diffuse + increasing polarization				
6-31+G	-11.456	0.6614	23.32	12.86
6-31+G(d)	-11.797	0.5408	23.90	7.83
6-31+G(2d)	-12.169	0.4752	23.54	8.35
6-31+G(3d)	-9.029	0.5257	13.69	63.99
6-31+G(3df)	-7.080	0.6195	18.32	47.10
6-311G	-14.819	0.4964	25.15	2.91
increasing polarization				
6-311G(d)	-15.355	0.4119	25.37	4.18
6-311G(2d)	-15.798	0.3538	25.45	7.38
6-311G(3d)	-15.696	0.1359	26.19	23.05
6-311G(3df)	-16.256	0.1376	26.40	34.31
diffuse + increasing polarization				
6-311+G	-14.111	0.3723	24.58	13.83
6-311+G(d)	-14.731	0.2996	24.89	10.09
6-311+G(2d)	-15.256	0.2395	25.21	7.66
6-311+G(3d)	-14.996	0.0439	26.10	4.20
6-311+G(3df)	-15.398	0.0510	26.24	35.82
correlation consistent polarization				
cc-pVDZ	-12.898	0.4036	24.74	4.15
cc-pVTZ	-16.165	0.2955	25.56	20.29

Table 6.3: ^{27}Al NMR spectral parameters for andalusite 6-coordinate site, Al$_1$. ^{b} V_{xc} = GGA96; G_{max}= 24 a_0^{-1}; k-points= 128.

	6-coordinate, Al$_1$			
	C_q	η	$\angle\vec{q}_{zz}, a$	$\angle\vec{q}_{yy}, c$
$R_{mt}{\times}K_{max}$	full crystal DFT^b			
3.00	11.638	0.455	31.95	90
3.96	11.546	0.085	28.08	0
4.97	13.933	0.063	28.78	0
5.60	13.491	0.092	28.69	0
6.76	13.639	0.094	28.67	0

shows that the calculated EFG tensor orientation is nearly superimposable with experiment. Andalusite is a favorable case for full-crystal DFT; the unit cell is mid-size, and the lattice structure is rigid, i.e., there is a complete absence of rotating water molecules or highly mobile cations.

The embedded-cluster MO results are also given in tables 6.2 and 6.4. While C_q and η are in good agreement with experiment, the EFG orientation is less accurate. For instance, the EFG orientation for the 5-coordinate site differs from experiment by about 45° for the angle between q_{yy} and the b-axis of the crystal. The best results are obtained with polarization and without diffuse functions. Adding polarization functions to 6-31G generally increases C_q at the 6-coordinate site and, at the 5-coordinate site, yields the correct sign only when f functions are added. The need for f functions is not surprising, since spherical harmonics up to l = 6 are needed in the full-crystal DFT calculations. Adding diffuse functions to the 6-31G basis set gives some improvement in the prediction of C_q and η for the 5-coordinate site, but seriously degrades the accuracy for the 6-coordinate site. The same series of polarization and diffuse functions were added to 6-311G, however, the sign remained negative for the 5-coordinate site. A similar change in

Table 6.4: ^{27}Al NMR spectral parameters for andalusite 5-coordinate site, Al_2. ^{a} RHF single point calculations.

basis set	5-coordinate, Al_2				
	C_q	η	$\angle\vec{q}_{zz}, c$	$\angle\vec{q}_{yy}, b$	$\frac{C_q Al_1}{C_q Al_2}$
experiment	5.832	0.6733	0.00	13.31	2.62
basis set	embedded-cluster MO^a				
STO-3G	10.171	0.3796	74.41	68.73	-0.90
6-31G	5.903	0.4930	75.77	89.34	-2.16
increasing polarization					
6-31G(d)	7.615	0.3652	74.80	75.18	-1.74
6-31G(2d)	5.293	0.7149	73.62	85.46	-2.45
6-31G(3d)	4.698	0.9659	72.31	88.74	-3.01
6-31G(3df)	-5.578	0.5841	18.50	59.51	2.99
diffuse + increasing polarization					
6-31+G	4.201	0.4220	61.41	56.13	-2.73
6-31+G(d)	5.424	0.4696	56.60	36.58	-2.18
6-31+G(2d)	5.438	0.3372	67.71	61.26	-2.24
6-31+G(3d)	-4.586	0.7755	21.04	70.18	1.97
6-31+G(3df)	-5.261	0.5473	22.91	46.28	1.35
6-311G	7.427	0.7679	76.64	89.17	-2.00
increasing polarization					
6-311G(d)	8.308	0.5272	75.97	85.86	-1.85
6-311G(2d)	7.387	0.5630	74.64	83.98	-2.14
6-311G(3d)	5.732	0.3728	67.61	66.04	-2.74
6-311G(3df)	5.501	0.5170	67.66	73.33	-2.96
diffuse + increasing polarization					
6-311+G	5.588	0.2577	63.10	57.12	-2.53
6-311+G(d)	5.692	0.2723	61.68	53.56	-2.59
6-311+G(2d)	5.863	0.3650	61.00	42.27	-2.60
6-311+G(3d)	5.479	0.5868	64.55	65.95	-2.74
6-311+G(3df)	5.517	0.5971	65.51	69.48	-2.79
correlation consistent polarization					
cc-pVDZ	8.280	0.4186	78.67	86.53	-1.56
cc-pVTZ	-4.205	0.8582	25.58	74.41	3.84

Table 6.5: ^{27}Al NMR spectral parameters for andalusite 5-coordinate site, Al_2. ^{b} V_{xc} = GGA96; G_{max}= 24 a_0^{-1}; k-points= 128.

	5-coordinate, Al_2				
	C_q	η	$\angle \vec{q}_{zz}, c$	$\angle \vec{q}_{yy}, b$	$\dfrac{C_q Al_1}{C_q Al_2}$
$R_{mt} \times K_{max}$			full crystal DFT^b		
3.00	1.311	0.706	90	13.17	8.88
3.96	5.034	0.883	0	13.48	2.29
4.97	5.564	0.717	0	14.19	2.50
5.60	5.477	0.783	0	14.68	2.46
6.76	5.578	0.764	0	14.31	2.45

sign is observed for the 5-coordinate site with the Correlation Consistent Polarized Valence Double (cc-pVDZ) and Triple (cc-pVTZ) Zeta [171, 172] basis sets. These differ in contraction scheme and by the addition of an f function. On the basis of these considerations, we choose the 6-31G(3df) as the best basis set for andalusite.

The source of the difficulty in calculating accurately C_q, η, and the EFG orientation at the 5-coordinate site becomes apparent upon examination of the two largest eigenvalues of the EFG tensor. These are nearly the same in magnitude but opposite in sign; experimentally, $|q_{yy}/q_{zz}| = 0.84$. For basis sets without sufficient polarization, the eigenvector whose direction most closely parallels the experimental element qzz has the second largest magnitude, rather than the largest magnitude and is thus identified as q_{yy}. Hence, very similar calculated EFG tensors (in the crystal coordinate system) may have the incorrect sign for C_q, depending on the relative values of q_{yy} and q_{zz}. This can be seen by examining the angle between q_{zz} and the a-axis. Only with polarization is the ordering of the eigenvalues correct, and even then the orientation of the EFG tensor is not determined well enough to completely interpret the single-crystal NMR results.

6.4   Conclusion

This work demonstrates that full-crystal DFT and embedded-cluster MO methods, combined with excellent NMR experiments, can be used to assign EFG tensors to low-symmetry sites. This is an important first step in developing methods for interpreting ^{27}Al NMR spectra in terms of the aluminum coordination environment. The 6-coordinate site experimental results agree with the previous work of Hafner et al., [173] and the EFG tensor assignment is the same as found in the point charge analysis of Raymond. [174] The 5-coordinate site is assigned, many years after its first observation, on the basis of full-crystal DFT calculations. This is the first 5-coordinate aluminum site to be fully studied and assigned by NMR. The signs of the quadrupole coupling constants are determined for both the 6- and 5-coordinate sites.

The agreement between the experimental EFG orientation and that from the full crystal density functional theory is remarkably close, differing by only 0.17^o for the 6-coordinate site and 1.56^o for the 5-coordinate site. The embedded-cluster MO results are significantly less accurate for orientation with errors exceeding 45°. This data shows the greater reliability of the full-crystal FP-LAPW DFT for tensor orientations compared to the single-molecule + point charge. Using a more accurate and time-consuming method for point charge inclusion may improve the single-molecule embedded cluster MO method.

CHAPTER 7

ANDALUSITE, SILLIMANITE AND KYANITE

The temperature dependence of the EFG tensors for andalusite, sillimanite and kyanite was studied with full potential linearized augmented plane wave implementation of density functional theory. Andalusite, sillimanite and kyanite are aluminosilicates and are three polymorphs of Al_2SiO_5 containing Al sites with four, five and six oxygen coordination in tetrahedral, octahedral and trigonal bipyramidal arrangements respectively. Calculations used crystal structures available from the literature for -183, 25, 400, 600, 800 and 1000 ^oC for andalusite; 25, 400, 600, 800 and 1000 ^oC for sillimanite; and 25, 400, 600 ^oC for kyanite. ^{27}Al NMR spectral parameters reported are the quadrupole coupling constant, the asymmetry parameter and the angles describing the orientation between the principal axis system and crystal axis system of the electric-field-gradient tensor. Calculated ^{27}Al NMR spectral parameters for 34 different aluminum sites and assignments of experimen-

tal tensors to sites are reported. Complete EFG tensors for 34 aluminum, 17 silicon and 74 oxygen sites are available as supplementary information. Relationships of these parameters to temperature, polyhedral volume, longitudinal and shear strain are discussed.

7.1 Introduction

NMR spectroscopy is a powerful tool for analyzing the structure of materials [119, 175, 120]. NMR can probe the interaction between the nuclear-electric-quadrupole moment and the EFG. The dependence of NMR signal on the EFG at an atomic site makes this technique a sensitive probe of local geometric and electronic structure. Applications of NMR spectroscopy range widely from determining dispersal in HIPS of brominated aromatics [4, 176], found in flame retardants, to elucidation of structure in aluminum containing materials such as mononuclear 7-azaindole aluminum complexes [177], ethylaluminum halides [178], aluminum alkoxides [179], cements and methylalumoxane (MAO) [180, 181, 182, 183, 184, 185, 186, 187, 188, 189]. Analysis of NMR spectra requires the knowledge of the EFG tensor at an atomic site. For sites of high symmetry, it is possible to distinguish between sites with different coordination numbers using simple models for interatomic interactions and symmetry considerations alone. However, for many materials of interest, asymmetries make it difficult or impossible to predict an EFG tensor without the use of ab initio calculations.

There are three distinct ab initio approaches for EFG tensor calculation: gas phase MO calculations, embedded cluster MO calculations and full crystal density functional calculations. Gas phase calculations are most useful for molecular solids where intermolecular interactions are relatively small perturbations on the dominant intramolecular forces. [190, 57] Cluster models

are used for ionic solids which use the target atom surrounded by the set of neighboring atoms (typically just the nearest neighbor atoms) embedded in a set of point charges [156] and multi-molecule systems to investigate intermolecular interactions such as hydrogen bonding [57, 58]. Full crystal density functional calculations typically use the FP-LAPW implementation of density functional theory [113, 114] and require knowledge of the crystal structure of the solid. In general, the various methods can accurately distinguish between sites with different coordination numbers. However, quantitative accuracy is limited to approximately 10 percent. When the crystal structure is known, FP-LAPW offers a distinct advantage with its ability to include the full crystal symmetry of the lattice. In an earlier publication, we found that ^{27}Al NMR spectral parameters (especially axis orientation) from FP-LAPW match experiment more closely than embedded cluster calculations. FP-LAPW has been used with considerable success to determine EFG parameters in a variety of solids.

There are three empirical correlations that have been suggested between local geometric structure and the ^{27}Al NMR spectral parameters or EFG: polyhedral volume, longitudinal strain and shear strain. Ab initio methods have significant computational requirements, so it is useful to investigate the utility of the three empirical correlations to match experiment. A useful test is to study the EFG tensor in known structures at a series of temperatures.

Variable temperature NMR studies exist for several materials including ruby [191], and rubidium salts [192]. The aluminosilicates are particularly interesting because they contain a variety of coordination sites with different polyhedral distortion. Ghose et al. [193], Weller et al. [194] and Engelhardt et al. [195] have studied spectra-structure relationships with polyhedral distortion [196] for aluminates. The temperature dependence of

the nuclear quadrupole interaction (EFG, C_q, or η) has been measured for various quadrupolar nuclei of inorganic compounds and minerals. Usually C_q decreases as temperature increases, as seen for ^{27}Al ($I = \frac{5}{2}$) in $AlPO_4$ tridymite [197], ^{14}N ($I = 1$) in different para-substituted anilines [198], two ^{87}Rb ($I = \frac{3}{2}$) in Rb_2SO_4, one Rb in $RbClO_4$ and two of the three Rb sites in $RbNO_3$ [192]. The linear relationships have been attributed to a linear increase of the lattice constant with increasing temperature. However, one Rb site in $RbNO_3$ exhibits a nonmonotonic behavior, with C_q decreasing with increasing temperature to a minimum at 20^oC then C_q increases with increasing temperature above 20^oC. This cannot be explained by thermal expansion of the unit cell alone and is probably associated with a reorientation of individual NO_3 groups which affect the Rb EFG in a different manner. Another explanation could be the in-plane rotations of the NO_3 groups with increasing temperature which could also affect the EFG. [192] Likewise, C_q also increases with increasing temperature for the ^{27}Al site in a synthetic ruby crystal (Al_2O_3) [191] possibly due to significant changes in lattice vibration frequencies with temperature. Thus, while the increase of the lattice constant with increasing temperature is a significant factor in the temperature dependence of the EFG, other interactions can offset this effect.

Andalusite, sillimanite and kyanite are well-characterized [199, 200, 201, 202]. They provide a well-defined series of aluminum containing solids for which structures are known at a number of temperatures [203]. The coordination of the Al atoms ranges from 4 to 6 O atoms and provides a stringent test for ab initio methods. Andalusite contains two crystallographically distinct aluminum sites — a six-coordinate, octahedral site, Al_1, and a five-coordinate, distorted trigonal bipyramidal site, Al_2. Sillimanite also contains two crystallographically distinct aluminum sites — a six-coordinate, octahe-

dral site, Al_1, and a four-coordinate, tetrahedral site, Al_2. Kyanite contains four crystallographically distinct aluminum sites and all of them are octahedrally coordinated with six oxygen atoms — Al_1, Al_2, Al_3 and Al_4.

Single temperature ^{27}Al NMR spectral parameters are available from NMR experiments for andalusite [156, 204], sillimanite, kyanite [173, 205, 206, 207], and a similar structure with an AlO_6 site, ruby [191]. Kyanite presents the most difficult case to experimentalists in assigning NMR signals to Al sites because all four Al sites have the same low symmetry (C_1). Indeed, the only assignment they make is to point out that the strongly distorted (Hafner Al(4)) site possesses both the shortest and one of the longest Al–O distances in aluminosilicate minerals and as a result ought to correspond to one of the tensors with the largest eigenvalues (Hafner tensors I and II) [173]. Nuclear quadrupole interaction data is available from calculations for andalusite [156].

Calculations data for andalusite, sillimanite and kyanite also exits. Raymond predicts EFGs using a point charge model [174]. During preparation of this work we were made aware of a recent submission regarding calculations of andalusite, sillimanite and kyanite for structures corresponding to a single temperature [208].

In this paper, we use FP-LAPW to calculate ^{27}Al NMR spectral parametersand assign the EFG tensors to 34 Al sites in the aluminosilicates. For the four Al sites in kyanite this is the first definitive assignment. Finally, we examine the temperature dependence of the ^{27}Al NMR spectral parameters and the utility of three proposed correlations with geometric structure.

7.2   Method

We study the three polymorphs of Al_2SiO_5 with density functional theory
[45, 46] in a manner similar to our single temperature study of andalusite
[156]. We now examine EFGs at different temperatures by using X-ray crys-
tallography structures available from the literature [203, 156]. These struc-
tures were taken at -183, 25, 400, 600, 800 and 1000 ^oC for andalusite; 25,
400, 600, 800 and 1000 ^oC for sillimanite; and 25, 400, 600 ^oC for kyanite. We
calculate EFGs using the WIEN [113] computer program. This program im-
plements full-crystal density functional theory with the FP-LAPW method
[114]. Exchange and correlation are included with the generalized gradi-
ent approximation (GGA) [115, 116]. GGA is preferred for EFGs [117, 118].
Linear variation of the LAPW provides the solution to the Kohn-Sham equa-
tions. The FP-LAPW method divides the unit cell of a crystal into two parts:
1) spheres around the atoms and 2) an interstitial region. Inside the atomic
spheres is a linear combination of the product of radial functions and spheri-
cal harmonics, while a plane wave expansion is used in the interstitial region.
This is a full potential method; no shape approximations are made for the
potential or the electronic charge. Computer memory size limits the plane
wave expansion; for each k-point plane wave coefficients must be calculated
by diagonalizing a matrix with dimensions equal to the number of K vectors.

7.2.1   Parameters

The convergence cut-off for the expansion of the augmented plane wave basis
set is a measure of its quality or completeness. The following parameters are
the same for all temperatures and all compounds unless otherwise specified.
We use a total of 10,000 plane waves. The magnitude of the largest vector
in the charge density Fourier expansion (G_{max}) is $24.0a_o^{-1}$.

Table 7.1: The matrix size, $R_{mt} \times K_{max}$, in $Bohr * Ry^{\frac{1}{2}}$ for the Al_2SiO_5 polymorphs at each temperature, T.

$T/^{\circ}C$	andalusite	sillimanite	kyanite
-183	5.51		
25	5.51	5.55	5.79
400	5.49	5.54	5.77
600	5.48	5.54	5.75
800	5.48	5.53	
1000	5.46	5.53	

The sphere radii, R_{mt}, encompass a majority of the core electron density, allowing the valence density to be represented primarily by plane waves. The sizes for R_{mt} are 1.65 for all Al; 1.8 for all Si; and 1.2, 1.16, 1.06 $Bohr$ for O in andalusite, sillimanite and kyanite respectively. The smallest atomic sphere radius (R_{mt}) is O in all three polymorphs. The product of the smallest R_{mt} and the magnitude of the largest K-vector, K_{max} determines the combined LAPW basis expansion cut-off. The unit cell dimensions combined with user input determine the magnitude of the largest K-vector. Table 7.1 shows the $R_{mt} \times K_{max}$ values that we use in our calculations.

75 k-points sample the irreducible wedge of the Brillouin zone; they are shifted away from high symmetry directions for efficiency. Additional calculations with up to 512 k-points show no qualitative differences. For the atomic spheres spherical harmonics are included up to $l = 6$ with lm_{max} set to 10. For convergence the charge is required to be self consistent to 0.0001 for three consecutive iterations, followed by self consistency in the forces to 1 $mRy/a.u.$ for three consecutive iterations.

A single relativistic calculation on andalusite at the -183$^{\circ}C$ structure showed only $\approx \frac{1}{5}MHz$ higher for the magnitude of the largest component in the diagonalized electric-field-gradient tensor; the orientation remained true up to 10^{-5}. All other calculations are non-relativistic.

7.2.2 Input

Nuclear coordinates are from X-ray crystallography [203, 156] and we designate Al sites in the same order (i.e Al_1, Al_2, Al_3, Al_4). Tables 7.2 and 7.3 details the environments due to other nuclei at each symmetry unique Al site. Each polymorph contains an Al in six-coordination and a Si in four-coordination. The coordination of the other Al atom is four in sillimanite, five in andalusite and six in kyanite. At each temperature there are 7 symmetry unique atoms in andalusite and sillimanite, while kyanite has 16.

Table 7.2: Point symmetry and Al–O coordination. Point symmetry and coordination of Al with O for symmetry unique Al sites in andalusite, sillimanite and kyanite. Coordination of Al with O is the total number of O less than 2.5Å from Al. In sillimanite there is an additional O greater than 2.5Å but less than 3.0Å from the Al_2 site. In parenthesis is the number of O with a unique Al–O distance. The largest distance change with temperature is a percentage, $\Delta d(Al-O_X)$.

site	point symmetry	coord.	$\Delta d(Al\text{-}O_X)$ with T/%
		andalusite	
Al_1	$2, C_2$	6(3)	$+3.2, O_D$
Al_2	m, C_s	5(3)	$+0.7, O_C$
		sillimanite	
Al_1	$-1, C_i$	6(3)	$+1.2, O_D$
Al_2	m, C_s	4(3)	$-\frac{1}{2}, O_C$
		kyanite	
Al_1	$1, C_1$	6(6)	$+1, O_H, O_G$
Al_2	$1, C_1$	6(6)	$+ \approx \frac{1}{2}, all$
Al_3	$1, C_1$	6(6)	$+1, O_F$
Al_4	$1, C_1$	6(6)	$+1, O_A$

7.3 Results

We report the calculated ^{27}Al NMR spectral parameters and the ratio of C_q between sites in Tables 7.4–7.7. Our calculations use the Al coordinates listed in Bryant [156] and Winter [203] except for andalusite Al_2 ($25 - 1000^\circ C$) for

Table 7.3: Nearest neighbor structure. Atoms neighboring each site are shown in order of increasing distance. Two atoms equidistant from Al are prefixed by the numeral two. The subscript on each atom identifies symmetry unique atoms and is unique for each polymorph.

site	$d(\text{Al-O}) < 2.5\text{Å}$	$2.5\text{Å} < d(\text{Al-O}) < 3.0\text{Å}$
	andalusite	
Al_1	$2\text{O}_A, 2\text{O}_B, 2\text{O}_D$	Al_1, Al_1
Al_2	$2\text{O}_D, \text{O}_A, 2\text{O}_C$	Al_2
	sillimanite	
Al_1	$2\text{O}_B, 2\text{O}_A, 2\text{O}_D$	2Al_1
Al_2	$\text{O}_C, \text{O}_B, 2\text{O}_D$	$\text{O}_A, 2\text{Si}$
	kyanite	
Al_1	$\text{O}_K, \text{O}_M, \text{O}_B, \text{O}_F, \text{O}_G, \text{O}_H$	$\text{Al}_2, \text{Al}_2, \text{Al}_3, \text{Al}_4, \text{Al}_3,$
Al_2	$\text{O}_C, \text{O}_D, \text{O}_F, \text{O}_M, \text{O}_K, \text{O}_B$	$\text{Al}_1, \text{Al}_1, \text{Al}_4, \text{Al}_3$
Al_3	$\text{O}_E, \text{O}_F, \text{O}_G, \text{O}_C, \text{O}_F, \text{O}_B$	$\text{Al}_4, \text{Al}_2, \text{Al}_1, \text{Al}_3, \text{Al}_1$
Al_4	$\text{O}_A, \text{O}_B, \text{O}_H, \text{O}_D, \text{O}_E, \text{O}_A$	$\text{Al}_4, \text{Al}_3, \text{Al}_2, \text{Al}_1$

which we report at $(\frac{1}{2} + x, \frac{1}{2} - y, \frac{1}{2} - z)$ to be consistent with our previous work [156]. The supplementary material contains the full EFG tensors for all 103 sites (Al, Si and O) along with their corresponding crystal coordinates.

7.3.1 Andalusite

Calculated and experimental ^{27}Al NMR spectral parameters for andalusite are in Table 7.4. Andalusite's Al_1 site is coordinated octahedrally with six O atoms and is the most symmetric Al site in all of the polymorphs. The site is of C_2 symmetry. The orientation of the EFG principle axes ($\vec{q}_{xx}$, $\vec{q}_{yy}$ and $\vec{q}_{zz}$) with respect to the crystal axes ($\vec{a}, \vec{b}, \vec{c}$) is: $\vec{q}_{xx}$ is closest to $\vec{b}$, $\vec{q}_{yy}$ is closest to $\vec{c}$ and $\vec{q}_{zz}$ is closest to $\vec{a}$. The angles of $\vec{q}_{xx}$ with $\vec{b}$ and q_{zz} with $\vec{a}$ are identical at each temperature, decreasing only slightly with increasing temperature from 28.71 to 28.86°. The angle of $\vec{q}_{yy}$ with $\vec{c}$ is exactly 0°. The middle magnitude eigenvector, $\vec{q}_{yy}$, is directed toward the next Al_1 atom and along the c axis, with an angle of 0 for all temperatures.

The largest magnitude eigenvector, $\vec{q}_{zz}$, points toward O_D, with an angle of approximately two degrees. There is almost no change with temperature in the orientation of the EFG principal axis system with respect to the crystal axis system; the angles of the eigenvectors with the crystal axis system change less than one percent. With increasing temperature the site undergoes uneven expansion; the distances from Al_1 to $O_B(< 0.2\%)$ and $O_A(< 0.1\%)$ are nearly constant relative to the pronounced elongation of the distance from $Al_1 (3.3\%)$ to O_D [203].

The Al_2 site in andalusite is five coordinate with C_s symmetry. Five coordinate Al sites are rare. The angles between the EFG principle axes $(\vec{q}_{xx}, \vec{q}_{yy}$ and $\vec{q}_{zz})$ and the crystal axes $(\vec{a}, \vec{b}, \vec{c})$ are: $\vec{q}_{xx}$ is closest to $\vec{a}$, $\vec{q}_{yy}$ is closest to $\vec{b}$ and $\vec{q}_{zz}$ is closest to $\vec{c}$. The angles of $\vec{q}_{xx}$ with $\vec{a}$ and q_{yy} with $\vec{b}$ are identical at each temperature and range 15.64–17.56°. The angle of $\vec{q}_{zz}$ with $\vec{c}$ is exactly 0°. The eigenvector $\vec{q}_{xx}$ is near O_C with an angle ranging from 5.6–7.5°, $\vec{q}_{yy}$ is near O_A with an angle ranging from 2.4–4.2°, and $\vec{q}_{zz}$ makes a perfect 90°angle with O_C and the next Al_2.

7.3.2 Sillimanite

Calculated and experimental ^{27}Al NMR spectral parameters for sillimanite are shown in Table 7.5. Small but unusual changes in the local coordination structure of the Al sites in sillimanite obscure correlations. The local coordination structure of the two Al atoms in sillimanite is different from all the other polymorphs studied in that there is an uneven change in Al–O distances. For the other polymorphs there is either little change or a uniform increase or decrease. For the sillimanite Al_1 site one distance $(Al_1–O_A)$ increases to a maximum at $800°C$ and then decreases at $1000°C$, while all the other Al_1-O distances increase to a maximum at $1000°C$. For the sillimanite

Table 7.4: Andalusite ^{27}Al NMR spectral parameters for Al_1 and Al_2 [27]Al quadrupole coupling constants (C_q in megahertz), EFG asymmetries (η) and angles in degrees between the crystal and principal axis systems for six temperatures in degrees Celsius (T). The values from experiment are also shown for comparison. [a] ^{27}Al NMR from [156] [b] ^{27}Al NMR from [209], temperature not reported. N.B. an experiment does not determine C_q sign.

$T/^\circ C$	C_q	η	$\angle\vec{q}_{xx}, b$	$\angle\vec{q}_{yy}, c$	$\angle\vec{q}_{zz}, a$
			six-coordinate Al_1		
-183	14.176	0.071	28.80	0.00	28.80
25	14.507	0.073	28.71	0.00	28.71
400	15.422	0.071	28.71	0.00	28.71
600	15.882	0.075	28.72	0.00	28.72
800	16.248	0.075	28.66	0.00	28.66
1000	16.727	0.077	28.86	0.00	28.86
			experiment		
25 [a]	±15.261	0.103	28.50	0.00	28.50
			experiment tensor I[b]		
[b]	±15.733	0.035	28.21	0.00	28.21

$T/^\circ C$	C_q	η	$\angle\vec{q}_{xx}, a$	$\angle\vec{q}_{yy}, b$	$\angle\vec{q}_{zz}, c$	$\frac{C_q(Al_1)}{C_q(Al_2)}$
			five-coordinate Al_2			
-183	5.668	0.750	14.86	14.86	0.00	2.50
25	5.487	0.702	15.64	15.64	0.00	2.64
400	5.181	0.692	15.95	15.95	0.00	2.98
600	5.014	0.658	15.63	15.63	0.00	3.17
800	4.802	0.688	15.91	15.91	0.00	3.38
1000	4.537	0.652	17.56	17.56	0.00	3.69
			experiment			
25 [a]	±5.832	0.673	15.87	15.87	0.00	±2.62
			experiment tensor II[b]			
[b]	±5.900	0.708	16.60	16.60	0.00	±2.67

Al$_2$ site the Al$_2$–O$_D$ distance increases, decreases very slightly at 600°C and increases again at 800 and 1000°C. These uneven changes are small, relative to the Al–O distance changes at other sites (cf. table 7.2), however they still effect the calculated EFG and make correlations unclear.

Table 7.5: Sillimanite ^{27}Al NMR spectral parametersfor Al$_1$ and Al$_2$ ^{27}Al quadrupole coupling constants (C_q in megahertz), EFG asymmetries (η) and angles in degrees between the crystal and principal axis systems for five temperatures in degrees Celsius (T). The values from experiment are also shown for comparison. ^{a} ^{27}Al NMR from [210], temperature not reported. N.B. an experiment does not determine C_q sign.

$T/°C$	C_q	η	$\angle\vec{q}_{xx}, a$	$\angle\vec{q}_{yy}, b$	$\angle\vec{q}_{zz}, c$
			six-coordinate Al$_1$		
25	-8.259	0.495	45.26	31.19	32.77
400	-8.615	0.534	44.96	30.61	32.91
600	-8.668	0.555	45.17	30.94	32.87
800	-8.911	0.561	45.33	30.95	33.09
1000	-8.890	0.585	44.81	30.49	32.74
			experiment tensor I^a		
a	±8.934	0.462	44.21	30.88	31.97

$T/°C$	C_q	η	$\angle\vec{q}_{xx}, c$	$\angle\vec{q}_{yy}, b$	$\angle\vec{q}_{zz}, a$	$\frac{C_q(\mathrm{Al}_1)}{C_q(\mathrm{Al}_2)}$
			four-coordinate Al$_2$			
25	-6.269	0.557	0.00	15.27	15.27	1.32
400	-6.315	0.549	0.00	16.48	16.48	1.36
600	-6.411	0.541	0.00	16.88	16.88	1.35
800	-6.318	0.559	0.00	17.84	17.84	1.41
1000	-6.347	0.505	0.00	18.98	18.98	1.40
			experiment tensor II^a			
a	±6.774	0.531	0.00	14.59	14.59	±1.32

The sillimanite Al$_1$ atom is coordinated with six O atoms and has C_i symmetry. The $\vec{q}_{xx}$ eigenvector is closest to the a axis, $\vec{q}_{yy}$ to b and $\vec{q}_{zz}$ to c. The $\vec{q}_{xx}$, a angle varies between 44.81 and 45.33°, $\vec{q}_{yy}$, b between 30.49 and 31.19°, $\vec{q}_{zz}$, c between 32.74 and 33.09°. The $\vec{q}_{xx}$ eigenvector is close to Si ($\approx 8°$), $\vec{q}_{yy}$ to O$_D$ ($\approx 2.4 - 2.8°$) and $\vec{q}_{zz}$ to O$_A$ atom ($\approx 6°$).

The sillimanite Al_2 site is coordinated with four oxygen atoms, though a fifth oxygen atom is between 2.5 and 3.0Å. The site is of C_s symmetry. $\vec{q}_{xx}$ lies along c for all temperatures, the $\vec{q}_{yy}$,b and $\vec{q}_{zz}$,a angles are identical at each temperature, with increasing temperature they increase a little less than 4°, from 15.27 to 18.98^o.

7.3.3 Kyanite

Calculated and experimental ^{27}Al NMR spectral parameters for kyanite are in Table 7.6. The Al_1 site is the only kyanite site with a positive C_q. For the kyanite Al_1 site, the $\vec{q}_{xx}$ EFG eigenvector is closest to the a crystal axis, $\vec{q}_{yy}$ to c and $\vec{q}_{zz}$ to b. The angles increase with increasing temperature: $\vec{q}_{xx}$, a from 8.59 to 10.71^o; $\vec{q}_{yy}$, c from 15.46 to 16.89^o; $\vec{q}_{zz}$, b from 12.87 to 13.10^o.

The Al_2, Al_3 and Al_4 are the kyanite octahedral sites with $C_q < 0$. (The C_q for Al_1 in sillimanite is also negative.) All have C_1 symmetry.

For kyanite Al_2 site, the $\vec{q}_{xx}$ EFG eigenvector is closest to the c crystal axis, $\vec{q}_{yy}$ to a and $\vec{q}_{zz}$ to b. The $\vec{q}_{yy}$, a angle increases with temperature from 14.17 to 16.78^o. The other two angles do not. The $\vec{q}_{xx}$, c angle varies between 25.19 and 26.91^o, and the $\vec{q}_{zz}$, b angle varies from 19.60 to 21.50^o. For kyanite Al_3 site, the $\vec{q}_{xx}$ EFG eigenvector is closest to the c crystal axis, $\vec{q}_{yy}$ to a and $\vec{q}_{zz}$ to b. The $\vec{q}_{zz}$, b angle decreases with increasing temperature from 15.35 to 13.36^o. The other two angles do not. They vary between 18.35 to 19.70^o ($\vec{q}_{xx}$, c) and 13.04 to 13.50^o ($\vec{q}_{yy}$, a). For kyanite Al_4 site, the $\vec{q}_{xx}$ EFG eigenvector is closest to the c crystal axis, $\vec{q}_{yy}$ to a and $\vec{q}_{zz}$ to b. The $\vec{q}_{xx}$, c and $\vec{q}_{yy}$, a angles decrease with increasing temperature, 9.72 to 7.40 and 6.72 to 2.96^o respectively. The $\vec{q}_{zz}$, b angle varies from 6.81 to 7.52^o.

For kyanite, there is no apparent correlation between the directions of the eigenvectors and individual atoms, as there is in andalusite and sillimanite.

Table 7.6: Kyanite ^{27}Al NMR spectral parameters Kyanite Al_1, Al_2, Al_3 and Al_4 [27]Al quadrupole coupling constants (C_q in megahertz), EFG asymmetries (η) and angles in degrees between the crystal and principal axis systems for five temperatures in degrees Celsius (T). Values from experiment are shown for comparison. [a] ^{27}Al NMR from [210], temperature not reported. N.B. experiment does not determine C_q sign.

$T/°C$	C_q	η	$\angle \vec{q}_{xx}, a$	$\angle \vec{q}_{yy}, c$	$\angle \vec{q}_{zz}, b$
			six-coordinate Al_1		
25	9.076	0.286	8.59	15.46	12.87
400	9.366	0.279	10.62	16.77	13.01
600	9.529	0.273	10.72	16.89	13.10
			experiment tensor I[a]		
a	±10.040	0.265	15.42	20.28	13.59

$T/°C$	C_q	η	$\angle \vec{q}_{xx}, c$	$\angle \vec{q}_{yy}, a$	$\angle \vec{q}_{zz}, b$
			six-coordinate Al_2		
25	-3.108	0.822	25.61	14.17	21.51
400	-3.361	0.801	25.19	15.99	19.60
600	-3.107	0.841	26.91	16.78	21.27
			experiment tensor IV[a]		
a	±3.700	0.897	25.18	20.12	14.98

$T/°C$	C_q	η	$\angle \vec{q}_{xx}, c$	$\angle \vec{q}_{yy}, a$	$\angle \vec{q}_{zz}, b$
			six-coordinate Al_3		
25	-5.285	0.832	19.71	13.05	15.35
400	-5.809	0.786	19.51	13.50	14.52
600	-6.107	0.791	18.35	13.24	13.37
			experiment tensor III[a]		
a	±6.530	0.590	17.25	11.76	12.58

$T/°C$	C_q	η	$\angle \vec{q}_{xx}, c$	$\angle \vec{q}_{yy}, a$	$\angle \vec{q}_{zz}, b$
			six-coordinate Al_4		
25	-8.097	0.466	9.72	6.73	7.13
400	-8.505	0.453	8.10	3.35	7.53
600	-8.892	0.431	7.40	2.95	6.81
			experiment tensor II[a]		
a	±9.370	0.387	7.25	2.56	6.78

Table 7.7: Ratios of C_q among Al sites in kyanite, denoted $X:Y$ for $\frac{C_q(\mathrm{Al}_x)}{C_q(\mathrm{Al}_y)}$. [a] $^{27}\mathrm{Al}$ NMR from [210], temperature not reported. N.B. because the experiment does not determine C_q sign the sign of the ratio is also not determined.

kyanite C_q ratios $\frac{C_q(\mathrm{Al}_x)}{C_q(\mathrm{Al}_y)} \equiv X:Y$						
$T/^{\circ}C$	$1:2$	$1:3$	$1:4$	$2:3$	$2:4$	$3:4$
25	-2.92	-1.72	-1.12	0.59	0.38	0.65
400	-2.79	-1.61	-1.10	0.58	0.40	0.68
600	-3.07	-1.56	-1.07	0.51	0.35	0.69
			experiment			
a	±2.71	±1.54	±1.07	±.57	±.57	±.70

7.4   Discussion

7.4.1   Single Temperature Accuracy

The comparison of calculated and experimental $^{27}\mathrm{Al}$ NMR spectral parameters demonstrates that the calculated EFG tensors are accurate enough to distinguish between the 8 different sites.

The C_q ratio is independent of Q and as a result has fewer uncertainties, making it a good metric with which to measure how well calculations match experiment. Variable temperature NMR data does not exist for these $\mathrm{Al_2SiO_5}$ polymorphs, but single temperature data is available and we include that in the tables.

The ten calculated $^{27}\mathrm{Al}$ NMR spectral parameters for andalusite agree well with experiment (cf. table 7.4). The C_q magnitudes, EFG asymmetry and the three angles between the axis system are close in value and confirm the site assignments we made in previous work [156]. The angles differ from experiment by less than 1.5%. The ratio of quadrupole coupling constants of $\mathrm{Al_1}$ and $\mathrm{Al_2}$ in andalusite, $\frac{C_q(\mathrm{Al_1})}{C_q(\mathrm{Al_2})}$, provides a unitless comparison free from any uncertainty which may be in the quadrupole moment, Q. The ratio

from calculations at the $25^\circ C$ structure (2.64) compares well to that from experiment (2.62 and 2.67 within 1%).

The calculated ^{27}Al NMR spectral parameters for sillimanite agree well with experiment (cf. table 7.5). The EFG asymmetry and the three angles between the axis system are close in value. The magnitudes of C_q are not in as good of agreement as those for andalusite. The angles differ from experiment by less than 2.5% for Al_1 and less than 5% for Al_2. These parameters confirm the site assignments made by Raymond et al. [210]. The C_q ratios of Al_1 and Al_2 in sillimanite, $\frac{C_q(Al_1)}{C_q(Al_2)}$, from calculations and experiment are the same at 1.32. The ratios agree much better than the magnitudes of C_q which differ by as much as 7.6%.

Kyanite is a much stiffer test of calculations; there are four Al each with very low C_1 symmetry in kyanite, while there are only two Al sites — all with higher symmetry — in andalusite and sillimanite. The calculated ^{27}Al NMR spectral parameters for kyanite agree with experiment in only a qualitative manner(cf. table 7.6). The EFG asymmetry and the magnitude of C_q are similar in value. The three angles between the axis system do not agree nearly as well as those of sillimanite or andalusite. The qualitative agreement is adequate for assignment of the EFG tensors All the C_q ratios show good agreement with experiment differing by less than 2%, except the $\frac{C_q(Al_2)}{C_q(Al_4)}$ ratio, which differs by more than 30%. We attribute the lack of good quantitative agreement to the low symmetry.

7.4.2 Temperature Dependence

There is a good linear correlation between C_q and temperature for most of the Al sites in the polymorphs, the exceptions being sillimanite Al_1 and Al_2 owing to the uneven structural changes and kyanite Al_2. Because there
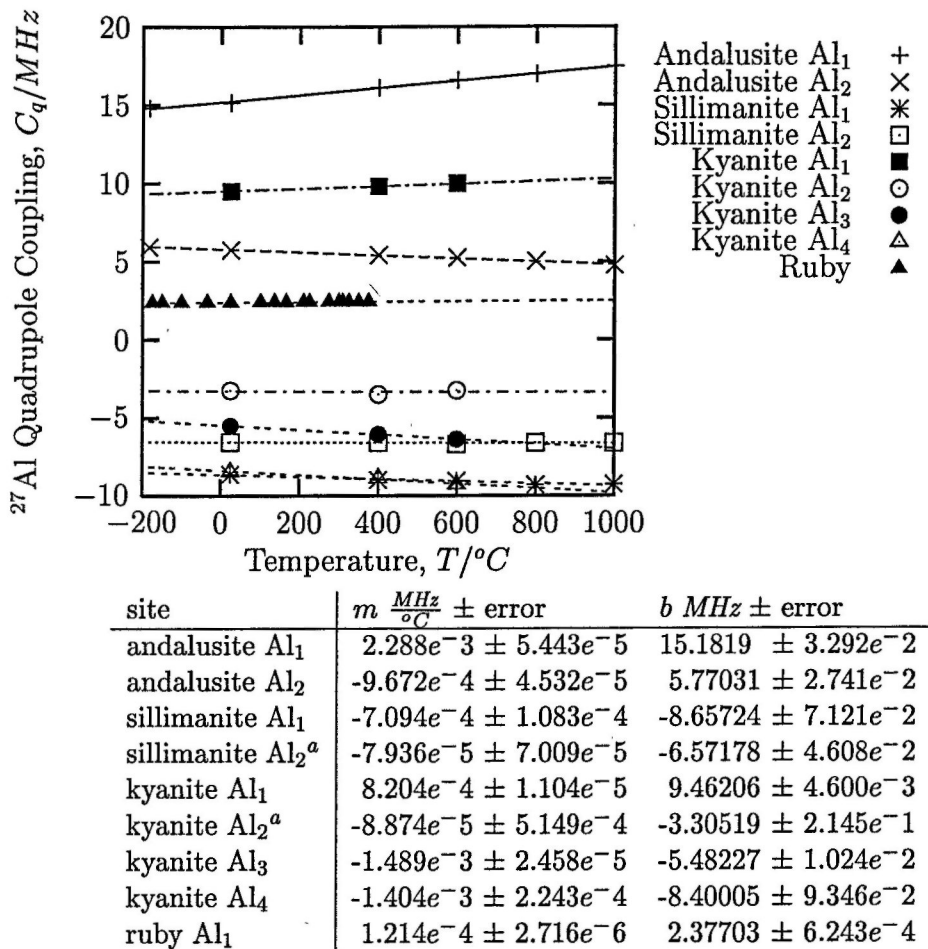
Figure 7.1: $C_q(T)$ fitting parameters. [a] The linear fitting parameters for sillimanite Al_2 and kyanite Al_2 are only shown to illustrate that the $C_q(T)$ relationship is not always linear for individual sites; their slope errors are unacceptably large.

site	$m \frac{MHz}{°C} \pm$ error	$b\ MHz \pm$ error
andalusite Al_1	$2.288e^-3 \pm 5.443e^-5$	$15.1819 \pm 3.292e^-2$
andalusite Al_2	$-9.672e^-4 \pm 4.532e^-5$	$5.77031 \pm 2.741e^-2$
sillimanite Al_1	$-7.094e^-4 \pm 1.083e^-4$	$-8.65724 \pm 7.121e^-2$
sillimanite Al_2[a]	$-7.936e^-5 \pm 7.009e^-5$	$-6.57178 \pm 4.608e^-2$
kyanite Al_1	$8.204e^-4 \pm 1.104e^-5$	$9.46206 \pm 4.600e^-3$
kyanite Al_2[a]	$-8.874e^-5 \pm 5.149e^-4$	$-3.30519 \pm 2.145e^-1$
kyanite Al_3	$-1.489e^-3 \pm 2.458e^-5$	$-5.48227 \pm 1.024e^-2$
kyanite Al_4	$-1.404e^-3 \pm 2.243e^-4$	$-8.40005 \pm 9.346e^-2$
ruby Al_1	$1.214e^-4 \pm 2.716e^-6$	$2.37703 \pm 6.243e^-4$

are kyanite structures at only three temperatures, any conclusions about correlations with temperature are not reliable.

In Figure 7.1, we show the temperature dependence of C_q for the 8 sites, as well as data for ruby. With the exception of the andalusite Al_2 site, the magnitude of C_q increases with temperature. There are rather different temperature dependencies for the different sites, though, ranging from $7.9 \times 10^{-5} MHz/°C$ for the four-coordinate site in sillimanite to $2.3 \times 10^{-3} MHz/°C$

for the six-coordinate site in andalusite. This spread in temperature dependencies makes it difficult to predict changes in EFG tensors without performing calculations at each temperature. With this in mind, we now turn to the suggested correlations between ^{27}Al NMR spectral parameters and geometric structure.

7.4.3 Polyhedral Distortion

Polyhedral distortion has been used to study the correlation between spectra and structure coordination polyhedra distortion in VPI-5 by Engelhardt and Veeman [195], in aluminosilicates by Ghose and Tsang [193] and in aluminate sodalites by Weller et al. [194]. Ghose et al. examined the relationship of $|C_q|$ and the coordination polyhedra formed by O around Al sites, concluding $|C_q|$ depends on bond lengths for octahedral sites and primarily on bond angle (and to a much lesser degree bond lengths) for tetrahedral sites. Robinson et al. use quadratic elongation as a measure of coordination polyhedra distortion [196] from which comes longitudinal, shear and total strain. Ghose and Tsang use Hamil's definitions of longitudinal strain ($|\alpha|$) and shear strain ($|\psi|$) [193]:

$$\text{longitudinal} \quad |\alpha| = \sum_i |\ln(l_i/l_0)| \tag{7.1}$$

$$\text{shear} \quad |\psi| = \sum_i |\tan(\theta_i - \theta_0)| \tag{7.2}$$

where l_0 is the ideal bond length, l_i is the actual bond length, θ_0 is the ideal bond angle, θ_i is the actual bond angle and $|\alpha| = 0$ and $|\psi| = 0$ mean no distortion, or an ideal polyhedra.

We use Ghose and Winter's values for polyhedral volume, longitudinal strain ($|\alpha|$) and shear strain ($|\psi|$) [193] in andalusite (α and ψ are reported only for the six-coordinate site), kyanite and sillimanite. For the Al$_2$ site in andalusite, we use Equations 1 and 2 to determine α and ψ. (cf. table 7.8)

Table 7.8: Andalusite Al_2 polyhedral strain. The longitudinal ($|\alpha|$), shear ($|\psi|$) and total polyhedral strain for andalusite Al_2, calculated using equations 7.2 and 7.1.

$T/^\circ C$	$|\alpha|$	$|\psi|$	total
-183	0.75	1.23	1.98
25	0.75	1.22	1.97
400	0.74	1.21	1.95
600	0.75	1.21	1.95
800	0.74	1.20	1.94
1000	0.73	1.19	1.93

We use the following as our definition of a perfect trigonal bipyramid: bond angles of 120 and 90 and the ratio of axial to equatorial bond lengths of 1.0, such that all O-O distances are equal.

In figures 7.2,7.3 and 7.4 we plot $|C_q|$ as a function of these three parameters. As can be seen, correlations do exist, but the slopes of the correlations are all different. This means one cannot simply apply information from one site to another. We do note the general trend that the magnitude of $|C_q|$ increases with increasing strain and polyhedral volume. The polyhedral volumes are distinct for each type of coordinated site, increasing from four to five to six coordinate. For each individual six coordinate site volume increases with temperature.

7.5 Conclusion

In this work, we calculate the EFG tenors and ^{27}Al NMR spectral parameters for the Al sites of the aluminosilicate polymorphs. We use these EFG tensors to match NMR signals from experiment to specific crystallographic sites. The four kyanite site assignments are new, the others confirm previous assignments. We also examine how the EFG tensors change with structure through calculations with crystal structures from different temperatures. We
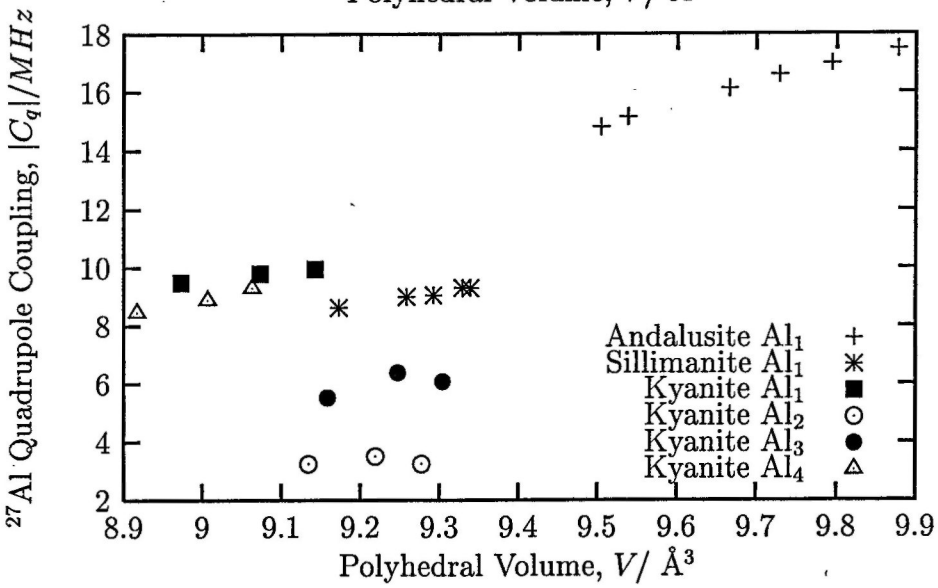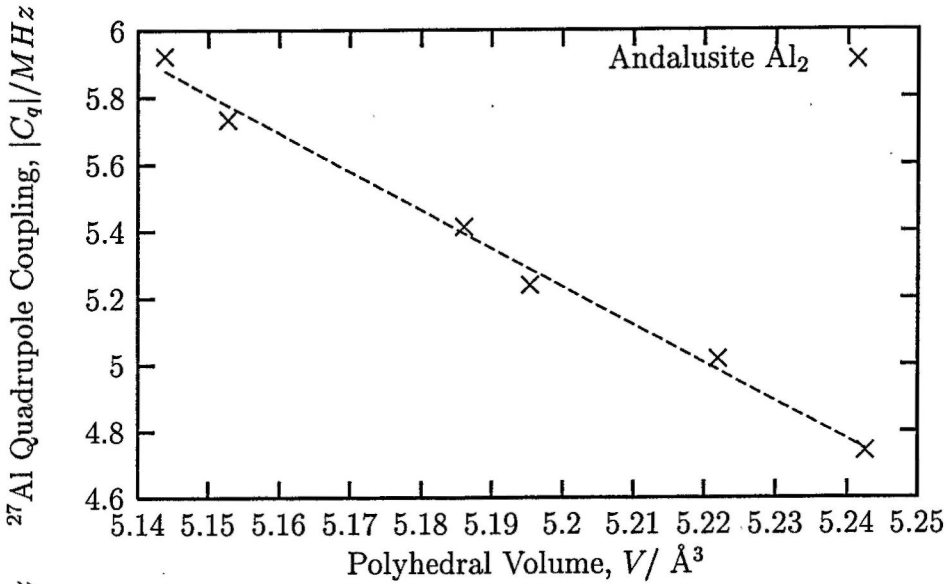
site	$m \frac{MHz}{Å^3} \pm$ error	$b\ MHz \pm$ error
andalusite Al_1	7.13568 $\pm$ 0.2569	-52.9188 $\pm$ 2.489
andalusite Al_2	-11.4577 $\pm$ 0.5087	64.8146 $\pm$ 2.640
sillimanite Al_1	4.07276 $\pm$ 0.3426	-28.7299 $\pm$ 3.179
kyanite Al_1	2.79825 $\pm$ 0.1651	-15.6182 $\pm$ 1.497
kyanite Al_2	0.217629 $\pm$ 2.125	1.33107 $\pm$ 19.57
kyanite Al_3	4.28583 $\pm$ 4.130	-33.5956 $\pm$ 38.15
kyanite Al_4	5.5971 $\pm$ 0.6642	-41.4698 $\pm$ 5.975

Figure 7.2: $|C_q|$(polyhedral volume)
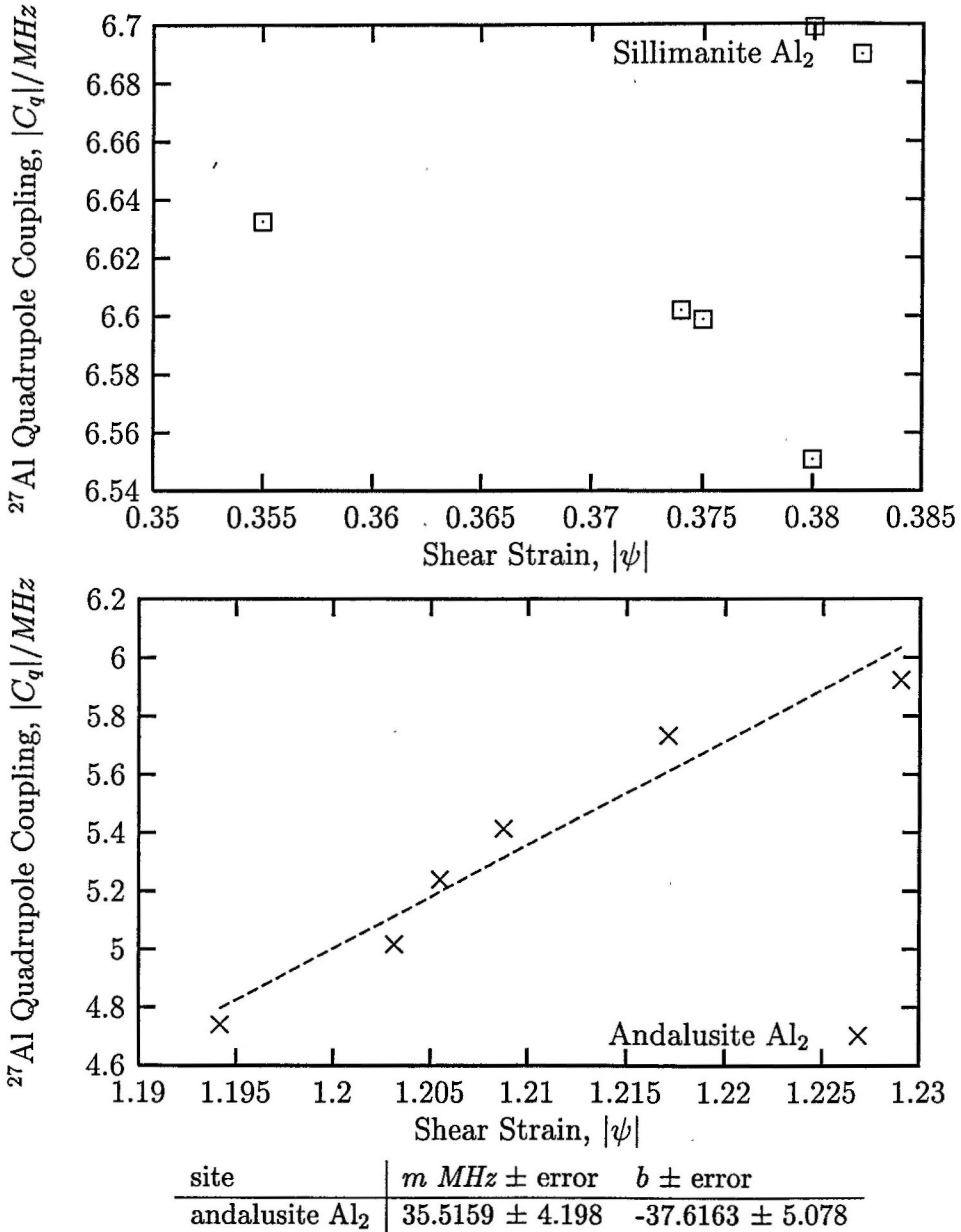
Figure 7.3: C_q(shear strain) The andalusite Al$_2$ site shows a very good correlation of C_q with shear strain, $|\psi|$, while the sillimanite Al$_2$ site shows none.

site	m MHz $\pm$ error	$b \pm$ error
andalusite Al$_2$	35.5159 $\pm$ 4.198	-37.6163 $\pm$ 5.078
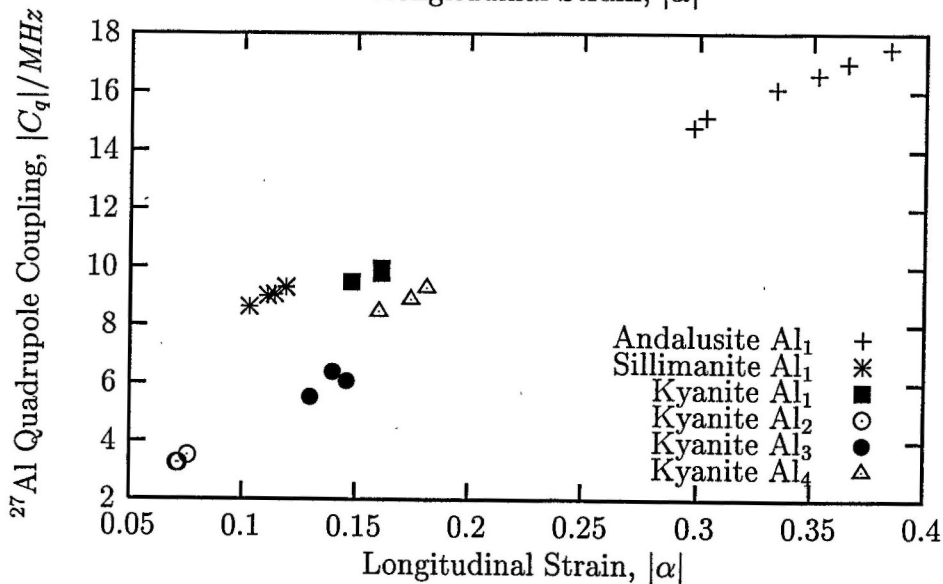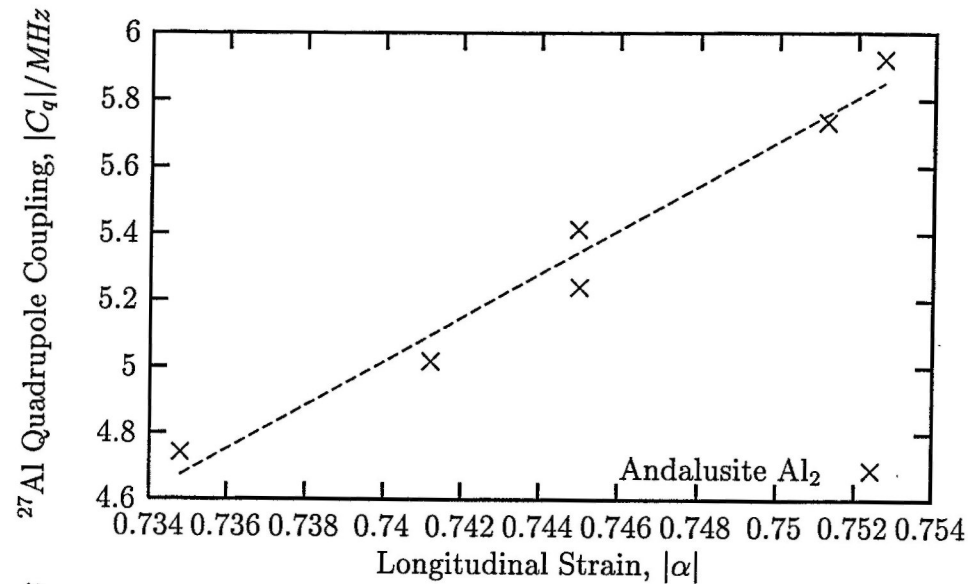
site	$m\ MHz \pm$ error	$b\ MHz \pm$ error
andalusite Al_1	30.1901 ± 1.124	5.94681 ± 0.3828
andalusite Al_2	65.8879 ± 6.114	-43.7413 ± 4.555
sillimanite Al_1	41.2815 ± 2.234	4.38497 ± 0.2532
kyanite Al_1	29.8288 ± 11.33	5.06917 ± 1.777
kyanite Al_2	56.5685 ± 11.08	-0.793991 ± 0.8091
kyanite Al_3	39.492 ± 36.53	0.514908 ± 5.071
kyanite Al_4	38.2361 ± 6.744	2.31603 ± 1.159

Figure 7.4: C_q(longitudinal strain)

examine the structural correlations of shear and longitudinal strain proposed for ^{27}Al NMR spectral parameters and found them to work well for single Al sites in a single polymorph at a number of temperatures, but the strain correlations do not work well across all sites. We add calculations for shear and longitudinal strain of the five coordinate Al site in andalusite, a distorted trigonal bipyrimidal shape. We note that as the crystals expand with increasing temperature, the magnitude of C_q tends to increase for six-coordinate Al sites. We also note that correlations postulated in previous work are valid, though there are quantitative differences between different sites that limit the utility of these approximations.

CHAPTER 8

BROMINATED AROMATICS: FLAME RETARDANTS

8.1 Introduction

The use of quantum chemical calculations to interpret nuclear magnetic resonance (NMR), nuclear quadrupole resonance (NQR), and gas-phase microwave spectra has a rich history. [156, 104, 159, 160, 97, 165, 65, 82, 75, 211, 119] Recent attention to NMR chemical shift calculations demonstrates a renewed interest for calculation of NMR properties. [212, 213, 214] Less attention has been focused on calculation of NQR transition frequencies, despite the widespread use of NQR spectroscopy in the study of materials containing ^2H, [215, 216, 63], ^{17}O, [217, 218] ^{27}Al [156], ^{14}N, [217], $^{63}Cu/^{65}Cu$, [219, 220] ^{93}Nb, [221], ^{35}Cl, [220, 222, 223], ^{209}Bi, [220], ^{23}Na, [221] and ^{81}Br [220, 224]. Of particular interest in this work are brominated aromatics, including flame retardants, recently studied by ^{81}Br NQR spectroscopy. [224] High-impact polystyrene (HIPS), used in manufacturing computer monitors, televisions, and business and electrical equipment, is made less flammable

by the inclusion of up to 30% by mass brominated aromatics. [4] ^{81}Br NQR spectra are used to measure flame retardant dispersion in HIPS. The major obstacle for ^{81}Br NQR is the exceedingly wide spectral range-over 40 *MHz* for brominated aromatics! For instance, sweeps of only 3 *MHz* can take 6 h, even with an automatically tuned NQR probe. There is clearly a need for a predictive method for ^{81}Br NQR transition frequencies.

Prior to this work, the only existing predictive model for ^{81}Br transition frequencies was based on Hammett σ values. [224, 225] These values relate the acidity of benzoic acid and substituted phenyl compounds to NQR transition frequencies, upon the premise that electronic effects of a substituent in one system are proportional to the electronic effects in another. While this model is useful for lightly meta- and para-substituted aromatics, it fails for heavily brominated flame retardants due to two issues related to ortho substituents: a lack of σ parameters for ortho substituents and steric effects not included in the Hammett model. [226]

In their solid-phase brominated aromatics are molecular crystals. While solid-phase calculations are possible by including the full-crystal structure, this limits one to systems with known structures. Few structures are available because heavily brominated aromatics as a class tend to be difficult to crystallize. In addition, computer memory requirements for solid-phase calculations are currently beyond our resources, due primarily to the large number of bromine atoms and the short hydrogen-bromine distances typically found in commercial flame retardants. The prediction of solid-phase NQR transition frequencies using gas-phase calculations is thus an area that needs exploration. Calculations of ^{81}Br NQR spectral parameters and transition frequencies via electric field gradient (EFG) calculations for small molecules now use larger, more complete basis sets and include electron corre-

lation, scalar-relativistic corrections, and vibrational and spin-orbit coupling effects. [227, 228, 229, 230, 231, 232, 233, 10] For small molecules, good correlations with experiment are being made using double-ζ basis sets including polarization. [144, 51, 234, 50] Gas-phase microwave and solid-phase NQR frequencies typically differ by less than 10% [119] (for instance, the value of $e^2 q_{zz} Q(^{81}\text{Br})/h$ (MHz) for gas phase is 8.5% higher than solid phase for methyl halides [235] and 6.9% higher for bromobenzene [236]). In addition, intermolecular interactions in the solid phase lead to splittings of transition frequencies that would be expected in more symmetric, gas-phase molecules. These splittings are small compared to the differences between different types of brominated aromatics. Thus, there are two aspects that require investigation: (1) can gas-phase calculations reproduce experimental trends and narrow the frequency search range for experimental work and (2) can gas-phase calculations be used to predict the splittings of frequencies seen in the solid-phase. In this work, we investigate (1) and leave (2) for future work.

In this paper, we report the first ab initio calculations of ^{81}Br NQR transition frequencies of brominated aromatics. These calculations are the first on large Br-containing molecules and the first on a commercially available flame retardant. We present calculations of ^{81}Br NQR transition frequencies for a series of simple brominated aromatics and predict absolute frequencies of Br in larger brominated aromatics by fitting calculations to experiments.

8.2 Method

First, ^{81}Br NQR frequencies were calculated for the nine simple brominated aromatics shown in figure 8.1. They were studied as isolated, gas-phase molecules. An initial geometry was generated using the SYBYL force field molecular mechanics routine in Spartan. [123] This was followed by a symmetry con-

strained, ab initio optimization in Cartesian coordinates using GAMESS [43] or Gaussian92 [41]. The restricted Hartree-Fock (RHF) and Becke's three-parameter Lee-Yang-Parr density functional theory hybrid method (B3LYP) methods were applied using the five basis set combinations shown in table 8.1 . Previous calculations of EFGs for small molecules have correlated well with experiment. These calculations typically used a rather low level of theory (RHF) and relatively small basis sets (double-ζ + polarization). While trends among molecules can be reproduced, absolute errors are about 10%; in the case of brominated aromatics, this would lead to errors of 20-30 *MHz*, which is too large to be of practical value. The are no EFG calculations of large bromine-containing molecules, so it is unknown if small basis sets and RHF can accurately reproduce the experimental trends. In light of these observations, we decided to undertake a systematic study of basis sets and levels of theory, within the bounds of our computer resources. Hence, we investigated both double- and triple-ζ basis sets (with and without polarization) and RHF and B3LYP levels of theory. More accurate ways of including correlation, such as CI, were beyond the ability of our computer resources. The smaller basis sets are advantageous because calculations are faster, but are potentially less accurate than larger basis sets. RHF calculations do not include correlation, while B3LYP calculations approximately include correlation. For both the double- and triple-ζ basis sets, polarization functions were added to bromine's basis set while the other atoms' basis sets remained unchanged. Mixed basis sets were chosen because the majority of the EFG is local [77, 163] and some basis sets are not available for Br. Sadlej's pVTZ [237, 238] basis set, which is available for Br, was not used due to convergence difficulties for these molecules. Geometry optimization and ^{81}Br frequency calculation were performed using the same basis set and level of theory. EFG

tensors were evaluated at Br in the optimized geometry. Then, EFG tensors were converted into the ^{81}Br $\nu(\pm\frac{1}{2} \to \pm\frac{3}{2})$ transition frequencies using the following relation: [224, 119]

$$\nu(\pm\frac{1}{2} \to \pm\frac{3}{2}) = (e^2 q_{zz} Q(^{81}\text{Br})/2h)(1 + (\eta^2)/3)^{\frac{1}{2}} \qquad (8.1)$$

Q(^{81}Br), the quadrupole moment for the ^{81}Br nucleus, is $2.76(4)10^{-29}m^2$, [65, 224] e is the charge of an electron, h is Plank's constant, q_{zz} is the largest component, and η is the asymmetry parameter of the diagonal EFG tensor. It is defined as $\eta = (|q_{yy}| - |q_{xx}|)/|q_{zz}|$. We follow the convention of ordering the eigenvalues of the traceless EFG tensor by absolute value such that $|q_{zz}| \geq |q_{yy}| \geq |q_{xx}|$. Conversion of q_{zz} from atomic units (and GAMESS sign convention) to MHz used the relation:[224]

$$e^2 q_{zz} Q(^{81}\text{Br})/h)(MHz) = q_{zz}(\text{atmic units}) \times (-64.85 MHz/au) \qquad (8.2)$$

The predictive ability of gas-phase calculations was investigated by using a linear fit of experimental, solid-phase frequencies to the calculated, gas-phase frequencies for the nine simple brominated aromatic molecules shown in figure 8.1. The fits were used to predict the frequencies of 1-(2,3,4,5,6-pentabromophenoxy)-2,3,4,5,6-pentabromobenzene (Saytex 102) and 1-bromo-4-(4-bromophenoxy)benzene. These are molecules 10 and 12 in figure 8.2, both recently studied. 10 is sold commercially as a flame retardant and 12 is used as a model for flame retardant dispersal.24 CPU time considerations prevented calculations on 10 itself, forcing us to use a truncated version, 11. For 12, both the entire molecule and a truncated version (13 in figure 8.2) were studied. The comparison of the results of 12 and 13 was used to assess the relevance of the results from 11.
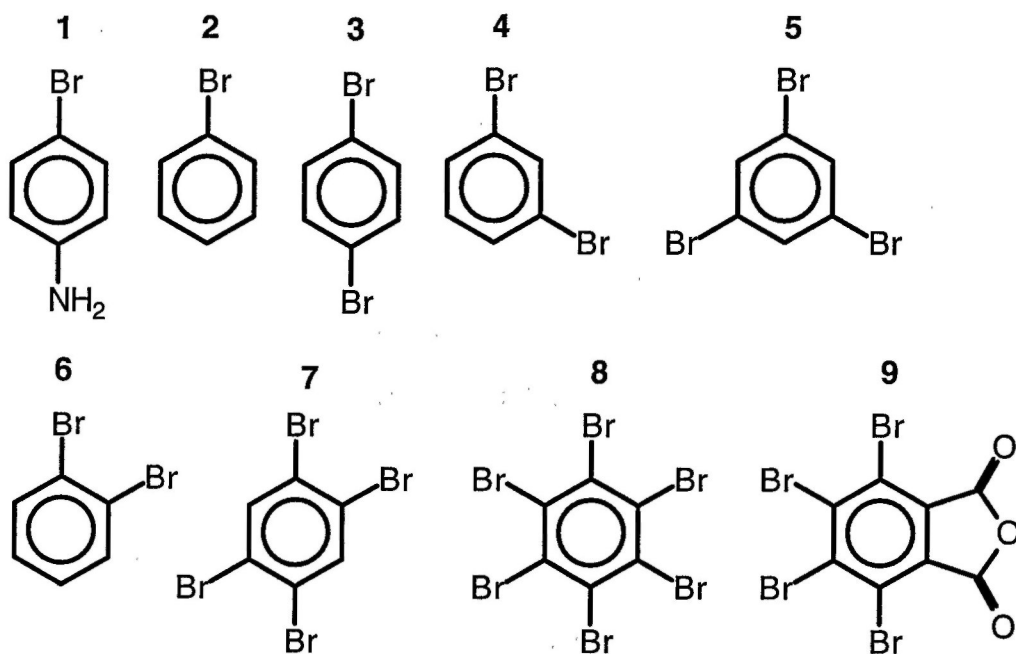
Figure 8.1: Simple brominated aromatics: 1) 4-bromoanaline; 2) bromobenzene; 3) 1,4-dibromobenzene; 4) 1,3-dibromobenzene; 5) 1,3,5-tribromobenzene; 6) 1,2-dibromobenzene; 7) 1,2,4,5-tetrabromobenzene; 8) hexabromobenzene; and 9) 3,4,5,6-tetrabromophthalic anhydride (flame retardant, tradename: Saytex RB-49).

basis set level	Br notation	ref	source	H,C,N,O notation	ref	source
double zeta	DZV	[239]	[240]	6-31G	[241]	[240]
	DZV(d)	[239]	[240]	6-31G	[241]	[240]
	DZV(df)	[239]	[240]	6-31G	[241]	[240]
triple zeta	TZV	[239, 242]	[134]	TZV	[243]	[240]
	TZV(df)	[239, 242]	[134]	TZV	[243]	[240]

Table 8.1: Basis sets. The polarization groups are explicitly shown in paren-thesis. Ref. refers to the original work for a basis set while Source refers to where the explicit form was obtained.

8.3 Results and Discussion

The calculated and measured [81]Br NQR transition frequencies of all mole-cules are listed in table 8.2 and table 8.3 . As necessary, the experimental frequencies are averaged over multiple lattice sites. For example, the av-erage 231.228 *MHz* is reported for 1,3,5-tribromobenzene which has three
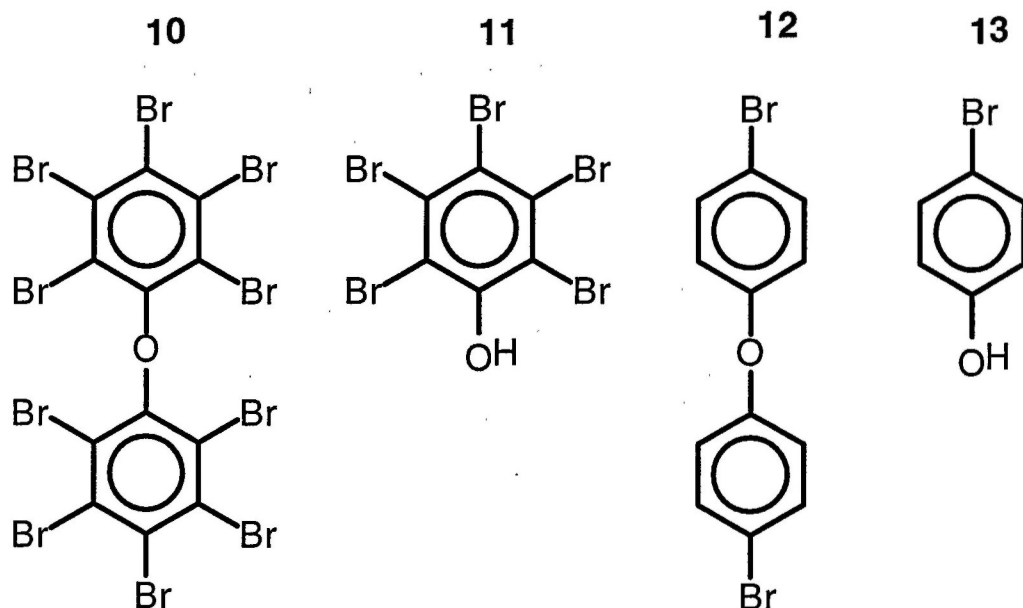
Figure 8.2: Flame retardant and models: 10) 1-(2,3,4,5,6-pentabromophenoxy)-2,3,4,5,6-pentabromobenzene (flame retardant, tradename: Saytex 102); 11) truncated version of 10; 12) 1-bromo-4-(4-bromophenoxy)benzene; 13) truncated version of 12.

Table 8.2: Experimentally observed and calculated ^{81}Br NQR transition frequencies (in *MHz*) for simple brominated aromatics. [a] Average of multiple transitions. [b] Average of two observed transitions assigned to this chemical site. [c] here 9′ refers to crystallographic sites Br-3 and Br-6 and 9″ to Br-4 and Br-5

molecule	expt.	ref.	basis set				
			DZV	DZV(d)	DZV(df)	TZV	TZV(df)
			RHF				
1	221.862	[244]	222.937	217.862	232.067	256.852	251.287
2	220.890	[245]	225.119	219.235	233.595	259.583	253.224
3	226.490	[225]	230.394	223.715	237.694	264.379	257.096
4	231.489[a]	[246]	231.638	224.776	238.683	265.583	258.271
5	231.228[a]	[224]	237.424	229.757	243.219	271.005	262.879
6	236.019[a]	[247]	239.863	232.418	246.178	275.381	266.562
7	239.701	[224]	247.945	239.573	252.685	283.083	272.954
8	255.196[a]	[247]	263.089	253.671	266.847	301.926	289.030
9′ [c]	253.080[b]	[224]	265.822	255.655	267.947	299.880	290.441
9″ [c]	254.293[b]	[224]	271.896	262.168	273.110	304.421	294.799
			B3LYP				
1	221.862	[244]	228.766	224.001	236.428	260.779	255.863
2	220.890	[245]	230.183	224.818	237.276	262.464	255.176
3	226.490	[225]	234.546	228.632	240.961	266.464	258.456
4	231.489[a]	[246]	235.400	229.385	241.605	267.370	259.275
5	231.228[a]	[224]	240.037	233.504	245.341	271.832	263.042
6	236.019[a]	[247]	244.639	236.465	247.930	277.718	265.878
7	239.701	[224]	248.502	241.201	253.202	281.866	270.917
8	255.196[a]	[247]	256.440	252.086	264.646	303.526	283.825
9′ [c]	253.080[b]	[224]	263.653	253.750	263.517	296.701	282.125
9″ [c]	254.293[b]	[224]	268.160	258.644	267.940	299.152	285.280

Table 8.3: Experimentally observed and calculated ^{81}Br NQR transition frequencies (in *MHz*) for flame retardant and models ^{a} average of multiple transitions.

molecule	expt.	ref.	basis set				
			DZV	DZV(d)	DZV(df)	TZV	TZV(df)
			RHF				
12	228.117^a	[224]	229.123	222.862	236.824	262.831	256.129
13		[224]	227.383	221.449	235.478	261.573	255.135
11	254.148^a	[224]	260.756	251.946	264.442	297.724	285.722
			B3LYP				
12	228.117^a	[224]	233.866	228.158	240.309	265.637	257.933
13		[224]	232.315	226.798	239.003	264.630	257.085
11	254.148^a	[224]	258.120	250.557	262.346	293.228	280.677

crystallographically inequivalent bromine sites with observed transitions at 230.407, 231.533, and 231.745 *MHz*. [224] Plots of experimental frequency versus calculated frequency for all basis sets are shown for RHF in figure 8.3 and B3LYP in figure 8.4. Differences in frequencies between unoptimized and ab initio optimized structures varied nonuniformly between 5 and 10 *MHz*. Thus, we deemed optimization important and report only the frequencies for the ab initio optimized structures. All basis sets and levels of theory adequately reproduce the experimental trends. Qualitatively, triple-ζ basis sets give frequencies about 10% higher than double-ζ basis sets and the polarization functions appear to affect frequencies only quantitatively. The gas-phase frequency for 1-bromobenzene is 240.034 *MHz*;41 our calculations show that double-ζ basis sets underestimate this value by about 5-10% and the triple-ζ basis sets overestimate this value by 5-10%. This result, com-

Table 8.4: Fitting parameters, rms residuals, and maximum errors for calculated and fitted [81]Br NQR transition frequencies for simple brominated aromatics

	basis set				
	DZV	DZV(d)	DZV(df)	TZV	TZV(df)
RHF					
fitting parameters					
correlation coeff	0.984	0.983	0.986	0.991	0.987
slope	1.326	1.202	1.136	1.365	1.225
intercept/MHz	-70.575	-49.040	-20.158	-45.335	-20.616
rms residuals/MHz					
raw calculation	8.307	3.970	12.527	41.497	32.844
linear fit	2.271	2.366	2.106	1.643	2.026
max error (calculated - experimental)/MHz					
raw calculation	17.603	7.876	18.817	50.129	40.507
linear fit	4.069	4.599	3.769	-3.714	-3.760
B3LYP					
fitting parameters					
correlation coeff	0.969	0.984	0.989	0.991	0.990
slope	1.022	0.944	0.887	1.198	0.892
intercept/MHz	2.763	14.438	39.664	-5.059	56.574
rms residuals/MHz					
raw calculation	9.124	2.563	13.039	41.886	31.027
linear fit	3.377	2.268	1.836	1.727	1.747
max error (calculated - experimental)/MHz					
raw calculation	13.868	4.352	16.386	48.330	34.286
linear fit	-7.011	4.332	-3.799	-3.998	-4.228

Table 8.5: Rms residuals and maximum errors for calculated and predicted ^{81}Br NQR transition frequencies for flame retardant and models

| | basis set | | | | |
	DZV	DZV(d)	DZV(df)	TZV	TZV(df)
			RHF		
			rms residuals/MHz		
raw calculation	3.882	5.064	8.869	37.520	28.934
linear fit	3.306	3.025	3.043	2.846	3.124
			max error (calculated - experimental)/MHz		
raw calculation	6.608	-6.668	10.294	43.576	31.574
linear fit	-4.191	-3.761	-3.713	-3.280	-4.003
			B3LYP		
			rms residuals/MHz		
raw calculation	4.706	2.209	10.557	37.719	28.472
linear fit	3.426	3.175	2.847	3.580	2.881
			max error (calculated - experimental)/MHz		
raw calculation	5.749	-3.591	12.192	39.080	29.816
linear fit	-4.319	-4.088	-3.361	-5.064	-3.311
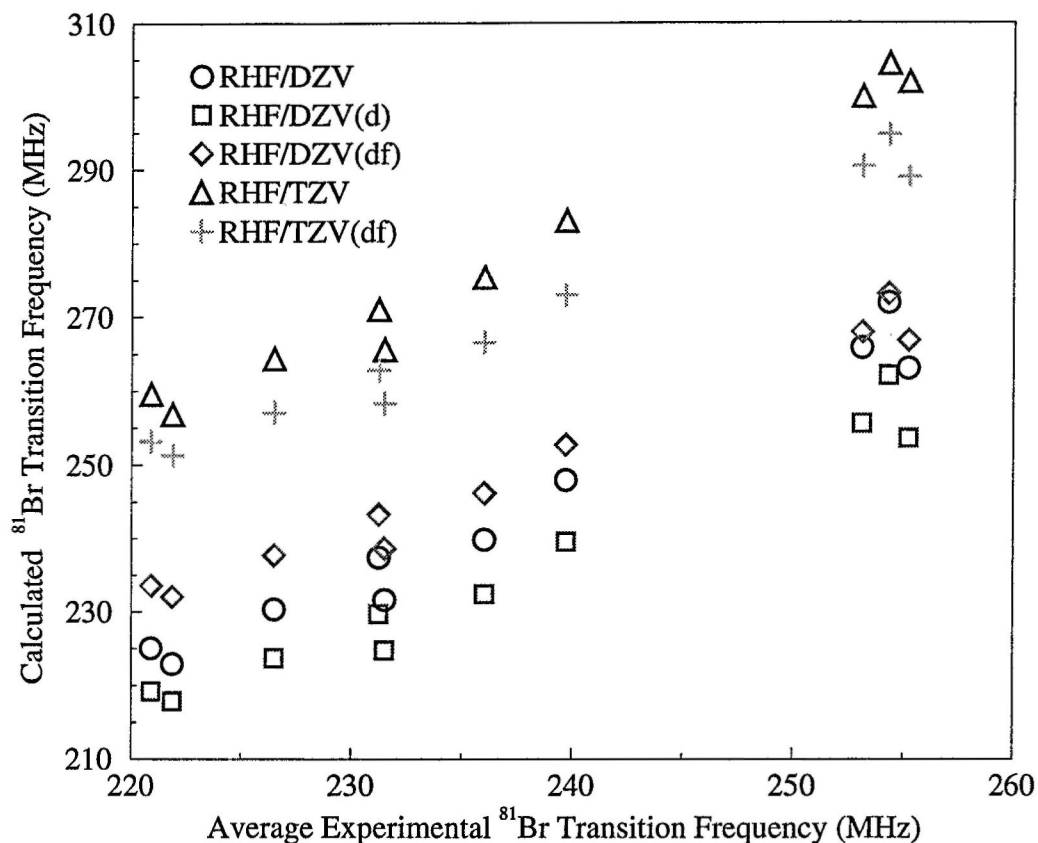
Figure 8.3: ^{81}Br NQR transition frequencies from RHF calculations plotted against values from experiment.

bined with the good reproduction of the trends among different brominated aromatics, suggests that both double and triple-ζ basis sets are adequate for brominated aromatics.

As a quantitative measure of the agreement between calculation and experiment, we calculated the rms errors and the maximum error made for each basis set and level of calculation. These are shown in table 8.4 . The double-ζ basis sets have rms errors around 10 MHz, while the triple-ζ basis sets have rms errors of about 30-40 MHz. The maximum errors have a similar pattern.
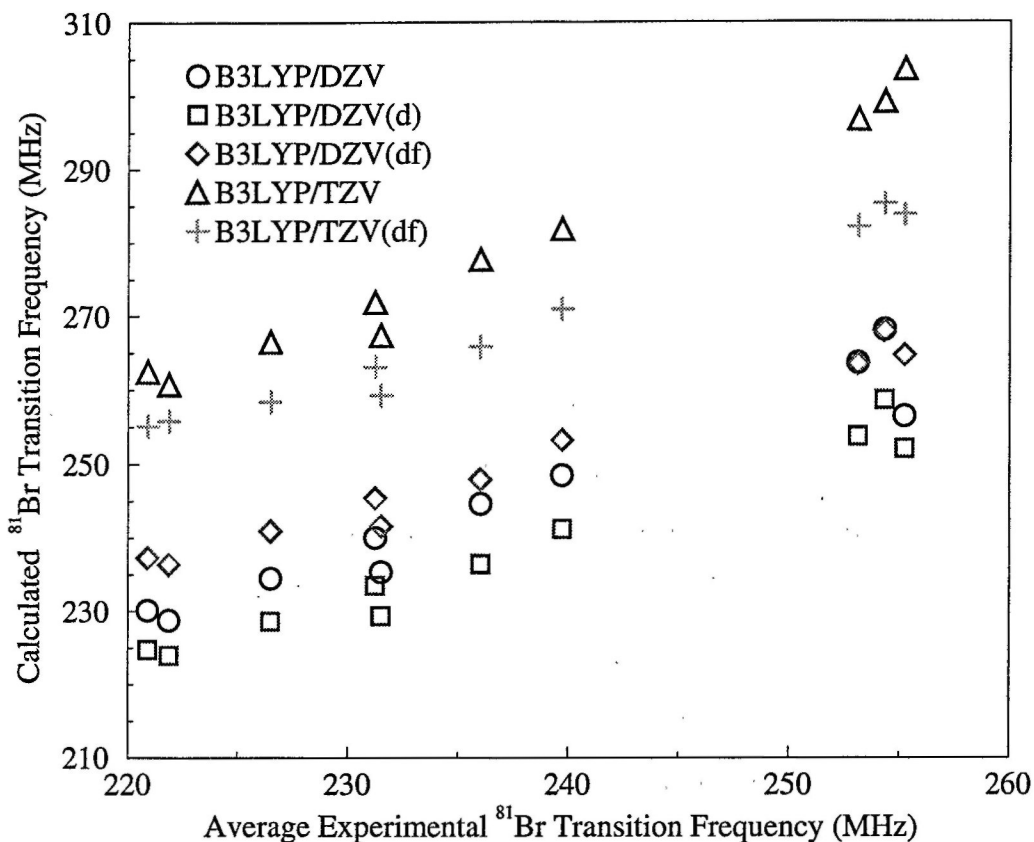
Figure 8.4: ^{81}Br NQR transition frequencies from B3LYP calculations plotted against values from experiment.

The trends among the brominated aromatics are well represented by gasphase calculations, but absolute differences between calculation and experiment remain. We used a linear fit of experiment versus calculation to see if calculations, combined with a fit, could be used to accurately predict NQR transition frequencies. The values of our fitting parameters (slope and intercept) as well as the rms and maximum errors are given in table 8.4. The fits give rms errors less than about 5 *MHz*. All basis sets, with the possible exception of DZ, give maximum errors on the order of 5 *MHz* using either RHF or B3LYP. The correlation coefficient shows the frequencies calculated

with the larger basis sets to be very slightly more correlated with those from experiment.

We now turn to the predictive ability of the calculations. Using a linear fit, the [81]Br NQR transition frequencies were predicted for a flame retardant and a model for flame retardant dispersal, molecules 10 and 12 in figure 8.2. Having two aromatic rings, both are significantly bigger than most of the simple brominated aromatics studied above and shown in figure 8.1. 12 is small enough to perform a geometry optimization in a reasonable amount of CPU time, but 10 is too large to make such an exercise practical. As a result, truncated versions of 10 and 12 (11 and 13, respectively) were also studied. A comparison of the results from 12 and 13 was made to assess the impact of truncation. Since the EFG is a local property, it is not expected that there is a large inter-ring effect in either molecule (neither is a planar molecule [224]). Therefore, we truncated both molecules by the substitution of an -OH group for the duplicate ring. The frequencies for these three calculations are shown in table 8.3. 13 proved to be a reasonable representation of 12, differing in calculated transition frequencies by less than 2 *MHz*. As can be seen from the rms and maximum errors reported in table 8.5, the agreement with experiment using the linear fit is quite good. For RHF and B3LYP with all basis sets agreement is within about 5 *MHz*.

Several comments can be made about the different basis sets and levels of theory. Neither the DZV or TZV basis sets give better than 5-10% absolute accuracy when compared to the gas-phase experimental result for 1-bromobenzene, indicating that larger basis sets are needed to obtain convergence on an absolute scale. However, both DZV and TZV, when used with a linear fit, accurately reproduce the experimental trend, indicating that both basis sets are adequate for estimating experimental frequencies.

Overall, using a linear fit and RHF with the TZV basis set yields the most accurate results. The linear fit with RHF and the DZV basis set is nearly as accurate and can be used if computational resources are limited. Without the linear fit, using B3LYP with the DZV(d) basis set is also fairly accurate, this is probably due to a fortuitous cancellation of errors. When using a linear fit, polarization and correlation (using B3LYP) do not seem to improve the agreement between experiment and calculation. It is unclear whether this is due to the similarity between molecules studied here or to some more fundamental reason.

8.4 Conclusion

We calculated the EFG tensors at bromine sites in a series of simple brominated aromatics. RHF and B3LYP calculations using a double- or triple-ζ basis set and the linear fit prove capable of 5 *MHz* accuracy. The predictive capability of the calculations is demonstrated by comparing a prediction with known experimental frequencies for a commercial flame retardant and a model for flame retardant dispersal. Calculations are shown to be a useful tool for experimentalists looking for an NQR signal over a large range of frequencies. In the present case, the search range has been narrowed from 40 to 5 *MHz*, allowing a significant reduction in the time required to acquire data.

Three items prevent closer agreement of calculations and experiment: (1) differences between solid- and gas-phase systems, (2) deficiencies in the description of the electronic system such as omission of vibrational, spin-orbit, and scalar-relativistic effects, and (3) the value of the quadrupole moment for ^{81}Br. [248] Including the intermolecular effects that are present in the solid brominated aromatics is important, as is demonstrated by the splitting

of transition frequencies seen in the solids. A simple method of including such effects, developed in a previous paper, [224] was not successful with the molecules studied in this work. Future work will investigate more systematic methods of including intermolecular interactions, such as representing other molecules in the crystal with point charges. Calculations that include scalar relativistic and spin-orbit effects were recently performed for HBr. [227] Frequencies calculated from that work (using the literature value of the Br quadrupole moment [65]) still differ with those from gas-phase experimental frequencies [249] by as much as 11%. The errors introduced through items 2 and 3 remain unresolved for small diatomic molecules and more exact methods remain computationally intractable for the large molecules we studied. However, the agreement seen here between predicted and observed frequencies demonstrates that calculations combined with fits can provide an effective procedure predicting experimental NQR frequencies.

CHAPTER 9

NITRO AROMATICS: EXPLOSIVES

9.1 Introduction

Compounds containing quadrupolar nuclei — such as ^{14}N found in explosives — produce a characteristic radio signal as nuclei relax after a low-intensity radio frequency pulse has first aligned their spins. Companies such as Quantum Magnetics [6], use this characteristic signal as a means of explosives detection in aviation security devices and other applications such as land mine detection systems and non-destructive test equipment. The difficulty lies in knowing what characteristic signal a particular compound will produce ahead of time. Calculations can help narrow the range which experimentalists have to search in order to find this signal.

Some theoretical studies of ^{14}N EFGs exist, though few include nitro (NO_2) groups. There are studies of EFGs in N containing compounds such as purines, pyrimidines, amides, thioamides, azoles, and azines [89, 90, 91, 92]. There are a few theoretical studies on compounds similar to tetryl. Pati et al. conducted similar theoretical studies on heroine [250], cocaine [251]. HMX [252] and RDX [63]. After those studies were conducted a revised value of the quadrupole coupling constant for the ^{14}N nucleus has

become available [122]. We have recently conducted theoretical studies on brominated aromatics [190], which share a common theme of the nucleus of interest being in a functional group immediately attached to a single aromatic ring.

We compare our calculated EFGs to those determined by NQR where possible. Values are available for TNB, TNX and TNT ^{14}N NQR from Marino [253]. The only hyperfine interaction data we are aware of for tetryl is a paramagnetic resonance study [254]. Measurement of the RDX ^{14}N NQR coupling constants and temperature dependence also exists [255].

9.2   Method

We report predictions for the ^{14}N NQR transition frequencies (ν_+, ν_- and ν_d) of tetryl. We perform *ab initio* calculations of tetryl and several similar compounds for which experimental data is available (cf. figure 9.1 and table 9.2).

We test several approaches for obtaining a structure for calculations:

1. perform a single point calculation on single molecules extracted from crystal structures for TNX [256], RDX [257], TNB [258], TNT (orthorhombic and monoclinic forms)[259] and tetryl [260];

2. build highly symmetric structures and then perform a geometry optimization calculation;

3. extract a single molecule from the crystal structure and perform a geometry optimization calculation.

We use two methods of calculation, RHF and B3LYP. We examine five basis sets: 6-311G, cc-pVDZ, cc-pCVDZ, cc-pVTZ and cc-pCVTZ. Because B3LYP and full optimization of single molecules from the crystal structure

Table 9.1: Experimental nitrogen-14 spectral data from $77K$. TNT, TNB, TNX are from table 1 in Reference [253]. RDX is from Table I in Reference [255]. q_{zz} was calculated via $C_q(MHz)/-4.80339(MHz/au)$. Column 1 'site' numbers and designations refer to the experiment paper. Columns 8 and 9 'assignment' refers to assignments to crystal and optimized structures based on this work. q_{zz} is in atomic units. C_q, ν_+, ν_- and ν_d are in megahertz. [a] Site assignments from reference [253]. [b] Site assignments from reference [63].

site	q_{zz}	C_q	η	ν_-	ν_+	ν_d	assign. crys.	opt.
trinitrotoluene monoclinic (TNT) NQR 77K								
1 (oAI)	-0.2306	1.1077	0.1396	0.8694	0.7921	0.0773	9	9,8
2 (oAII)	-0.2356	1.1315	0.1654	0.8954	0.8018	0.0936		9,8
3 (oBII)	-0.2255	1.0831	0.1649	0.8570	0.7677	0.0893		9,8
4 (oBI)	-0.2280	1.0953	0.1978	0.8756	0.7673	0.1083	7	9,8
5 (pI)	-0.2209	1.0610	0.2490	0.8618	0.7297	0.1321	8	12
6 (pII)	-0.2246	1.0788	0.2929	0.8881	0.7301	0.1580		12
trinitrotoluene orthorhombic (TNT) NQR 77K								
7 (oAI)	-0.2304	1.1068	0.1362	0.8678	0.7924	0.0754	8	9,8
8 (oAII)	-0.2361	1.1341	0.1670	0.8979	0.8032	0.0947		9,8
9 (oBII)	-0.2258	1.0847	0.1661	0.8586	0.7685	0.0901		9,8
10 (oBI)	-0.2279	1.0948	0.1995	0.8757	0.7665	0.1092	7	9,8
11 (pI)	-0.2206	1.0598	0.2546	0.8623	0.7274	0.1349	9	12
12 (pII)	-0.2246	1.0787	0.2839	0.8856	0.7325	0.1531		12
trinitrobenzene (TNB) NQR 77K								
13	-0.2384	1.1449	0.3518	0.9594	0.7580	0.2014	(10),11	1,2,3
14	-0.2373	1.1400	0.3593	0.9574	0.7526	0.2048	(11),10	1,2,3
15	-0.2312	1.1107	0.3545	0.9315	0.7346	0.1969	12	1,2,3
16	-0.2254	1.0828	0.3506	0.9070	0.7172	0.1898		1,2,3
17	-0.2155	1.0351	0.4162	0.8840	0.6686	0.2154		1,2,3
18	-0.2132	1.0240	0.2500	0.8320	0.7040	0.1280		1,2,3
trinitro-m-xylene (TNX) NQR 77K								
19	-0.2194	1.0540	0.1195	0.8220	0.7590	0.0630	11[a]	12[a]
20	-0.2284	1.0970	0.2316	0.8860	0.7592	0.1268	10,18[a]	8,9 [a]
RDX NQR 77K								
2	-1.2033	5.780	0.6374	5.2560	3.4140	1.8421	4[b]	4,5,6
1	-1.2256	5.887	0.6139	5.3188	3.5117	1.8070	5[b]	4,5,6
3	-1.1815	5.675	0.6076	5.1183	3.3942	1.7241	6[b]	4,5,6
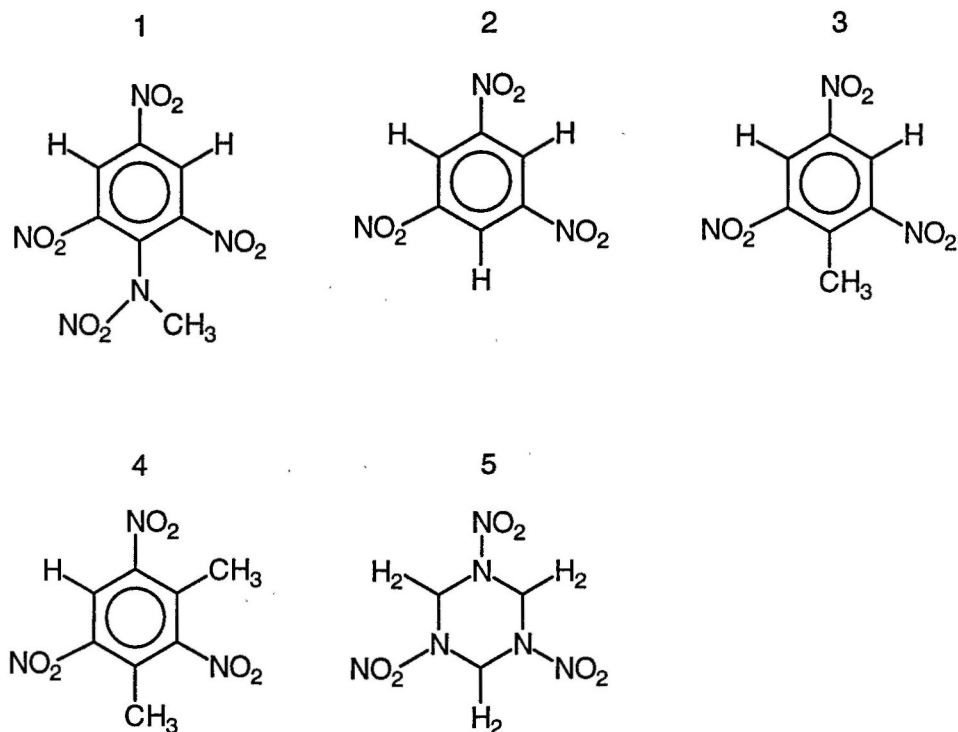
Figure 9.1: 1) tetryl (N-methyl-N-2,4,6-tetranitroaniline, $C_7H_5N_5O_8$); 2) TNB (trinitrobenzene, $C_6H_3N_3O_6$); 3) TNT (trinitrotoluene, $C_7H_5N_3O_6$ orthorhombic and monoclinic); 4) TNX (trinitro-m-Xylene, $C_8H_7N_3O_6$) and 5) RDX (hexahydro-1,3,5-trinitro-s-triazine, $C_3H_6N_6O_6$). Note these are idealized two-dimensional representations, the nitro (NO_2) groups are not actually planar and the RDX conformation is chair-like.

Table 9.2: Number of electrons, e^-, and atoms for tetryl and mimics. [a]Symmetry point group found by full optimization of single molecule from crystal structure at B3LYP/cc-pVDZ using Gaussian and symmetrization with default tolerance 0.04 in Jaguar.

molecule	e^-	atoms	point group[a]
rdx	114	21	C_s
tetryl	146	25	C_1
tnb	108	18	D_{3h}
tnt	116	21	C_s
tnx	124	24	C_2

Table 9.3: ^{14}N electric field gradients, q_{zz}, in atomic units in Ammonia from a calculation by Palmer [261].

basis	method	q_{zz}/au
DZ	SCF	1.3283
DZ	CI	1.2049
TZV	SCF	1.2595
TZV	CI	1.2007
TZVP	SCF	1.0195
TZVP	CI	0.9825

requires much more CPU time than single point calculations we only examine the cc-pVDZ.

9.3 Results and Discussion

9.3.1 Preliminary Calculations on NH_3

Our theoretical approach has been successful for ^{27}Al in aluminosilicates and ^{81}Br in bromobenzenes. To verify the validity of our approach for ^{14}N a series of calculations on ammonia NH_3 with C_3V symmetry was performed. Comparison of tables 9.3 and 9.4 shows that our approach compares quite favorably to a much earlier study of EFGs in ammonia by Palmer [261]. Specifically, using a recently developed, large basis set with tight core functions and polarization at the triple zeta level (cc-pCVTZ) with only RHF produces a value for q_{zz} as good as Palmer's best configuration interaction (CI) calculation. In addition, using our smallest basis set and B3LYP we also obtain a value as good as Palmer's CI/TZVP. This validates our approach for small N compounds, leaving the study of tetryl and mimics to test its validity for N in -NO_2 groups.

Table 9.4: ^{14}N electric field gradients, q_{zz}, in atomic units from RHF and B3LYP calculations on optimized C_{3v} NH$_3$.

	basis set			
method	cc-pVDZ	cc-pCVDZ	cc-pVTZ	cc-pCVTZ
RHF	1.0101	1.0328	1.0056	0.9841
B3LYP	0.9894	1.0279	1.0600	1.0544

9.3.2 Predictions of Tetryl Frequencies

Because *ab initio* calculations tend to be better at reproducing trends than absolute values, we also examine a fit of our calculated values for the quadrupole coupling constant, C_q, to experimental values. This line of best fit is subsequently used to adjust the raw calculated values of C_q for tetryl. These adjusted values for C_q and the calculated value of the electric field gradient asymmetry, η, are then used to calculate the transition frequencies. Predicted NQR transition frequencies for tetryl using B3LYP/cc-pVDZ with single point calculations on molecules from the crystal structures are reported in table 9.5. Predictions are from linear fits of the C_q values from experiments and calculations. Calculations are of single molecules from crystal structures and use the B3LYP method with the cc-pVDZ basis set. Predictions of $C_{q,\text{expt}}$ for sites N$_8$, N$_9$, N$_{10}$ and N$_{12}$ used experimental values from TNX, TNB, TNT-o and TNT-m. They were made from

$$C_{q,\text{expt}} = (0.286148 \pm 0.213) \times C_{q,\text{calc}} + (1.35393 \pm 0.1911) \qquad (9.1)$$

Predictions of $C_{q,\text{expt}}$ for the site N$_{11}$ were made from

$$C_{q,\text{expt}} = (-0.897049 \pm 0.008894) \times C_{q,\text{calc}} + (0.29386 \pm 0.02615) \quad (9.2)$$

and additionally included RDX in the fitting procedure. Refer to the section conversion of EFG to NQR frequencies in the methodology chapter for calcu-

Table 9.5: Predictions for tetryl ^{14}N NQR transition frequencies. C_q, ν_+, ν_- and ν_d are in megahertz. Subscripts on N refer to atom number from calculation input file.

	N_8	N_9	N_{10}	N_{11}	N_{12}
raw values from B3LYP/cc-pVDZ calculation					
C_q	-0.6660	-0.8021	-0.7024	-6.8153	0.6279
η	0.6802	0.6167	0.5694	0.3431	0.5324
predicted C_q					
C_q	1.1634	1.1244	1.1529	6.4075	1.5336
predicted frequencies					
ν_+	0.6747	0.6700	0.7006	4.2560	0.9461
ν_-	1.0703	1.0167	1.0288	5.3552	1.3543
ν_d	0.3957	0.3467	0.3282	1.0992	0.4082

lating ν_+, ν_- and ν_d from C_q and η. The notation we designate atomic sites in tetryl with is mapped to the crystal structure notation in the appendix.

Results from single point calculations on the crystal structures are shown in tables 9.6–9.14. Results from optimized calculations on the symmetric structures are shown in tables 9.17–9.21. Results from fully optimized crystal structures (using C_1 symmetry) are shown in table 9.16. Unlike our other studies, focusing on ^{27}Al or ^{81}Br NMR spectral parameters, a significant difference is seen between B3LYP and RHF. In those studies there are small changes in C_q magnitude (usually a decrease) and η is nearly the same from both methods. For EFG calculations of N in NO$_2$ groups attached to rings this is not the case; for those there is a marked change in C_q magnitude and a change in η. It is worth noting that the RHF calculations yield an η much closer to that of experiment than B3LYP. Another point is that the calculations using crystal structures are better able to reproduce the absolute values and relative trends from experiment. We suspect this is due to unrealistic constraints of symmetry in the symmetry optimized versions;

Table 9.6: ^{14}N quadrupole coupling constants, C_q/MHz, from RHF calculations on single molecules from crystal structure data.

| molecule | site | basis set | | | | |
		6-311G	cc-pVDZ	cc-pCVDZ	cc-pVTZ	cc-pCVTZ
RDX	N_4	-7.7480	-6.6789	-6.7753	-6.6843	-6.6326
RDX	N_5	-7.9813	-6.8360	-6.9494	-6.9783	-6.8965
RDX	N_6	-8.0246	-6.8740	-6.9875	-7.0186	-6.9352
RDX	N_7	1.9089	2.7342	2.7139	3.0825	2.8499
RDX	N_8	1.8211	2.6462	2.6306	2.9999	2.7761
RDX	N_9	1.8204	2.6407	2.6255	2.9934	2.7705
tetryl	N_8	2.0201	2.8036	2.7999	3.2268	2.9876
tetryl	N_9	2.1497	2.9295	2.9203	3.3370	3.0954
tetryl	N_{10}	1.9741	2.7994	2.7860	3.1821	2.9541
tetryl	N_{11}	-8.6983	-7.6068	-7.7051	-7.6410	-7.5532
tetryl	N_{12}	1.8691	2.6840	2.6620	3.0270	2.8016
TNT-m	N_7	2.2252	3.0036	2.9927	3.3891	3.1524
TNT-m	N_8	2.2657	3.0308	3.0212	3.4288	3.1865
TNT-m	N_9	2.1424	2.9516	2.9397	3.3291	3.1031
TNT-o	N_7	2.2737	3.0481	3.0362	3.4304	3.1912
TNT-o	N_8	2.1502	2.9324	2.9303	3.3447	3.1150
TNT-o	N_9	2.3006	3.0629	3.0516	3.4489	3.2067
TNB	N_{10}	2.2638	3.0102	3.0035	3.4296	3.0035
TNB	N_{11}	2.2677	3.0164	3.0103	3.4345	3.0103
TNB	N_{12}	2.1899	2.9200	2.9272	3.3983	2.9272
TNX	N_{10}	2.2725	3.0385	3.0274	3.4236	3.1847
TNX	N_{11}	2.1214	2.9546	2.9439	3.3288	3.1115
TNX	N_{18}	2.2726	3.0386	3.0275	3.4237	3.1848

Table 9.7: ^{14}N quadrupole coupling constants, C_q/MHz, from B3LYP calculations on single molecules from crystal structure data.

molecule	site	basis set				
		6-311G	cc-pVDZ	cc-pCVDZ	cc-pVTZ	cc-pCVTZ
RDX	N_4	-7.1488	-6.0997	-6.2830	-6.2440	-6.2440
RDX	N_5	-7.1904	-6.1104	-6.3105	-6.3518	-6.3518
RDX	N_6	-7.2082	-6.1341	-6.3295	-6.3707	-6.3707
RDX	N_7	-0.8885	0.5696	0.5818	-0.6424	-0.6424
RDX	N_8	-0.8794	0.5786	0.5997	0.6754	0.6754
RDX	N_9	-0.8612	0.5782	0.5990	0.6813	0.6813
tetryl	N_8	0.7524	-0.6660	-0.6936	0.9766	0.7829
tetryl	N_9	0.8280	-0.8021	-0.8311	1.0537	-0.9293
tetryl	N_{10}	0.8437	-0.7024	-0.7263	0.9236	-0.8146
tetryl	N_{11}	-7.8619	-6.8153	-7.0046	-6.9535	-6.9735
tetryl	N_{12}	-1.0382	0.6279	0.6428	-0.6477	0.5792
TNT-m	N_7	0.8916	-0.8833	-0.9215	-1.1407	-1.0270
TNT-m	N_8	0.8804	-0.8810	-0.9139	-1.1572	-1.0343
TNT-m	N_9	0.9225	-0.9090	-0.9332	-1.1563	-1.0464
TNT-o	N_7	0.9344	-0.9357	-0.9671	-1.1886	-1.0753
TNT-o	N_8	0.9413	-0.9394	-0.9679	-1.1937	-1.0846
TNT-o	N_9	0.9066	-0.8981	-0.9367	-1.1689	-1.0541
TNB	N_{10}	0.8044	-0.8387	-0.8681	1.1131	-0.9803
TNB	N_{11}	0.8637	-0.9032	-0.9330	1.1577	-1.0253
TNB	N_{12}	0.7333	-0.8196	-0.8649	1.1880	-0.9897
TNX-c1	N_{10}	0.8974	-0.8835	-0.9211	-1.1330	-1.0224
TNX-c1	N_{11}	0.9855	-0.9679	-1.0011	-1.2433	-1.1333
TNX-c1	N_{18}	0.8976	-0.8847	-0.9212	-1.1331	-1.0225

Table 9.8: ^{14}N *EFG* asymmetry, η, from RHF calculations on single molecules from crystal structure data.

molecule	site	basis set				
		6-311G	cc-pVDZ	cc-pCVDZ	cc-pVTZ	cc-pCVTZ
RDX	N_4	0.5473	0.5343	0.5399	0.5674	0.5566
RDX	N_5	0.5594	0.5549	0.5612	0.5918	0.5801
RDX	N_6	0.5653	0.5620	0.5689	0.6022	0.5896
RDX	N_7	0.7193	0.6128	0.6064	0.5486	0.5647
RDX	N_8	0.5552	0.5221	0.5237	0.5248	0.5312
RDX	N_9	0.5544	0.5218	0.5249	0.5322	0.5380
tetryl	N_8	0.4005	0.1232	0.1426	0.1130	0.1264
tetryl	N_9	0.4983	0.1895	0.2104	0.1845	0.2001
tetryl	N_{10}	0.4623	0.1359	0.1582	0.1426	0.1560
tetryl	N_{11}	0.4199	0.3976	0.4032	0.4312	0.4230
tetryl	N_{12}	0.7475	0.6397	0.6308	0.5582	0.5720
TNT-m	N_7	0.5882	0.2651	0.2895	0.2716	0.2864
TNT-m	N_8	0.5676	0.2514	0.2783	0.2670	0.2811
TNT-m	N_9	0.6299	0.2662	0.2912	0.2817	0.2956
TNT-o	N_7	0.6105	0.2820	0.3075	0.2894	0.3053
TNT-o	N_8	0.6369	0.2609	0.2796	0.2523	0.2673
TNT-o	N_9	0.5708	0.2554	0.2825	0.2718	0.2862
TNB	N_{10}	0.4993	0.2130	0.2328	0.2032	0.2328
TNB	N_{11}	0.5439	0.2210	0.2372	0.1913	0.2372
TNB	N_{12}	0.4892	0.2164	0.2371	0.2073	0.2371
TNX	N_{10}	0.5818	0.2620	0.2867	0.2663	0.2821
TNX	N_{11}	0.7219	0.3181	0.3439	0.3359	0.3502
TNX	N_{18}	0.5819	0.2620	0.2868	0.2664	0.2822

Table 9.9: ^{14}N *EFG* asymmetry, η, from B3LYP calculations on single molecules from crystal structure data.

molecule	site	basis set				
		6-311G	cc-pVDZ	cc-pCVDZ	cc-pVTZ	cc-pCVTZ
RDX	N_4	0.4923	0.4810	0.4827	0.5014	0.5014
RDX	N_5	0.4907	0.4828	0.4870	0.5112	0.5112
RDX	N_6	0.4941	0.4848	0.4917	0.5184	0.5184
RDX	N_7	0.9037	0.9187	0.8259	0.6872	0.6872
RDX	N_8	0.6449	0.5397	0.4899	0.8332	0.8332
RDX	N_9	0.6505	0.5637	0.5128	0.8579	0.8579
tetryl	N_8	0.3932	0.6802	0.6095	0.8072	0.9882
tetryl	N_9	0.6566	0.6167	0.5503	0.9698	0.8482
tetryl	N_{10}	0.3411	0.5694	0.4947	0.9825	0.8324
tetryl	N_{11}	0.3703	0.3431	0.3473	0.3784	0.3679
tetryl	N_{12}	0.7540	0.5324	0.4206	0.6738	0.8765
TNT-m	N_7	0.7179	0.4816	0.4307	0.8379	0.6825
TNT-m	N_8	0.7325	0.5413	0.4565	0.8511	0.6906
TNT-m	N_9	0.6813	0.4680	0.4080	0.7977	0.6615
TNT-o	N_7	0.7523	0.4602	0.3955	0.7819	0.6264
TNT-o	N_8	0.7970	0.4774	0.4421	0.8688	0.7351
TNT-o	N_9	0.7451	0.5016	0.4223	0.8013	0.6398
TNB	N_{10}	0.8174	0.6529	0.5798	0.9637	0.8596
TNB	N_{11}	0.9163	0.6207	0.5601	0.9537	0.8689
TNB	N_{12}	0.9012	0.7274	0.6659	0.8677	0.9821
TNX-cl	N_{10}	0.7179	0.5021	0.4309	0.8426	0.6767
TNX-cl	N_{11}	0.7321	0.3880	0.3431	0.7084	0.5876
TNX-cl	N_{18}	0.7179	0.5027	0.4308	0.8424	0.6764

Table 9.10: ^{14}N NQR high transition frequency, ν_{hi}, from RHF calculations on single molecules from crystal structure data.

molecule	site	6-311G	cc-pVDZ	cc-pCVDZ	cc-pVTZ	cc-pCVTZ
RDX	N_4	6.8712	5.9013	5.9960	5.9614	5.8974
RDX	N_5	7.1022	6.0754	6.1870	6.2661	6.1725
RDX	N_6	7.1526	6.1213	6.2344	6.3205	6.2236
RDX	N_7	1.7750	2.4695	2.4468	2.7346	2.5398
RDX	N_8	1.6186	2.3301	2.3174	2.6436	2.4508
RDX	N_9	1.6177	2.3250	2.3136	2.6433	2.4505
tetryl	N_8	1.7173	2.1891	2.1997	2.5113	2.3351
tetryl	N_9	1.8801	2.3359	2.3439	2.6566	2.4764
tetryl	N_{10}	1.7088	2.1947	2.1997	2.5001	2.3307
tetryl	N_{11}	7.4369	6.4612	6.5555	6.5545	6.4636
tetryl	N_{12}	1.7512	2.4423	2.4163	2.6927	2.5019
TNT-m	N_7	1.9961	2.4517	2.4612	2.7719	2.5900
TNT-m	N_8	2.0208	2.4636	2.4761	2.8005	2.6138
TNT-m	N_9	1.9441	2.4101	2.4188	2.7313	2.5566
TNT-o	N_7	2.0523	2.5010	2.5106	2.8210	2.6370
TNT-o	N_8	1.9550	2.3905	2.4026	2.7195	2.5444
TNT-o	N_9	2.0538	2.4927	2.5042	2.8211	2.6344
TNB	N_{10}	1.9804	2.4180	2.4274	2.7464	2.4274
TNB	N_{11}	2.0092	2.4290	2.4362	2.7401	2.4362
TNB	N_{12}	1.9103	2.3480	2.3689	2.7248	2.3689
TNX	N_{10}	2.0349	2.4779	2.4875	2.7957	2.6132
TNX	N_{11}	1.9740	2.4508	2.4611	2.7761	2.6061
TNX	N_{18}	2.0351	2.4781	2.4877	2.7958	2.6133

Table 9.11: ^{14}N NQR high transition frequency, ν_{hi}, from B3LYP calculations on single molecules from crystal structure data.

molecule	site	basis set				
		6-311G	cc-pVDZ	cc-pCVDZ	cc-pVTZ	cc-pCVTZ
RDX	N_4	6.2415	5.3082	5.4705	5.4657	5.4657
RDX	N_5	6.2749	5.3203	5.5013	5.5756	5.5756
RDX	N_6	6.2966	5.3440	5.5252	5.6036	5.6036
RDX	N_7	0.8672	0.5581	0.5565	0.5922	0.5922
RDX	N_8	0.8013	0.5120	0.5232	0.6473	0.6473
RDX	N_9	0.7860	0.5151	0.5261	0.6571	0.6571
tetryl	N_8	0.6383	0.6128	0.6259	0.9295	0.7806
tetryl	N_9	0.7569	0.7253	0.7376	1.0457	0.8940
tetryl	N_{10}	0.7047	0.6268	0.6345	0.9196	0.7804
tetryl	N_{11}	6.6243	5.6961	5.8617	5.8729	5.8716
tetryl	N_{12}	0.9744	0.5545	0.5497	0.5949	0.5613
TNT-m	N_7	0.8288	0.7688	0.7903	1.0945	0.9455
TNT-m	N_8	0.8215	0.7800	0.7898	1.1142	0.9543
TNT-m	N_9	0.8490	0.7881	0.7951	1.0978	0.9578
TNT-o	N_7	0.8765	0.8094	0.8210	1.1238	0.9748
TNT-o	N_8	0.8936	0.8167	0.8329	1.1545	1.0128
TNT-o	N_9	0.8488	0.7862	0.8014	1.1108	0.9592
TNB	N_{10}	0.7677	0.7659	0.7769	1.1031	0.9458
TNB	N_{11}	0.8456	0.8175	0.8304	1.1443	0.9917
TNB	N_{12}	0.7152	0.7637	0.7927	1.1488	0.9853
TNX-cl	N_{10}	0.8341	0.7735	0.7900	1.0884	0.9397
TNX-cl	N_{11}	0.9195	0.8198	0.8367	1.1527	1.0165
TNX-cl	N_{18}	0.8343	0.7747	0.7901	1.0884	0.9398

Table 9.12: ^{14}N NQR low transition frequency, ν_{lo}, from RHF calculations on single molecules from crystal structure data.

molecule	site	6-311G	cc-pVDZ	basis set cc-pCVDZ	cc-pVTZ	cc-pCVTZ
RDX	N_4	4.7509	4.1170	4.1670	4.0650	4.0515
RDX	N_5	4.8697	4.1786	4.2371	4.2013	4.1723
RDX	N_6	4.8843	4.1897	4.2469	4.2073	4.1792
RDX	N_7	1.0884	1.6318	1.6240	1.8891	1.7351
RDX	N_8	1.1131	1.6393	1.6286	1.8563	1.7134
RDX	N_9	1.1130	1.6360	1.6246	1.8468	1.7053
tetryl	N_8	1.3128	2.0163	2.0001	2.3290	2.1463
tetryl	N_9	1.3445	2.0583	2.0366	2.3489	2.1667
tetryl	N_{10}	1.2524	2.0045	1.9793	2.2731	2.1004
tetryl	N_{11}	5.6105	4.9489	5.0022	4.9070	4.8662
tetryl	N_{12}	1.0526	1.5838	1.5767	1.8478	1.7006
TNT-m	N_7	1.3417	2.0536	2.0279	2.3116	2.1387
TNT-m	N_8	1.3778	2.0826	2.0557	2.3427	2.1659
TNT-m	N_9	1.2694	2.0173	1.9908	2.2624	2.0980
TNT-o	N_7	1.3583	2.0711	2.0437	2.3246	2.1499
TNT-o	N_8	1.2703	2.0080	1.9929	2.2976	2.1281
TNT-o	N_9	1.3971	2.1016	2.0732	2.3523	2.1756
TNB	N_{10}	1.4153	2.0974	2.0778	2.3979	2.0778
TNB	N_{11}	1.3924	2.0956	2.0792	2.4116	2.0792
TNB	N_{12}	1.3746	2.0320	2.0219	2.3725	2.0219
TNX	N_{10}	1.3739	2.0799	2.0535	2.3398	2.1639
TNX	N_{11}	1.2082	1.9810	1.9548	2.2170	2.0612
TNX	N_{18}	1.3739	2.0799	2.0535	2.3398	2.1639

Table 9.13: ^{14}N NQR low transition frequency, ν_{lo}, from B3LYP calculations on single molecules from crystal structure data.

molecule	site	6-311G	cc-pVDZ	basis set cc-pCVDZ	cc-pVTZ	cc-pCVTZ
RDX	N_4	4.4817	3.8414	3.9540	3.9002	3.9002
RDX	N_5	4.5108	3.8452	3.9645	3.9521	3.9521
RDX	N_6	4.5157	3.8571	3.9691	3.9524	3.9524
RDX	N_7	0.4657	0.2964	0.3162	0.3715	0.3715
RDX	N_8	0.5178	0.3559	0.3763	0.3659	0.3659
RDX	N_9	0.5059	0.3522	0.3725	0.3648	0.3648
tetryl	N_8	0.4904	0.3863	0.4145	0.5354	0.3937
tetryl	N_9	0.4851	0.4779	0.5090	0.5348	0.4999
tetryl	N_{10}	0.5608	0.4268	0.4549	0.4659	0.4414
tetryl	N_{11}	5.1685	4.5268	4.6452	4.5574	4.5886
tetryl	N_{12}	0.5830	0.3873	0.4145	0.3767	0.3075
TNT-m	N_7	0.5087	0.5561	0.5919	0.6166	0.5950
TNT-m	N_8	0.4991	0.5416	0.5811	0.6217	0.5971
TNT-m	N_9	0.5347	0.5754	0.6047	0.6366	0.6117
TNT-o	N_7	0.5251	0.5941	0.6297	0.6591	0.6381
TNT-o	N_8	0.5185	0.5924	0.6189	0.6360	0.6141
TNT-o	N_9	0.5111	0.5610	0.6036	0.6425	0.6220
TNB	N_{10}	0.4389	0.4921	0.5253	0.5667	0.5245
TNB	N_{11}	0.4499	0.5372	0.5691	0.5922	0.5463
TNB	N_{12}	0.3848	0.4656	0.5047	0.6333	0.4993
TNX-cl	N_{10}	0.5120	0.5517	0.5916	0.6111	0.5938
TNX-cl	N_{11}	0.5588	0.6320	0.6650	0.7123	0.6835
TNX-cl	N_{18}	0.5121	0.5524	0.5917	0.6112	0.5939

Table 9.14: ^{14}N NQR transition frequency, ν_d, from RHF calculations on single molecules from crystal structure data.

| molecule | site | basis set | | | | |
		6-311G	cc-pVDZ	cc-pCVDZ	cc-pVTZ	cc-pCVTZ
RDX	N_4	2.1203	1.7843	1.8290	1.8964	1.8459
RDX	N_5	2.2325	1.8968	1.9499	2.0649	2.0002
RDX	N_6	2.2682	1.9316	1.9875	2.1132	2.0445
RDX	N_7	0.6866	0.8377	0.8228	0.8455	0.8047
RDX	N_8	0.5055	0.6908	0.6888	0.7872	0.7374
RDX	N_9	0.5047	0.6890	0.6890	0.7965	0.7452
tetryl	N_8	0.4045	0.1728	0.1996	0.1823	0.1888
tetryl	N_9	0.5356	0.2776	0.3073	0.3078	0.3097
tetryl	N_{10}	0.4563	0.1902	0.2204	0.2269	0.2304
tetryl	N_{11}	1.8263	1.5123	1.5533	1.6475	1.5974
tetryl	N_{12}	0.6986	0.8585	0.8396	0.8449	0.8013
TNT-m	N_7	0.6544	0.3981	0.4332	0.4603	0.4514
TNT-m	N_8	0.6430	0.3810	0.4204	0.4578	0.4479
TNT-m	N_9	0.6747	0.3928	0.4281	0.4689	0.4586
TNT-o	N_7	0.6940	0.4298	0.4668	0.4964	0.4871
TNT-o	N_8	0.6848	0.3825	0.4096	0.4219	0.4163
TNT-o	N_9	0.6566	0.3911	0.4310	0.4687	0.4588
TNB	N_{10}	0.5652	0.3206	0.3496	0.3485	0.3496
TNB	N_{11}	0.6168	0.3333	0.3570	0.3285	0.3570
TNB	N_{12}	0.5357	0.3160	0.3470	0.3523	0.3470
TNX	N_{10}	0.6611	0.3981	0.4340	0.4559	0.4493
TNX	N_{11}	0.7657	0.4699	0.5062	0.5591	0.5449
TNX	N_{18}	0.6612	0.3981	0.4341	0.4560	0.4494

Table 9.15: ^{14}N NQR transition frequency, ν_d, from B3LYP calculations on single molecules from crystal structure data.

molecule	site	basis set				
		6-311G	cc-pVDZ	cc-pCVDZ	cc-pVTZ	cc-pCVTZ
RDX	N_4	1.7598	1.4669	1.5165	1.5655	1.5655
RDX	N_5	1.7641	1.4751	1.5367	1.6235	1.6235
RDX	N_6	1.7808	1.4869	1.5560	1.6512	1.6512
RDX	N_7	0.4015	0.2617	0.2403	0.2207	0.2207
RDX	N_8	0.2836	0.1561	0.1469	0.2814	0.2814
RDX	N_9	0.2801	0.1630	0.1536	0.2922	0.2922
tetryl	N_8	0.1479	0.2265	0.2114	0.3941	0.3868
tetryl	N_9	0.2718	0.2473	0.2287	0.5109	0.3941
tetryl	N_{10}	0.1439	0.2000	0.1796	0.4537	0.3390
tetryl	N_{11}	1.4558	1.1693	1.2165	1.3155	1.2829
tetryl	N_{12}	0.3914	0.1671	0.1352	0.2182	0.2538
TNT-m	N_7	0.3201	0.2127	0.1984	0.4779	0.3505
TNT-m	N_8	0.3224	0.2384	0.2086	0.4925	0.3571
TNT-m	N_9	0.3142	0.2127	0.1904	0.4612	0.3461
TNT-o	N_7	0.3515	0.2153	0.1913	0.4647	0.3367
TNT-o	N_8	0.3751	0.2243	0.2139	0.5185	0.3986
TNT-o	N_9	0.3377	0.2252	0.1978	0.4683	0.3372
TNB	N_{10}	0.3288	0.2738	0.2517	0.5364	0.4213
TNB	N_{11}	0.3957	0.2803	0.2613	0.5520	0.4455
TNB	N_{12}	0.3304	0.2981	0.2880	0.5155	0.4860
TNX-c1	N_{10}	0.3221	0.2218	0.1984	0.4773	0.3459
TNX-c1	N_{11}	0.3607	0.1878	0.1717	0.4404	0.3330
TNX-c1	N_{18}	0.3222	0.2224	0.1984	0.4772	0.3458

Table 9.16: tetryl and mimics. Data from B3LYP/cc-pVDZ optimization of single molecules from the crystal structures. The ^{14}N quadrupole coupling constant, C_q, and all transitions frequencies (ν_-, ν_+ and ν_d) are givin in *MHz*. The ν_d from experiment is also shown for comparison, using assignments from table 9.1

molecule	N	C_q	η	ν_+	ν_-	ν_d	$\nu_{d,\text{expt}}$
rdx-xtal	4	-5.901	0.52	5.200	3.652	1.549	1.842
rdx-xtal	5	-6.174	0.49	5.392	3.868	1.524	1.807
rdx-xtal	6	-6.175	0.49	5.393	3.870	1.524	1.724
rdx-xtal	7	0.523	0.54	0.462	0.322	0.140	
rdx-xtal	8	0.582	0.41	0.497	0.377	0.121	
rdx-xtal	9	0.583	0.42	0.498	0.376	0.121	
tetryl-c1-xtal	8	-0.694	0.56	0.617	0.424	0.193	
tetryl-c1-xtal	9	-0.803	0.60	0.723	0.482	0.241	
tetryl-c1-xtal	10	-0.725	0.57	0.647	0.440	0.207	
tetryl-c1-xtal	11	-6.761	0.37	5.695	4.446	1.249	
tetryl-c1-xtal	12	0.615	0.42	0.526	0.396	0.129	
tnb-xtal	10	-0.836	0.60	0.752	0.502	0.250	0.205
tnb-xtal	11	-0.837	0.60	0.753	0.503	0.250	0.201
tnb-xtal	12	-0.837	0.60	0.753	0.503	0.250	0.197
tnt-xtal-m	7	-0.856	0.50	0.749	0.535	0.213	0.108
tnt-xtal-m	8	-0.850	0.59	0.764	0.511	0.253	0.132
tnt-xtal-m	9	-0.856	0.50	0.749	0.535	0.213	0.077
tnt-xtal-o	7	-0.856	0.50	0.749	0.535	0.213	0.109
tnt-xtal-o	8	-0.856	0.50	0.748	0.535	0.213	0.075
tnt-xtal-o	9	-0.850	0.59	0.764	0.511	0.253	0.135
tnx-xtal-c1	10	-0.873	0.53	0.771	0.539	0.231	0.127
tnx-xtal-c1	11	-0.977	0.36	0.820	0.646	0.173	0.063
tnx-xtal-c1	18	-0.873	0.53	0.771	0.539	0.231	

Table 9.17: ^{14}N quadrupole coupling constants, C_q/MHz, from RHF and B3LYP calculations on single molecules from optimized structures.

molecule	site	basis set				
		6-311G	cc-pVDZ	cc-pCVDZ	cc-pVTZ	cc-pCVTZ
		RHF				
RDX	N_3	1.8203	2.4053	2.3970	2.8380	2.6061
RDX	N_6	-8.1811	-7.3851	-7.4825	-7.2752	-7.2358
tetryl	N_1	-8.5747	-7.6868	-7.7859	-7.6813	-7.5978
tetryl	N_9	2.0806	2.7320	2.7414	3.1999	2.9623
tetryl	N_{12}	2.2340	2.8396	2.8504	3.3281	3.0783
tetryl	N_{19}	1.9381	2.5082	2.5051	2.9442	2.7134
TNT	N_9	2.2793	2.8914	2.9002	3.3435	3.1059
TNT	N_{12}	2.3535	2.9265	2.9377	3.4130	3.1616
TNB	N_3	2.3301	2.9086	2.9200	3.3889	Na
TNX	N_9	2.3427	2.9336	2.9430	Na	Na
TNX	N_{12}	2.1707	2.8894	2.8958	Na	Na

molecule	site	6-311G	cc-pVDZ
		B3LYP	
RDX	N_3	-1.2980	1.5218
RDX	N_6	-7.7948	-7.6646
tetryl	N_9	0.8984	-0.6915
tetryl	N_{12}	0.8876	-0.7927
tetryl	N_{19}	-1.0742	0.5308
TNT	N_9	2.0660	2.7840
TNT	N_{12}	-1.1249	1.2291
TNB	N_1	0.8952	-1.1829
TNB	N_2	0.8952	1.2367
TNB	N_3	0.8952	-1.3879
TNX	N_9	0.9712	1.1709
TNX	N_{12}	2.1823	2.9403

Table 9.18: ^{14}N EFG asymmetry, η, from RHF and B3LYP calculations on single molecules from optimized structures.

molecule	site	6-311G	cc-pVDZ	basis set cc-pCVDZ	cc-pVTZ	cc-pCVTZ
				RHF		
RDX	N_3	0.7788	0.6361	0.6398	0.6046	0.6212
RDX	N_6	0.4046	0.3580	0.3639	0.4011	0.3873
tetryl	N_1	0.4465	0.3952	0.4017	0.4316	0.4208
tetryl	N_9	0.4964	0.1750	0.1915	0.1416	0.1545
tetryl	N_{12}	0.5166	0.2078	0.2223	0.1619	0.1785
tetryl	N_{19}	0.6836	0.6157	0.6159	0.5813	0.5919
TNT	N_9	0.5830	0.2679	0.2832	0.2309	0.2464
TNT	N_{12}	0.5458	0.2417	0.2568	0.1959	0.2130
TNB	N_3	0.5463	0.2367	0.2513	0.1842	Na
TNX	N_9	0.5758	0.2725	0.2876	Na	Na
TNX	N_{12}	0.7413	0.3349	0.3535	Na	Na

molecule	site	6-311G	cc-pVDZ
		B3LYP	
RDX	N_3	0.7769	0.8394
RDX	N_6	0.3379	0.2506
tetryl	N_9	0.1138	0.5296
tetryl	N_{12}	0.4205	0.6001
tetryl	N_{19}	0.7207	0.7032
TNT	N_9	0.7738	0.6076
TNT	N_{12}	0.2091	0.9368
TNB	N_1	0.5278	0.4787
TNB	N_2	0.5277	0.8014
TNB	N_3	0.5277	0.5898
TNX	N_9	0.4338	0.5167
TNX	N_{12}	0.8157	0.7551

Table 9.19: ^{14}N NQR high transition frequency, ν_{hi}, from RHF and B3LYP calculations on single molecules from optimized structures.

molecule	site	6-311G	cc-pVDZ	basis set cc-pCVDZ	cc-pVTZ	cc-pCVTZ
				RHF		
RDX	N_3	1.7196	2.1865	2.1811	2.5574	2.3593
RDX	N_6	6.9632	6.1998	6.2926	6.1858	6.1275
tetryl	N_1	7.3883	6.5245	6.6213	6.5897	6.4977
tetryl	N_9	1.8186	2.1685	2.1873	2.5131	2.3361
tetryl	N_{12}	1.9640	2.2772	2.2962	2.6308	2.4461
tetryl	N_{19}	1.7848	2.2673	2.2646	2.6360	2.4365
TNT	N_9	2.0417	2.3622	2.3805	2.7007	2.5207
TNT	N_{12}	2.0863	2.3717	2.3918	2.7268	2.5395
TNB	N_3	2.0658	2.3535	2.3734	2.6978	Na
TNX	N_9	2.0943	2.4000	2.4188	Na	Na
TNX	N_{12}	2.0303	2.4090	2.4278	Na	Na

molecule	site	6-311G	cc-pVDZ
		B3LYP	
RDX	N_3	1.2256	1.4607
RDX	N_6	6.5046	6.2287
tetryl	N_9	0.6994	0.6102
tetryl	N_{12}	0.7590	0.7135
tetryl	N_{19}	0.9992	0.4914
TNT	N_9	1.9492	2.5109
TNT	N_{12}	0.9024	1.2097
TNB	N_1	0.7895	1.0287
TNB	N_2	0.7895	1.1752
TNB	N_3	0.7895	1.2455
TNX	N_9	0.8338	1.0294
TNX	N_{12}	2.0817	2.7603

Table 9.20: ^{14}N NQR low transition frequency, ν_{lo}, from RHF and B3LYP calculations on single molecules from optimized structures.

| molecule | site | basis set | | | | |
		6-311G	cc-pVDZ	cc-pCVDZ	cc-pVTZ	cc-pCVTZ
				RHF		
RDX	N_3	1.0109	1.4215	1.4144	1.6995	1.5498
RDX	N_6	5.3084	4.8778	4.9311	4.7269	4.7262
tetryl	N_1	5.4738	5.0057	5.0575	4.9322	4.8990
tetryl	N_9	1.3022	1.9294	1.9249	2.2867	2.1073
tetryl	N_{12}	1.3870	1.9822	1.9794	2.3613	2.1713
tetryl	N_{19}	1.1224	1.4951	1.4931	1.7802	1.6336
TNT	N_9	1.3773	1.9749	1.9698	2.3146	2.1381
TNT	N_{12}	1.4440	2.0181	2.0147	2.3926	2.2029
TNB	N_3	1.4293	2.0093	2.0065	2.3856	Na
TNX	N_9	1.4198	2.0004	1.9957	Na	Na
TNX	N_{12}	1.2258	1.9252	1.9159	Na	Na

molecule	site	6-311G	cc-pVDZ
		B3LYP	
RDX	N_3	0.7214	0.8220
RDX	N_6	5.1875	5.2683
tetryl	N_9	0.6483	0.4271
tetryl	N_{12}	0.5724	0.4756
tetryl	N_{19}	0.6121	0.3048
TNT	N_9	1.1498	1.6651
TNT	N_{12}	0.7848	0.6340
TNB	N_1	0.5533	0.7456
TNB	N_2	0.5533	0.6797
TNB	N_3	0.5533	0.8362
TNX	N_9	0.6231	0.7269
TNX	N_{12}	1.1917	1.6502

Table 9.21: ^{14}N NQR transition frequency, ν_d, from RHF and B3LYP calculations on single molecules from optimized structures.

molecule	site	6-311G	cc-pVDZ	cc-pCVDZ	cc-pVTZ	cc-pCVTZ
				basis set		
				RHF		
RDX	N_3	0.7088	0.7650	0.7667	0.8579	0.8095
RDX	N_6	1.6548	1.3219	1.3615	1.4589	1.4013
tetryl	N_1	1.9144	1.5189	1.5638	1.6575	1.5987
tetryl	N_9	0.5164	0.2391	0.2624	0.2265	0.2289
tetryl	N_{12}	0.5770	0.2950	0.3168	0.2695	0.2747
tetryl	N_{19}	0.6624	0.7722	0.7715	0.8558	0.8030
TNT	N_9	0.6644	0.3873	0.4107	0.3861	0.3826
TNT	N_{12}	0.6423	0.3537	0.3772	0.3342	0.3367
TNB	N_3	0.6365	0.3442	0.3669	0.3121	Na
TNX	N_9	0.6745	0.3996	0.4232	Na	Na
TNX	N_{12}	0.8046	0.4838	0.5119	Na	Na

molecule	site	6-311G	cc-pVDZ
			B3LYP
RDX	N_3	0.5042	0.6387
RDX	N_6	1.3171	0.9604
tetryl	N_9	0.0511	0.1831
tetryl	N_{12}	0.1866	0.2378
tetryl	N_{19}	0.3871	0.1866
TNT	N_9	0.7993	0.8458
TNT	N_{12}	0.1176	0.5757
TNB	N_1	0.2362	0.2831
TNB	N_2	0.2362	0.4955
TNB	N_3	0.2362	0.4093
TNX	N_9	0.2107	0.3025
TNX	N_{12}	0.8900	1.1101

too high of a symmetry prevented rearrangements of functional groups with optimization. In reality there may also be significant interaction between the molecules in the crystal which are completely neglected by this single molecule method.

Other studies have seen similar differences in transition frequencies for N in -NO_2 groups between calculation and experiment; they have suggested intermolecular interactions such as hydrogen bonding of O with H between molecules [252]. Because H atoms have little electron density their positions are not well determined by X-ray crystallography. If hydrogen bonding interactions are present and they do effect the EFG at the N nuclei, then small uncertainties in the H atoms position could make big differences in the transition frequencies. When the positions for three H atoms in cocaine were redetermined the agreement of the N transition frequencies between calculation and experiment improved [251]. It should also be carefully noted, that some studies [252, 251, 63] have obtained good agreement with experiment for single molecules by adjusting the value of the quadrupole moment instead of using the literature value [65] and using 298K NMR data [63]. It is also worth noting that the -NO_2 groups in the symmetrized molecules are much more planar than those in the crystal structures. Some suggest a relationship between the angle of the -NO_2 groups with the plane and the frequencies [253].

9.4   Conclusion

The preliminary calculations for N in NH_3 show our single-molecule MO approach to work well for small N compounds. The single-molecule MO approach as implemented here did not reproduce experimental values well for N in the -NO_2 groups of nitroaromatic compounds. A fitting procedure did

not improve the values significantly. Including more molecules with a larger range of C_q values could improve the fit. A set of experimental data, acquired with the same precision, would serve to clarify where errors may occur in the predictions from calculation. For these compounds B3LYP calculations using single point calculations on single molecule geometry from crystal structures produces C_q magnitudes closer to experiment than RHF, while RHF produces an η close to that of experiment. Overall the best calculations of NQR frequencies are from B3LYP/cc-pVDZ using the coordinates for single molecules taken from crystal structures and then optimized. Exploration of larger basis set space is necessary to increase confidence.

In conclusion, while the single-molecule MO approach shows promise in its application to small N molecules such as NH_3, further investigation needs to be brought to bear to improve the situation for N in the -NO_2 groups.

CHAPTER 10

METHYL-ALUMINUM OXIDE MODELS

10.1 Introduction

The most exciting project to date is the application of the single-molecule MO and full-crystal FP-LAPW DFT methods to explore relationships between spectra and possible structures for Al containing structures similar to methyl aluminum oxide (MAO). MAO is a co-catalyst in new-generation Ziegler-Natta catalysts for olefin polymerization [262, 263, 264] produced and sold by scientists at Albemarle Corporation. The structure of MAO is not well characterized and the method of catalytic activity is not well understood. The proposed model compounds include a variety of Al coordination and shapes, including cages, rings and propeller shapes of Al, N and O combinations. Those with N-Al bonds are aluminum amides or aminoalanes and those with $(R-Al-N-R')_n$ structure are iminoalanes. The $[Me\,Al\{N-2,6-iPr_2C_6H_3)\}]_3$ structure may be a world record value of C_q. NMR analysis of the model structures is hindered by the large quadrupolar coupling constants that make

conventional magic angle spinning (MAS) spectra difficult to resolve at ordinary magnetic fields. Experimentalists characterize the active catalytic site with NQR, which is better for the large quadrupolar interactions at the ^{27}Al sites, and extremely high magnetic field MAS NMR at the National High Magnetic Field Lab in the state of Florida. These compounds are difficult to synthesize, may contain multiple phases and can degrade rapidly and catch fire when exposed to the atmosphere. With such unusual and extreme materials and very high C_q values, the additional confirmation of a compounds identity by calculations is vital.

In similar areas, *ab initio* studies exist for aluminosilicate drum molecules and alumoxane [265], aluminosilicate glasses and melts [266], aluminosilicate and borosilicate cages [267], and complexes with Al(CH$_3$) and MAO [268].

The MAO models we study are dimethyl aluminum [269], diaminato aluminum [270], tri aluminum [271], hexa aluminum [272], and tetra aluminum [273] (cf. table 10.1).

10.2 Method

First, we examine a single molecule of the smallest compound, cyclodi-m-dimethylamido-bis(dimethylaluminum)[269], [{Me$_2$Al}{NMe$_2$}]$_2$ which we refer to as dimethyl aluminum. Results from two methods, two basis sets and three structures are shown in table 10.2. The methods are:

1. Restricted Hartree-Fock (RHF) with GAMESS [43] and

2. Becke's 3-parameter Lee-Yang-Parr (B3LYP) with Gaussian [41].

The basis sets are:

1. correlation consistent double (cc-pVDZ) and

2. triple zeta (cc-pVTZ) with additional polarization functions [134].

Table 10.1: MAO models names, formulae, symmetry point group, number of electrons and atoms used in calculations. ^{a} Structures correspond to a truncated version of the actual molecule, i.e. Me is substituted for C_6H_5 in the hexa aluminum, $-2, 6 - iPr_2C_6H_3$ in the tri aluminum and $-2, 6 - iPr_2C_6H_3$ in the tetra aluminum. For these truncated structures the full molecule is also shown beneath for comparison.

molecule	formula, pt. group	e^-	atoms (unique)
mono aluminum	$Al(Me_2N)_3$, D_3	88	28(6)
dimethyl aluminum	$[\{Me_2Al\}\{NMe_2\}]_2$, C_{2v}	112	36(14)
diaminato aluminum	$[Al(NMe_2)_3]_2$, C_{2h}	176	56(18)
tri aluminum^a	$[\{MeAl\}\{NMe\}]_3$, C_{3v}	114	30(8)
tri aluminum	$[MeAl\{N - 2, 6 - iPr_2C_6H_3)\}]_3$, C_{3v}	354	105(26)
hexa aluminum^a	$[\{MeAl\}\{NMe\}]_6$, D_{3d}	228	60(8)
hexa aluminum	$[\{MeAl\}\{NC_6C_5\}]_6$, D_{3d}	420	102(16)
tetra aluminum^a	$[Al[(\mu\text{-}OMe)_2Al(OMe)_2]_3$, D_3	256	64(12)
tetra aluminum	$[Al[(\mu\text{-}O^iPr)_2Al(O^iPr)_2]_3$,	448	136

The three types of single-molecule structures at which the EFG tensors are calculated are:

1. experimentally determined via X-ray crystallography [269],

2. D_{2h} symmetry constrained optimized,

3. C_{2v} symmetry constrained optimized.

The energy of the C_{2v} structure is the lowest. The RHF/cc-pVTZ with optimized structure is the least computationally intensive method which proved adequate to reproduce the approximate magnitude of C_q and value of η. The sign of C_q changes because the q_{xx} and q_{yy} components of the EFG are opposite in sign and very close in value to each other. Because they are assigned by magnitude, small changes in structure, method or basis set cause them to switch.

Second, we examine the full crystal of dimethyl aluminum. These results further validate the C_{2v} optimized single-molecule MO results. FP-

Table 10.2: ^{27}Al nuclear quadrupole coupling constants C_q in megahertz for the smallest dimer, $[\{Me_2Al\}\{NMe_2\}]_2$ (dimethyl aluminum), using RHF and B3LYP methods with cc-pVDZ and cc-pVTZ basis sets at ^{a} crystal structure coordinates[269], ^{b} optimized coordinates of D_{2h} symmetry, ^{c} optimized coordinates of C_{2v} symmetry, ^{d} fully optimized crystal structure coordinates of C_1 symmetry. Experimental values (marked 'expt.') are from NMR experiments by Anthony Mrse, Earl Emery, Pam Bryant and Les Butler.

method	site	C_q	η	C_q	η
		cc-pVDZ		cc-pVTZ	
RHF^a	Al$_1$	15.936	0.99	-18.210	0.99
RHF^a	Al$_2$	15.931	0.99	-18.222	0.99
RHF^b	Al	-15.979	0.99	17.809	0.94
RHF^c	Al	-17.257	0.90	-19.082	0.92
RHF^d	Al	-17.257	0.90		
B3LYP^a	Al$_1$	-14.343	0.92	17.733	0.94
B3LYP^a	Al$_2$	-14.349	0.92	17.725	0.95
B3LYP^b	Al	-15.191	0.83	17.977	0.93
B3LYP^c	Al	-16.398	0.79	-19.092	0.88

method	site	C_q	η
expt.	Al	±15.8	1

Table 10.3: ^{27}Al nuclear quadrupole coupling constants C_q in megahertz for the largest dimer, $[Al(NMe_2)_3]_2$ (diaminato aluminum), using RHF and B3LYP methods with cc-pVDZ and cc-pVTZ basis sets at [a] crystal structure coordinates[270] [b] optimized coordinates of D_{2h} symmetry, [c] optimized coordinates of C_{2h} symmetry, [d] fully optimized crystal structure coordinates of C_1 symmetry. Experimental values (marked 'expt.') are from NMR experiments by Anthony Mrse, Earl Emery, Pam Bryant and Les Butler.

method	site	C_q	η	C_q	η
		cc-pVDZ		cc-pVTZ	
RHF[a]	Al$_4$	12.286	0.72	14.400	0.76
RHF[a]	Al$_{17}$	12.287	0.72	14.400	0.76
RHF[b]	Al	15.660	0.21	18.655	0.19
RHF[c]	Al	11.894	0.75	14.163	0.76
RHF[d]	Al$_4$	11.876	0.75		
RHF[d]	Al$_{17}$	11.920	0.76		
B3LYP[a]	Al$_4$	10.117	0.83	13.330	0.73
B3LYP[a]	Al$_{17}$	10.118	0.83	13.331	0.73
B3LYP[b]	Al	14.447	0.24	18.144	0.16
B3LYP[c]	Al	9.774	0.86		

method	site	C_q	η
expt.	Al	±12.2	0.8

LAPW DFT as implemented in WIEN [113] with the generalized gradient approximation (GGA), $R_{mt} \times K_{max}=2.53$, $G_{max}=24$, k-points=1 and R_{mt} for Al=1.65, C=1.0, H=0.6 and N=1.4 yields $C_q=17.252, \eta=0.91$.

Third, we examine the larger of the two dimers, $[Al(NMe_2)_3]_2$, diaminato aluminum. The crystal structure is available [270]. We use single-molecule MO (cf. table 10.3) and full-crystal FP-LAPW DFT. Calculations on the full crystals of both dimethyl aluminum and diaminato aluminum require a new set of R_{mt} for Al=1.65, C=1.0, H= 0.6, N=1.4. They use GGA and $G_{max}=24$ with k-points=1. The $R_{mt} \times K_{max}$ differ because the unit cells are different sizes. For dimethyl aluminum with $R_{mt} \times K_{max}=2.00$ $C_q=15.875$ $\eta=0.82$ and diaminato aluminum with $R_{mt} \times K_{max}=2.28$ $C_q=12.115$ $\eta=0.79$.

Short C-H bonds dictate small atomic spheres and therefore an unusually small cut-off for the plane-wave basis set, $R_{mt} \times K_{max}$. With such small values of $R_{mt} \times K_{max}$ the FP-LAPW method for these molecules can not stand alone, however they are useful as a comparison for the single-molecule MO results.

The investigation of the two dimers, dimethyl and diaminato aluminum reveals several items:

1. full-crystal FP-LAPW method requires more CPU time and is severely limited by computer main memory size because of the short C-H bonds,

2. single-molecule MO and full-crystal FP-LAPW DFT results agree,

3. optimization of the structures is only practical with the single-molecule MO method,

4. the symmetry constrained optimization is faster because there are fewer unique atoms (cf. table 10.1) and it produces similar results to the crystal structure.

Bearing these items in mind we investigate the remaining MAO models with the single-molecule MO method using symmetry constrained optimization, RHF, cc-pVDZ and cc-pVTZ basis sets.

10.3   Results and Discussion

We report ^{27}Al NMR spectral parameters for MAO models using optimized geometries and RHF/cc-pVDZ and RHF/cc-pVTZ are in table 10.4. Some additional calculations including B3LYP are also in table 10.4.

Monoaluminum contrasts the other models with an η of zero, because of the centrosymmetric environment in which the Al is in. For dimethyl aluminum calculations with both the C_{2h} and D_{2h} structures B3LYP increases the magnitude of C_q. This is in contrast to all other optimized structure calcula-

Table 10.4: MAO models ^{27}Al quadrupole coupling constant, C_q, in megahertz and asymmetry parameter, η calculated from optimized geometries using Restricted Hartree-Fock (RHF) and Becke's 3 Parameter Lee-Yang-Parr (B3LYP) with correlation consistent polarized double (cc-pVDZ) and triple (cc-pVTZ) basis sets. ^{a} Structures correspond to a truncated version of the actual molecule, i.e. Me is substituted for C_6H_5 in the hexa aluminum, $-2,6-i\text{Pr}_2C_6H_3$ in the tri aluminum and $-2,6-i\text{Pr}_2C_6H_3$ in the tetra aluminum. Experimental values (marked 'expt.') are from NMR experiments by Anthony Mrse, Earl Emery, Pam Bryant and Les Butler.

molecule	site	RHF cc-pVDZ		cc-pVTZ		expt.	
		C_q	η	C_q	η	C_q	η
mono aluminum	Al$_4$	27.119	0.00	36.067	0.00		
dimethyl aluminum	Al$_1$	-17.257	0.90	-19.082	0.92	15.8	1
diaminato aluminum	Al$_8$	11.894	0.75	14.163	0.76	12.2	0.8
tri aluminum^a	Al$_9$	30.802	0.06	39.950	0.01	37	0
hexa aluminum^a	Al$_6$	-13.181	0.93	14.545	0.99		
hexa aluminum	Al$_6$	-16.537	0.59	-18.214	0.62	17.5	0.55
tetra aluminum^a	Al$_1$	1.207	0.00	0.293	0.00	1.8	0.00
tetra aluminum^a	Al$_4$	11.511	0.04	14.159	0.11	12.5	0.12
				B3LYP			
mono aluminum	Al$_4$	20.145	0.00	31.350	0.00		
dimethyl aluminum	Al$_1$	-16.398	0.79	-19.092	0.88		
diaminato aluminum	Al$_8$	9.774	0.86				
tri aluminum^a	Al$_9$	25.269	0.08	37.021	0.02		
hexa aluminum^a	Al$_6$	-11.635	0.86				
hexa aluminum	Al$_6$	-14.840	0.52				

tions for the MAO models. For diaminato aluminum the choice of symmetry point group for the optimized calculations plays an interesting role. With D_{2h} the value of C_q is higher and the value of η is remarkably different (≈ 0.2 vs. ≈ 0.8) in comparison to the C_{2h} structure. This is also in contrast to the very similar dimethyl aluminum structure. We truncate many structures out of necessity; without truncation the calculation might not be possible with current computational resources. Nevertheless, the effect of this truncation should be examined when possible. Truncation plays a large role in determining the value of η (≈ 1 vs ≈ 0.6) for the truncated versus non-truncated versions of hexa aluminum. However, there is very little difference for the truncated and non-truncated versions of tri aluminum.

The accuracy of calculations, with regard to experiment, is $\approx \pm 2MHz$ for C_q and $\approx \pm 0.2$ for η. The magnitudes of C_q and values for η match well for dimethyl aluminum, diaminato aluminum, tri aluminum, tetra aluminum and hexa aluminum, though the ratio of C_q values for tetra aluminum with cc-pVTZ (≈ 7 expt. vs. ≈ 48) is not good at all. Surprisingly, the results from cc-pVDZ are better (≈ 7 expt. vs. ≈ 10). Perhaps, additional correlation with B3LYP will improve the ratio.

10.4 Conclusion

Application of the single-molecule MO method, aided by the speed of truncation and symmetry constraints for geometry optimizations, yields good qualitative agreement with experiment. Truncation and symmetry constraints can both dramatically effect ^{27}Al NMR spectral parameters. The combination of calculation with experiment works to confirm the unusually high C_q values of tri aluminum.

CHAPTER 11

CONCLUSIONS

Full-crystal FP-LAPW DFT was explored with calculations on corundum and then applied to accurately predict EFGs for andalusite. Also using the full-crystal FP-LAPW method, the EFG temperature dependence due to structure was examined for three Al_2SiO_5 polymorphs: andalusite, silliman-ite, and kyanite. The embedded-cluster MO method as implemented was not accurate enough to reliably predict tensor orientations in andalusite, though C_q magnitudes were reasonable. Work could be applied to self-consistently determine the charges on the point charges, possibly increasing the ability of the cluster to mimic a crystal[274, 275, 81]. We demonstrated the single-molecule MO approach with the diatomic aluminum halides and then applied it with reasonable success to predicting [81]Br NQR frequencies of flame retar-dants and models. The single-molecule MO approach was not as successful for predicting ^{14}N NQR frequencies of tetryl and similar compounds with ni-tro groups. These could be further investigated with the single-molecule MO method by unconstrained geometry optimization of single molecules from crystal structures and additional methods for the inclusion of correlation or even with the full-crystal FP-LAPW method. The most exciting project was the application of the single-molecule MO and full-crystal FP-LAPW meth-

ods to explore relationships between spectra and possible structures for other Al containing structures similar to methyl aluminum oxide (MAO). MAO is a co-catalyst in new-generation Ziegler-Natta catalysts for olefin polymerization [262, 263, 264] and NQR is well-suited as a tool for study due to the large quadrupolar interactions at the ^{27}Al sites. The $[\mathrm{Me\,Al}\{N-2, 6-i\mathrm{Pr}_2\mathrm{C}_6\mathrm{H}_3)\}]_3$ structure may very well be a world record value of C_q.

The study of EFG calculations themselves has been interesting and has improved the calculations, however it was the practical applications which added the most value. The combination of EFG calculations and data from NMR experiments to zeolites, flame retardants, explosives and MAO provided a valuable tool. This tool can be used to identify key chemical structures, to improve products such as flame retardant HIPS, and to increase efficiency of processes such as production of polypropylene and other olefins.

BIBLIOGRAPHY

[1] Lucken, E. A. C. *Nuclear Quadrupole Coupling Constants*, Academic Press: New York, 1969.

[2] Friebolin, H. *Basic One- and Two-Dimensional NMR Spectroscopy*, VCH: New York, 1993.

[3] Lindgren, B. *Phys. Rev. B.*, **1986**, *34*, 648.

[4] Uhlmann, J. G.; Oelberg, J. D.; Sikkemma, K. D., and Nelb, R. G. *Plast Compd.*, **1993**, *May/June*, 38.

[5] Seinfeld, J. H. and Pandis, S. N. *Atmospheric Chemistry and Physics: From Air Pollution to Climate Change*, Wiley: New York, 1998.

[6] Quantum Magnetics, Inc.; http://www.qm.com; 7740 Kenamar Court; San Diego, CA 921211.

[7] Storck, W. J.; Layman, P. L.; McCoy, M.; Reisch, M. S.; Thayer, A. M., and Tremblay, J.-F. *Chemical and Engineering News*, June 28 **1999**, *77*, 33.

[8] Casimir, H. B. G. *On the Interaction Between Atomic Nuclei and Electrons*, Freeman: Cambridge, 1963.

[9] Kopfermann, H. *Nuclear Moments*, Academic Press: New York, 1958.

[10] Lucken, E. A. C. *Z. Naturforsch.*, **1993**, *49a*, 133.

[11] Das, T. P. *Nuclear Quadrupole Resonance Spectroscopy*, Academic Press: New York, 1958.

[12] Kaufmann, E. N. and Vianden, R. J. *Rev. Modern Physics*, **1979**, *51*, 161.

[13] Das, T. P. and Schmidt, P. C. *Z. Naturforsch.*, **1986**, *41a*, 47.

[14] Vianden, R. *Hyperfine Interactions*, **1983**, *15/16*, 189.

[15] Smith, M. E. and Van Eck, E. R. H. *Prog. Nucl. Magn. Reson. Spectrosc.*, **1999**, *34*, 159.

[16] Kuhn, H. G. *Atomic Spectra*, Academic Press: New York, 1962.

[17] Ramsey, N. *Molecular Beams*, Clarendon Press: Oxford, 1956.

[18] Scoles, G. *Atomic and Molecular Beam Methods*, Oxford University Press: New York, 1988.

[19] Gordy, W. *Microwave Spectroscopy*, Wiley & Sons: New York, 1953.

[20] Strandberg, M. W. P. *Microwave Spectroscopy*, Wiley & Sons: New York, 1954.

[21] Townes, C. H. *Microwave Spectroscopy*, McGraw-Hill: New York, 1955.

[22] Maverick, A. W.; Butler, L. G.; Lewis, W.; Gallegos, C. H.; Goette, J. D.; Rickel, D. G., and Fowler, C. M. *Inorg. Chim. Acta,* **1996**, *243*, 309.

[23] Maverick, A. W. and Butler, L. G. *Intern. J. Quantum Chemistry,* **1997**, *64*, 607.

[24] Butler, L. G.; Maverick, A. W.; Gallegos, C. H.; Goettee, J. D.; Marshall, B. R.; Fowler, C. M.; Rickel, D. G.; Gonzales, J. M., and Tabaka, L. J. *Intern. J. Quantum Chemistry*, **1998**, *70*, 797.

[25] Pauli, W. Zurich conference. In *Zurich Conference*, 1931.

[26] Racah, G. *Zeits. f. Physik,* **1931**, *71*, 431.

[27] Schuler, H. and Schmidt, T. *Z. Phys.*, **1935**, *94*, 457.

[28] Kellog, J. M. B.; Rabi, I. J.; Ramsey, N. F., and Zacharias, J. R. *Phys. Rev.*, **1939**, *55*, 318.

[29] Kellog, J. M. B.; Rabi, I. J.; Ramsey, N. F., and Zacharias, J. R. *Phys. Rev.*, **1940**, *57*, 677.

[30] Nordsieck, A. *Phys Rev.*, **1940**, *57*, 556.

[31] Nordsieck, A. *Phys Rev.*, **1940**, *58*, 310.

[32] Newell, G. F. *Phys. Rev.*, **1950**, *78*, 711.

[33] Townes, C. H. and Dailey, B. P. *J. Chem. Phys.*, **1949**, *17*, 782.

[34] Butler, L. G. private communication.

[35] Dehmelt, H. G. *Naturwiss.*, **1950**, *37*, 398.

[36] Robinson, H.; Dehmelt, H. G., and Gordy, W. *J. Chem. Phys.*, **1954**, *22*, 511.

[37] Blaha, P. and Schwarz, K. *Hyperfine Interactions*, **1989**, *52*, 153.

[38] Amatao, I. *Science*, **1998**, *282*, 611.

[39] Roothaan, C. C. J. *Rev. Mod. Phys.*, **1951**, *23*, 69.

[40] Roothaan, C. C. J. *Rev. Mod. Phys.*, **1960**, *32*, 179.

[41] Frisch, M. J.; Trucks, G. W.; Schlegel, H. B.; Gill, P. M. W.; Johnson, B. G.; Wong, M. W.; Foresman, J. B.; Robb, M. A.; Head-Gordon, M.; Replogle, E. S.; Gomperts, R.; Andres, J. L.; Raghavachari, K.; Binkley, J. S.; Gonzalez, C.; Martin, R. L.; Fox, D. J.; Defrees, D. J.; Baker, J.; Stewart, J. J. P.; , and Pople, J. A. Gaussian 92/DFT, Revision F.4. Gaussian, Inc., Pittsburgh PA, 1993.

[42] Kestner, N. R. private communication.

[43] Schmidt, M. W.; Baldridge, K. K.; Boatz, J. A.; Elbert, S. T.; Gordon, M. S.; Jensen, J. H.; Koseki, S.; Matsunaga, N.; Nguyen, K. A.; Su, S. J.; Windus, T. L.; Dupuis, M., and Montgomery, J. A. GAMESS version = 31 Oct 1996, from Iowa State University., 1993.

[44] Johnson, B. G.; Gill, P. M. W., and Pople, J. A. *J. Chem. Phys.*, **1993**, *98*, 5612.

[45] Hohenberg, P. and Kohn, W. *Phys. Rev.*, **1964**, *136*, B864.

[46] Kohn, W. and Sham, L. J. *Phys. Rev.*, **1965**, *A140*, A1133.

[47] Bagano, A. *J. Mol. Structure (Theochem)*, **1997**, *418*, 243.

[48] Bacskay, G. B.; Kerdraon, D. I., and Hush, N. S. *Chem. Phys.*, **1990**, *144*, 53.

[49] Camus, S.; Harris, K. D. M., and Johnston, R. L. *Chem. Phys. Lett.*, **1997**, *276*, 186.

[50] Butler, L. G. and Brown, T. L. *J. Am. Chem. Soc.*, **1981**, *103*, 6541.

[51] Cummins, P. L.; Bacskay, G. B., and Hush, N. S. *Chem. Phys.*, **1987**, *115*, 325.

[52] Cummins, P. L.; Bacskay, G. B., and Hush, N. S. *Mol. Phys.*, **1987**, *62*, 193.

[53] Gready, J. E. and Bacskay, N. S., Hush. *Chem. Phys.*, **1982**, *64*, 1.

[54] Gready, J. E. *Chem. Phys.*, **1981**, *55*, 1.

[55] Palmer, M. H. *Z. Naturforsch.*, **1996**, *51a*, 479.

[56] Palmer, M. H. and Blair-Fish, J. A. *Z. Naturforsch.*, **1994**, *49a*, 146.

[57] Wu, G.; Hook, A.; Dong, S., and Yamada, K. *J. Phys. Chem. A*, **2000**, *104*, 4102.

[58] Wu, G.; Yamada, K.; Dong, S.; , and Grondey, H. *J. Am. Chem. Soc.*, **2000**, *122*, 4215.

[59] Arnold, W. D.; Sanders, L. K.; McMahon, M. T.; Volkov, A. V.; Wu, G.; Coppens, P.; Wilson, S. R.; Godbout, N.; , and Oldfield*, E. *J. Am. Chem. Soc.*, **2000**, *ASAP*, .

[60] Diercksen, G. H.; Sadlej, A. J.; Sundholm, D., and Pyykkö, P. *Chem. Phys. Lett.*, **1988**, *143*, 163.

[61] Diercksen, G. H. F. and Sadlej, A. J. *Chem. Phys. Lett.*, **1989**, *155*, 127.

[62] Cernusak, I.; Diercksen, G. H., and Sadlej, A. J. *Chem. Phys.*, **1986**, *108*, 45.

[63] Pati, R.; Srinvas, S.; Briere, T.; Sahoo, T. P. D. N.; , and Ray, S. N. *J. Phys. Chem.*, **1995**, *99*, 9051.

[64] Cummins, P. L.; Backsay, G. B., and Hush, N. S. *J. Chem. Phys*, **1987**, *87*, 416.

[65] Pyykkö, P. *Z. Naturforsch.*, **1992**, *47a*, 189.

[66] Scuseria, G. E. and III, S. H. F. *J. Chem. Phys.*, **1987**, *87*, 4021.

[67] Sundholm, D.; Pyykkö, P.; Laaksonen, L., and Sadlej, A. J. *Chem. Phys. Lett.*, **1984**, *112*, 1.

[68] Sundholm, D.; Pyykkö, P.; Laaksonen, L., and Sadlej, A. J. *Chem. Phys.*, **1986**, *101*, 219.

[69] Sundholm, D. and Olsen, J. *Phys. Rev. A.*, **1990**, *42*, 1160.

[70] Clotet, A.; Ricart, J. M.; Sousa, C., and Illas, F. *J. Electron. Spectrosc. Relat. Phenom.*, **1994**, *69*, 65.

[71] Sousa, C.; Illas, F., and Pacchioni, G. *J. Chem. Phys.*, **1993**, *99*, 6818.

[72] Gready, J. E. *J. Chem. Phys.*, **1984**, *88*, 3497.

[73] Huber, H. *J. Chem. Phys.*, **1985**, *83*, 4591.

[74] Köster, A. M.; Calaminici, P., and Russo, N. *Phys. Rev. A.*, **1996**, *53*, 3865.

[75] Lindgren, B. *Phys. Rev. B: Condens. Matter*, **1986**, *34*, 648.

[76] Lindgren, B. *Europhysics Letters*, **1990**, *11*, 555.

[77] Schwarz, K.; Ambrosch-Draxl, C., and Blaha, P. *Phys. Rev. B: Condens. Matter*, **1990**, *42*, 2051.

[78] Ambrosch-Draxl, C.; Blaha, P., and Schwartz, K. *Phys. Rev. B.*, **1991**, *44*, 5141.

[79] Karzel, H.; Potzel, W.; Kofferlein, M.; Schiessl, W.; Steiner, M.; Hiller, U.; Kalvius, G. M.; Mitchell, D. W.; Das, T. P.; Blaha, P.; Schwarz, K., and Pasternak, M. P. *Phys. Rev. B.*, **1996**, *53*, 11425.

[80] Guenzburger, D. and Ellis, D. E. *Phys. Rev. B*, **1987**, *36*, 6971.

[81] Mitchell, D. W.; Das, T. P.; Potzel, W.; Schiessl, W.; Harzel, H.; Steiner, M.; Kfferlein, M.; Hiller, U.; Kalvius, G. M.; Martin, A.; Schafer, W.; Will, G.; Halevy, I., and Gal. *J. Phys. Rev. B.*, **1996**, *53*, 7684.

[82] Mitchell, D. W.; Sulaiman, S. B.; Sahoo, N.; Das, T. P.; Potzel, W., and Kalvius, G. M. *Phys. Rev. B: Condens. Matter*, **1991**, *44*, 6728.

[83] S., M. D.; Das, T. P.; W., P.; Kalvius, G. M.; Schiessl, W.; Steiner, M., and Köfferlein, M. *Phys. Rev. B*, **1993**, *48*, 16449.

[84] Nogueira, S. R.; Vugman, N. V., and Guenzburger, D. *Hyperfine Interactions*, **1990**, *60*, 631.

[85] Bryce, D. L. and Wasylishen, R. E. *J. Phys. Chem. A*, **1999**, *103*, 7364.

[86] Tröger, W.; Butz, T.; Blaha, P., and Schwartz, K. *Hyperfine Interactions*, **1993**, *80*, 1109.

[87] Palmer, M. H. *Z. Naturforsch.*, **1992**, *47a*, 203.

[88] Terra, J. and Guenzburger, D. *Phys. Rev. B*, **1991**, *44*, 8584.

[89] Palmer, M. H. and Blair-Fish, J. A. *Z. Naturforsch.*, **1994**, *49a*, 137.

[90] Palmer, M. H. and Sherwood, P. *Z. Naturforsch.*, **1996**, *51a*, 460.

[91] Palmer, M. H. *Z. Naturforsch.*, **1996**, *51a*, 451.

[92] Palmer, M. H.; Blake, A. J.; Khurshid, M. M. P., and Smith, A. S. *Chem. Phys.*, **1992**, *168*, 41.

[93] Pati, R.; Srinivas, S.; Briere, T.; Das, T.; Sahoo, N., and Ray, S. *J. Phys. Chem.*, **1995**, *99*, 9051.

[94] Rizzo, A.; Ruud, K.; Helgaker, T., and M., J. *J. Chem. Phys.*, **1998**, *109*, 2264.

[95] Bishop, D. M. and Cybulski, S. M. *J. Chem. Phys.*, **1994**, *100*, 6628.

[96] Bishop, D. M. and Cybulski, S. M. *J. Chem. Phys.*, **1994**, *101*, 2180.

[97] Butler, L. G. and Keiter, E. A. *J. Coord. Chem.*, **1994**, *32*, 121.

[98] Barysz, M. and Sadlej, A. J. *Theor. Chim. Acta*, **1997**, *97*, 260.

[99] Pyykkö, P. and Seth, M. *Theor. Chim. Acta*, **1997**, *96*, 92.

[100] Kello, V. and Sadlej, A. J. *J. Chem. Phys.*, **2000**, *112*, 522.

[101] Halkier, A.; Christansen, O.; Sundholm, D., and Pyykkö, P. *Chem. Phys. Lett.*, **1997**, *271*, 273.

[102] Pernpointner, M.; Schwerdtfeger, P., and Hess, B. A. *Int. J. Quantum Chem.*, **2000**, *76*, 371.

[103] Kellö, V.; Sadlej, A.; Pyykkö, P.; Sundholm, D., and Tokman, M. *Chem. Phys. Lett.*, **1999**, *304*, 414.

[104] Halkier, A.; Koch, H.; Christiansen, O.; Jörgensen, P., and Helgaker, T. *J. Chem. Phys.*, **1997**, *107*, 849.

[105] Foresman, J. B. and Frisch, Æ. *Exploring Chemistry with Electronic Structure Methods*, Gaussian, Inc.: Pittsburg, PA, 1996.

[106] Becke, A. D. *J. Chem. Phys.*, **1993**, *98*, 5648.

[107] Lee, C.; Yang, W., and Parr, R. G. *Phys. Rev. B: Condens. Matter*, **1988**, *37*, 785.

[108] Becke, A. D. *Phys. Rev. A.*, **1988**, *38*, 3098.

[109] Becke, A. D. Density Functional Theories in Quantum Chemistry: Beyond the Local Density Approximation. In *The Challenge of d and f Electrons: Theory and Computation*, chapter 12, 165. American Chemical Society, Washington, DC, December 1988.

[110] Miehlich, B.; Savin, A.; Stoll, H., and Preuss, H. *Chem. Phys. Lett.*, **1989**, *157*, 200.

[111] Becke, A. D. *J. Chem. Phys.*, **1993**, *98*, 1372.

[112] Vosko, S. H.; Wilk, L., and Nusair, M. *Can. J. Phys.*, **1980**, *58*, 1200.

[113] WIEN97.7, P. Blaha, K. Schwarz, and J. Luitz, WIEN97, Vienna University of Technology 1997. (Improved and updated Unix version of the original copyrighted WIEN-code, which was published by P. Blaha, K. Schwarz, P. Sorantin, and S. B. Trickey, in *Comput. Phys. Commun.* 1990, *59*, 399-415.

[114] Singh, D. *Plane waves, pseudopotentials and the LAPW method*, Kluwer Academic Publishers: Boston, 1994.

[115] Perdew, J. P. and Wang, Y. *Phys. Rev.*, **1992**, *B45*, 13244.

[116] Perdew, J. P.; Burke, K., and Ernzerhof, M. *Phys. Rev. Lett.*, **1996**, *77*, 3865.

[117] Winkler, B.; Blaha, P., and Schwarz, K. *Am. Mineral.*, **1996**, *81*, 545.

[118] Dufek, P.; Blaha, P., and Schwartz, K. *Phys. Rev. Lett.*, **1995**, *75*, 3545.

[119] Lucken, E. A. C. *Nuclear Quadrupole Coupling Constants*, Academic Press: New York, 1969.

[120] Slichter, C. P. *Principles of Magnetic Resonance*, Harper & Row: New York, 1963.

[121] Halliday, D. and Resnik, R. *Physics*, Wiley & Sons: New York, 1963.

[122] Tokman, M.; Sundholm, D.; Pyykkö, P., and Olsen, J. *Chem. Phys. Lett.*, **1997**, *265*, 60.

[123] SPARTAN: Deppmeier, B. J.; Dreissen, A. J.; Hehre, W. J.; Johnson, J. A.; Johnson, C. H.; Leonard, M. J.; Lou, L.; Peng, C; Yu, J.; Spartan IBM VERSION 4.1.1 X11 AIX3.2.5, Copyright 1981-1986, Wavefunction, Inc.

[124] Schlegel, H. B. *J. Comput. Chem.*, **1982**, *3*, 214.

[125] Jensen, F. *J. Chem. Phys.*, **1995**, *102*, 6706.

[126] Hedin, L. and Lundqvist, B. I. *J. Phys. C: Solid State Physics*, **1971**, *4*, 2064.

[127] Hedin, L. and Lundqvist, B. I. *J. Physique Col.*, **1972**, *33*, C3.

[128] Morruzzi, V. L.; Janak, J., and Williams, A. R. C. E. P. o. M., Pergamon Press: New York, 1978.

[129] Soldner, T.; Tröger, W.; Butz, T.; Blaha, P., and Schwartz, K. *Z. Naturforsch.*, **1998**, *53a*, 411.

[130] Wyse, F. C. and Gordy, W. *J. Chem. Phys.*, **1972**, *56*, 2130.

[131] Lide, D. R., Jr. *J. Chem. Phys.*, **1965**, *42*, 1013.

[132] Hensen, K. D.; Styger, C.; Jäger, W.; Merer, J. A., and Gerry, M. C. *J. Chem. Phys.*, **1993**, *5*, 3320.

[133] Gustev, G. L.; Jena, P., and Bartlett, R. J. *J. Chem. Phys.*, **1999**, *110*, 2928.

[134] Basis sets were obtained from the Extensible Computational Chemistry Environment Basis Set Database, Version , as developed and distributed by the Molecular Science Computing Facility, Environmental and Molecular Sciences Laboratory which is part of the Pacific Northwest Laboratory, P.O. Box 999, Richland, Washington 99352, USA, and funded by the U.S. Department of Energy. The Pacific Northwest Laboratory is a multi-program laboratory operated by Battelle Memorial Institue for the U.S. Department of Energy under contract DE-AC06-76RLO 1830. Contact David Feller or Karen Schuchardt for further information. http://www.emsl.pnl.gov:2080/forms/basisform.html.

[135] Hehre, W. J.; Radom, L.; Schleyer, P. v., and Pople, J. A. *Ab Initio Molecular Orbital Theory*, Wiley and Sons: New York, 1986.

[136] Brown, A. S.; Spackman, M. A., and Hill, R. J. *Acta. Cryst.*, **1993**, *A49*, 513.

[137] Lewis, J.; Schwarzenbach, D., and Flack, H. D. *Acta Cryst.*, **1982**, *38*, 33.

[138] Megaw, H. *Crystal Structures: A Working Approach*, W. B. Saunders Co.: Philadelphia, Pa, 1973.

[139] Brun, E.; Derighetti, B.; Hundt, E. E., and Niebuhr, H. H. *Phys Lett.*, **1970**, *31A*, 416.

[140] Pound, R. V. *Phys. Rev.*, **1950**, *79*, 685.

[141] Chang, J.; Connor, C.; Hahn, E. L.; Huber, H., and Pines, A. *J. Magn. Reson.*, **1989**, *82*, 387.

[142] Connor, C.; Chang, J., and Pines, A. *J. Chem. Phys.*, **1990**, *93*, 7639.

[143] Silver, A. H.; Kushida, T., and Lambe, J. *Phys. Rev.*, **1962**, *125*, 1147.

[144] Huggins, B. A. and Ellis, P. D. *J. Am. Chem. Soc.*, **1992**, *114*, 2098.

[145] Vosegaard, T. and Jakobsen, H. J. *J. Magn. Reson.*, **1997**, *128*, 135.

[146] Brown, A. S. and Spackman, M. A. *J. Phys. Chem.*, **1992**, *96*, 9200.

[147] Nagel, S. *J. Phys. C*, **1985**, *18*, 3673.

[148] Salasco, L.; Dovesi, R.; Orlando, R., and Causa, M. *Molecular Physics*, **1991**, *72*, 267.

[149] Vorotilova, L. S.; Shchegolev, B. F., and Dmitrieva, L. V. *Sov. Phys. Solid State*, **1991**, *33*, 861.

[150] Hafner, S. and Raymond, M. *J. Chem. Phys.*, **1968**, *49*, 3570.

[151] Casanovas, J.; Lorda, A.; Sousa, C., and Illas, F. *Inter. J. Quantum Chem.*, **1994**, *52*, 281.

[152] Salasco, L.; Dovesi, R.; Orlando, R., and Causa, M. *Molecular Physics*, **1991**, *72*, 267.

[153] Kirfel, A. and Eichhorn, K. *Acta Cryst.A*, **1990**, *46*, 271.

[154] Gravina, S. J. and Bray, P. J. *J. Magn. Reson.*, **1990**, *89*, 515.

[155] Nagel, S. *J. Phys. C*, **1985**, *18*, 3673.

[156] Bryant, P. L.; Harwell, C. R.; Wu, K.; Fronczek, F. R.; Hall, R. W., and Butler, L. G. *J. Phys. Chem. A*, **1999**, *103*, 5246.

[157] Sugano, S. and Shulman, R. G. *Phys. Rev. B.*, **1963**, *130*, 517.

[158] Lewandowski, A. C. and Wilson, T. M. *J. Comput. Phys.*, **1996**, *129*, 233.

[159] Hemmingsen, L. and Ryde, U. *J. Chem. Phys.*, **1996**, *100*, 4803.

[160] Palmer, M. H. *Z. Naturforsch. A: Phys. Sci.*, **1996**, *51*, 442.

[161] Blaha, P.; Schwarz, K., and Herzig, P. *Phys. Rev. Lett.*, **1985**, *54*, 1192.

[162] Blaha, P.; Singh, D. J.; Sorantin, P. I., and Schwarz, K. *Phys. Rev. B*, **1992**, *46*, 1321.

[163] Wei, S.-H. and Zunger, A. *J. Chem. Phys.*, **1997**, *107*, 1931.

[164] Palmer, M. H. and Blair-Fish, J. A. *Z. Naturforsch*, **1994**, *49a*, 137.

[165] Tossell, J. A. *Am. Min.*, **1993**, *78*, 16.

[166] Koller, H.; Meijer, E. L., and Santen, R. A. v. *Solid State NMR*, **1997**, *9*, 165.

[167] Schurko, R. W.; Wasylishen, R. E., and Phillips, A. D. *J. Magn. Reson.*, **1998**, *133*, 388.

[168] Cummins, P. L.; Bacskay, G. B., and Hush, N. S. *Chem. Phys.*, **1987**, *115*, 325.

[169] Dunning, T. H. J. and Hay, P. J. *Gaussian Basis Sets for Molecular Calculations*, 1. Plenum Press, New York, 1977.

[170] Wilson, S. *Basis Sets In Ab Initio Methods in Quantum Chemistry*, chapter 1. Wiley and Sons, New York, 1987.

[171] Dunning, T. H., Jr. *J. Chem. Phys.*, **1989**, *90*, 1007.

[172] Woon, D. E. and Dunning, T. H., Jr. *J. Chem. Phys.*, **1993**, *98*, 1358.

[173] Hafner, S. and Raymond, M. *Am. Min.*, **1967**, *52*, 1632.

[174] Raymond, M. *Phys. Rev. B.*, **1971**, *3*, 3692.

[175] Das, T. P. *Nuclear Quadrupole Resonance Spectroscopy*, Academic Press: New York, 1958.

[176] Mrse, A. A.; Lee, Y.; Bryant, P. L.; Fronczek, F. R.; Butler, L. G., and Simeral, L. S. *Chem. Mat.*, **1998**, *10*, 1291.

[177] Ashenhurst, J.; Wu, G., and Wang, S. *J. Am. Chem. Soc.*, **2000**, *122*, 2541.

[178] Cerny, Z.; Machacek, J.; Fusek, J.; Hermanek, S.; Kriz, O., and Casensky, B. *J. Organomet. Chem.*, **1991**, *402*, 139.

[179] Kriz, O.; Casensky, B.; Lycka, A.; Fusek, J., and Hermanek, S. *J. Magn. Reson.*, **1984**, *60*, 375.

[180] Simeral, L. S.; Zens, T., and Finnegan. *J. Appl. Spectrosc.*, **1993**, *47*, 1954.

[181] Mason, M. R.; Smith, J. M.; Bott, S. G., and Barron, A. R. *J. Am. Chem. Soc.*, **1993**, *115*, 4971.

[182] Nekhaeva, L. A.; Bondarenko, G. N.; Rykov, S. V.; Nekhaev, A. I.; Krentsel, B. A.; Marin, V. P.; Vyshinskaya, L. I.; Khrapova, I. M.; Polonskii, A. V., and Korneev, N. N. *J. Organomet. Chem.*, **1991**, *406*, 139.

[183] Benn, R.; Rufinska, A.; Janssen, E., and Lehmkuhl, H. *Organometallics*, **1986**, *5*, 825.

[184] Sugano, T.; Matsubara, K.; Fujita, T., and Takahashi, T. *J. Mol. Catal.*, **1993**, *82*, 93.

[185] Kimura, Y.; Tanimoto, S.; Yamane, H., and Kitao, T. *Polyhedron*, **1990**, *9*, 371.

[186] Imhoff, D. W.; Simeral, L. S.; Sangokoya, S. A., and Peel, J. H. *Organometallics*, **1998**, *17*, 1941.

[187] Tritto, I.; Donetti, R.; Sacchi, M. C.; Locatelli, P., and Zannoni, G. *Macromolecules*, **1997**, *30*, 1247.

[188] Storre, J.; Schnitter, C.; Roesky, H. W.; Schmidt, H.-G.; Nolte-meyer, M.; Fleischer, R., and Stalke, D. *J. Am. Chem. Soc.*, **1997**, *119*, 7505.

[189] Wehmschulte, R. J. and Power, P. P. *J. Am. Chem. Soc.*, **1997**, *119*, 8387.

[190] Harwell, C. R.; Mrse, A. A.; Shelby, A. I.; Butler, L. G., and Hall, R. W. *J. Phys. Chem. A*, **1999**, *103*, 8088.

[191] Veigele, W. J. and Bevan, A. W., Jr. *J. Chem. Phys.*, **1963**, *38*, 1596.

[192] Skibsted, J. and Jakobsen, H. J. *J. Phys. Chem.*, **1999**, *103*, 7958.

[193] Ghose, S. and Tsang, T. *Am. Min.*, **1973**, *58*, 748.

[194] Weller, M. T.; Brenchley, M. E.; Apperley, D. C., and Davies, N. A. *Solid State Nucl. Mag. Reson.*, **1994**, *3*, 103.

[195] Engelhardt, G. and Veeman, W. *J. Chem. Soc., Chem. Commun.*, **1993**, 622.

[196] Robinson, K.; Gibbs, G. V., and Ribbe, P. H. *Science*, **1971**, *172*, 567.

[197] Xiao, Y. and Kirkpatrick, J. *J. Mater. Res.*, **1995**, *10*, 2586.

[198] Trepanier, R. J. and Whitehead, M. A. *J. Chem. Soc., Faraday Trans.*, **1992**, *88*, 183.

[199] Skinner, B. J.; Clark, S. P., Jr., and Appleman, D. E. *American Journal of Science*, **1961**, *259*, 651.

[200] Kerrick, D. M. The Al_2SiO_5 polymorphs. In Ribbe, P. H., ed., *Reviews in Mineralogy*, volume 22, 24. Mineralogical Society of American, Washington, DC, 1990.

[201] Griffen, D. T. The aluminum silicate polymorphs. In *The Systematic Crystal Chemistry of Silicates*, chapter 6, 237. Oxford University Press, New York, 1992.

[202] Holdaway, M. J. and Mukhopadhyay, B. *American Mineralogist*, **1993**, *78*, 298.

[203] Winter, J. K. and Ghose, S. *Am. Min.*, **1979**, *64*, 573.

[204] Rocha, J. *Chemical communications: chem comm*, November **1998**, 2489.

[205] Smith, M. E.; Jeager, C.; Schoenhofer, R., and Steuernagel, S. *Chem. Phys. Lett.*, March **1994**, *219*, 75.

[206] Stebbins, J. F. Triple-Quantum Two-Dimensional ^{27}Al Magic-Angle Spinning Nuclear Magnetic Resonance Spectroscopic Study of Aluminosilicate and Aluminate Crystals and Glasses. In Ahrens, T. J., ed., *Nuclear Magnetic Resonance Spectroscopy of Silicates and Oxides in Geochemistry and Geophysics*, 303. American Geophysical Union, Washington DC, 1995.

[207] Alemany, L. B.; Steuernagel, S.; Amoureux, J.-P.; Callender, R. L., and Barron, A. R. *Solid State Nucl. Mag.*, **1999**, *14*, 1.

[208] Iglesias, M.; Schwartz, K.; Blaha, P., and Baldomir, D. Electronic Structure and Electric Field Gradient Calculations of Al_2SiO_5 Polymorphs. Communicated in November 23, 1999 letter from Karlhein Schwartz detailing submission on October 18, 1999.

[209] Hafner, S. S.; Raymond, M., and Ghose, S. *J. Chem. Phys.*, **1970**, *52*, 6037.

[210] Raymond, M. and Hafner, S. S. *J. Chem. Phys.*, **1970**, *53*, 4110.

[211] Beri, A. C.; Lee, T.; Das, T. P., and Sternheimer, R. M. *Phys. Rev. B: Condens. Matter*, **1983**, *28*, 2335.

[212] Dios, A. C. d.; Pearson, J. G., and Oldfield, E. *Science*, **1993**, *260*, 1491.

[213] Vaara, J.; Ruud, K.; Vahtras, O.; Ågren, H., and Jokisaari, J. *J. Chem. Phys.*, **1998**, *109*, 1212.

[214] Vaara, J.; Lounila, J.; Ruud, K., and Helgaker, T. *J. Chem. Phys.*, **1998**, *109*, 8388.

[215] Kim, A. J.; Fronczek, F. R.; Butler, L. G.; Chen, S., and Keiter, E. A. *J. Am. Chem. Soc.*, **1991**, *113*, 9090.

[216] Schmidt-Rohr, K. and Spiess, H. W. *Multidimensional Solid-State NMR and Polymers*, Academic Press: New York, 1994.

[217] Pati, R.; Srinivas, S.; Briere, T.; Das, T. P.; Sahoo, N., and Ray, S. N. *J. Chem. Phys.*, **1995**, *99*, 9051.

[218] Vermillion, K. E.; Florian, P., and Grandinetti, P. J. *J. Chem. Phys.*, **1998**, *108*, 7274.

[219] Brinkman, D. *J. Mol. Structure*, **1995**, *345*, 167.

[220] Ainbiner, N. E.; Azhegonov, A. S.; Danilov, A. V., and K., S. N. *J. Mol. Structure*, **1995**, *345*, 105.

[221] Wolf, F.; Kline, D., and Story, H. S. *J. Chem. Phys.*, **1970**, *53*, 3538.

[222] Yamada, K.; Kinoshita, M.; Hosokawa, K., and Okuda, T. *Bull. Chem. Soc. Jpn.*, **1993**, *66*, 1317.

[223] Pang, L.; Lucken, E. A. C., and Bernardinelli, G. *J. Am. Chem. Soc.*, **1990**, *112*, 8754.

[224] Mrse, A. A.; Lee, Y.; Bryant, P. L.; Fronczek, F. R.; Butler, L. G., and Simeral, L. S. *Chem. Mater.*, **1998**, *10*, 1291. Equations 3 and 7 are in error in this reference. We have corrected them here.

[225] Bray, P. J. and Barnes, R. G. *J. Chem. Phys.*, **1954**, *22*, 2023.

[226] Streitwieser, A. J. and Heathcock, C. H. *Introduction to Organic Chemistry*, Macmillan Publishing: New York, 1976.

[227] Visscher, L.; Enevoldsen, T.; Saue, T., and Oddershede, J. *J. Chem. Phys.*, **1998**, *109*, 9677.

[228] Kellö, V. and Sadlej, A. J. *Int. J. Quantum Chem.*, **1998**, *68*, 159.

[229] Kellö, V. and Sadlej, A. J. *Mol. Phys.*, **1996**, *89*, 127.

[230] Fowler, P. W.; Legon, A. C.; Peebles, S. A., and Steiner, E. *Chem. Phys. Lett.*, **1995**, *238*, 163.

[231] Schwarz, K. and Blaha, P. *Z. Naturforsch.*, **1992**, *47a*, 197.

[232] Bominaar, E. L.; Guillin, J.; Sawaryn, A., and Trautwein, A. X. *Phys. Rev. B: Condens. Matter*, **1989**, *39*, 72.

[233] Bacskay, G. B. *Chem. Phys. Lett.*, **1989**, *157*, 115.

[234] Cremer, D. and Krüger, M. *J. Phys. Chem.*, **1992**, *96*, 3239.

[235] Bersohn, R. *J. Chem. Phys.*, **1962**, *36*, 3445.

[236] Rosenthal, E. and Dailey, B. P. *J. Chem. Phys.*, **1965**, *43*, 2093. We calculate the [81]Br transition frequency from the quadrupole coupling constant and asymmetry parameter reported within this reference.

[237] Kellö, V. and Sadlej, A. J. *Chem. Phys. Lett.*, **1990**, *174*, 641.

[238] Sadlej, A. J. *Theor. Chim. Acta*, **1991**, *81*, 45.

[239] Binning, R. C., Jr. and Curtiss, L. A. *J. Coord. Chem.*, **1990**, *11*, 1206.

[240] Schmidt, M. W.; Baldridge, K. K.; Boatz, J. A.; Elbert, S. T.; Gordon, M. S.; Jensen, J. H.; Koseki, S.; Matsunaga, N.; Nguyen, K. A.; Su, S. J.; Windus, T. L.; Dupuis, M., and Montgomery, J. A. *J. Comput. Chem.*, **1993**, *14*, 1347.

[241] Ditchfield, R.; Hehre, W., and Pople, J. *J. Chem. Phys.*, **1971**, *54*, 724.

[242] Dunning, T. H. J. *J. Chem. Phys.*, **1977**, *66*, 1382.

[243] Dunning, T. H., Jr. *J. Chem. Phys.*, **1971**, *55*, 716.

[244] Bray, P. J. *J. Chem. Phys.*, **1954**, *22*, 950.

[245] Kojima, S.; Tsukada, K.; Ogawa, S., and Shimauchi, A. *J. Chem. Phys.*, **1953**, *21*, 1415.

[246] Semin, G. K. J. *Struct. Chem. (Engl. Transl.)*, **1962**, *3*, 275.

[247] Cassabella, P. A.; Bray, P. J.; Segel, S. L., and Barnes, R. G. *J. Chem. Phys.*, **1956**, *25*, 1280.

[248] Legon, A. C. and Thorn, J. C. *Chem. Phys. Lett.*, **1993**, *215*, 554.

[249] Jones, G. and Gordy, W. *Phys. Rev.*, **1964**, *136*, A1229. $Q(^{81}Br)$, $Q(^{79}Br)$ ratio was used from Fowler et al. 1995.

[250] Pati, R.; Das, T. P.; Sahoo, N., and Ray, S. N. *J. Phys. Chem. A*, April **1998**, *102*, 3209.

[251] Pati, R.; Das, T. P.; Sahoo, N., and Ray, S. N. *J. Phys. Chem. A*, August **1997**, *101*, 6101.

[252] Pati, R.; Sahoo, N.; Das, T. P., and Ray, S. N. *J. Phys. Chem. A*, October **1997**, *101*, 8302.

[253] Marino, R. A. and Connors, R. F. *J. Mol. Structure*, **1983**, *111*, 323.

[254] Owens, F. J. *Mol. Cryst. Liq. Cryst.*, **1985**, *126*, 379.

[255] Karpowicz, R. J. and Brill, T. B. *J. Phys. Chem.*, **1983**, *87*, 2109.

[256] Bryden, J. H. *Acta Cryst.*, **1972**, *B28*, 1395.

[257] Choi, C. and Prince, E. *Acta Cryst.*, **1972**, *B28*, 2857.

[258] Choi, C. S. and Abel, J. E. *Acta Cryst.*, **1972**, *B28*, 193.

[259] Golovina, N. I.; Titkov, A. N.; Raevskii, A. V., and Atovmyan, L. O. *J. Solid State Chem.*, **1994**, *113*, 229.

[260] Cady, H. H. *Acta Cryst.*, **1967**, *23*, 601.

[261] Palmer, M. H. *Z. Naturforsch.*, **1990**, *45a*, 357.

[262] Brintzinger, H. H.; Fischer, D.; Mlhaupt, R.; Rieger, B., and Waymouth, R. M. *Agnew. Chem. Int. Ed. Engl.*, **1995**, *34*, 1143.

[263] Carlson, E. D.; Krejchi, M. T.; Shah, C. D.; Terakawa, T.; Waymouth, R. M., and Fuller, G. G. *Macromolecules*, **1998**, *31*, 5343.

[264] Carpentier, P. A.; Zhu, S.; Hamielec, A. E., and Brook, M. A. *Polymer*, **1998**, *39*, 6501.

[265] Tossell, J. A. *Inorg. Chem.*, **1998**, *37*, 2223.

[266] Xue, X. and Kanzaki, M. *J. Phys. Chem. B*, **1999**, *103*, 10816.

[267] Tossell, J. A. *J. Phys. Chem. A*, **1998**, *102*, 3368.

[268] Fusco, R.; Longa, L.; Masi, F., and Garbassi, F. *Macromolecules*, **1997**, *30*, 7673.

[269] McLaughlin, G. M.; Sim, G. A., and Smith, J. D. *J. C. S. Dalton*, **1972**, *2197*, .

[270] Waggoner, K. M.; Olmstead, M. M., and Power, P. P. *Polyhedron*, **1990**, *9*, 257.

[271] Waggoner, K. M.; Hope, H., and Power, P. P. *Angew. Chem., Int. Ed. Engl.*, **1988**, *27*, 1699.

[272] Al-Wassil, A.-A. I.; Hitchcock, P. B.; Sarisaban, S.; Smith, J. D., and Wilson, C. L. *J. Chem. Soc. Dalton Trans.*, **1985**, 1929.

[273] Folting, K.; Streib, W. E.; Caulton, K. G.; Poncelet, O., and Hubert-Pfalzgraf, L. G. *Polyhedron*, **1991**, *10*, 1639.

[274] Lewandowski, A. C. and Wilson, T. M. *Journal of Computational Physics.*, **1996**, *129*, 233.

[275] Stefanovich, E. V. and Truong, T. N. *J. Phys. Chem.*, **1998**, *102*, 3018.

APPENDIX A

TETRYL AND MIMICS: MAPPING TO CRYSTAL STRUCTURE SITE NOTATION

Table A.1: RDX site notation from published crystal structure[257], other calculations[63] and this work.

crystal	other[63]	this work (crystal)	position	this work (opt)
C(1)	1	1	ring	
C(2)	2	2	ring	
C(3)	3	3	ring	
N(1)	4	4	ring	4,5,6
N(2)	5	5	ring	4,5,6
N(3)	6	6	ring	4,5,6
N(4)	7	7	ring-NO_2	1,2,3
N(5)	8	8	ring-NO_2	1,2,3
N(6)	9	9	ring-NO_2	1,2,3
O(1)	10	10	ring-NO_2	
O(2)	11	11	ring-NO_2	
O(3)	12	12	ring-NO_2	
O(4)	13	13	ring-NO_2	
O(5)	14	14	ring-NO_2	
O(6)	15	15	ring-NO_2	
H(1)	16	16	ring-H_2	
H(2)	17	17	ring-H_2	
H(3)	18	18	ring-H_2	
H(4)	19	19	ring-H_2	
H(5)	20	20	ring-H_2	
H(6)	21	21	ring-H_2	

Table A.2: Mapping TNB site notation from crystal structure[258] to this work. Order of atoms is that from Cambridge Crystallographic Database Quest Software. Because there were two molecules in the unit cell only one molecule (molecule 2) was used. Also shown are optimized structures Nsite numbers. The approximate rotation of nitro groups in degrees is shown in parenthesis.

crystal	this work		position
	(crystal)	(optimized)	
1 C(1)			ring
2 C(10)	1		ring
3 C(11)	2		ring
4 C(12)	3		ring
5 C(2)			ring
6 C(3)			ring
7 C(4)			ring
8 C(6)			ring
9 C(7)			ring
10 C(8)	4		ring
11 C(9)	5		ring
12 C(10)	6		ring
13 H(1)			ring-H
14 H(2)			ring-H
15 H(3)			ring-H
16 H(4)	7		ring-H
17 H(5)	8		ring-H
18 H(6)	9		ring-H
19 N(1)	(3°)		ring-NO_2
20 N(2)	(28°)		ring-NO_2
21 N(3)	(8°)		ring-NO_2
22 N(4)	10 (10°)	1,2,3(0°)	ring-NO_2
23 N(5)	11 (10°)	1,2,3(0°)	ring-NO_2
24 N(6)	12 (5°)	1,2,3(0°)	ring-NO_2
25 O(1)			ring-NO_2
26 O(10)	13		ring-NO_2
27 O(11)	14		ring-NO_2
28 O(12)	15		ring-NO_2
29 O(2)			ring-NO_2
30 O(3)			ring-NO_2
31 O(4)			ring-NO_2
32 O(5)			ring-NO_2
33 O(6)			ring-NO_2
34 O(7)	16		ring-NO_2
35 O(8)	17		ring-NO_2
36 O(9)	18		ring-NO_2

Table A.3: Mapping TNX site notation from crystal structure[256] to this work. Order of atoms is that from Cambridge Crystallographic Database Quest Software. Also shown are optimized structures N site numbers. The approximate rotation of nitro groups in degrees is shown in parenthesis.

crystal	this work		position
	(crystal)	(optimized)	
C(1)	1		ring
C(2)	2		ring
C(3)	3		-CH$_3$
C(4)	4		ring
C(5)	5		ring
H(1)	6		-CH$_3$
H(2)	7		-CH$_3$
H(3)	8		-CH$_3$
H(4)	9		ring
N(1)	10 (35.7°)	8,9(30°)	-NO$_2$
N(2)	11 (75.2°)	12(75°)	b,-NO$_2$
O(1)	12		-NO$_2$
O(2)	13		-NO$_2$
O(3)	14		-NO$_2$
C(2F)	15		ring
C(1F)	16		ring
O(3F)	17		-NO$_2$
N(1F)	18 (35.7°)	8,9(30°)	-NO$_2$
C(3F)	19		-CH$_3$
O(1F)	20		-NO$_2$
O(2F)	21		-NO$_2$
H(1F)	22		-CH$_3$
H(2F)	23		-CH$_3$
H(3F)	24		-CH$_3$

Table A.4: Mapping monoclinic (TNT-m) and orthorhombic (TNT-o) trinitrotoluene site notation from crystal structure[259] to this work. Order of atoms is that from Cambridge Crystallographic Database Quest Software. Because there were two molecules in the unit cell only one molecule (molecule 1) was used for both orthorhombic and monoclinic. Also shown are optimized structures N site numbers. The approximate rotation of nitro groups in degrees is shown in parenthesis.

crys.	#	t.w. TNT-m crys.	opt.	pos.	t.w. TNT-o crys.	opt.	pos.
O7	7	1		ring-NO_2	4		ring-NO_2
O8	8	2		ring-NO_2	5		ring-NO_2
O9	9	3		ring-NO_2	3		ring-NO_2
O10	10	4		ring-NO_2	2		ring-NO_2
O11	11	5		ring-NO_2	1		ring-NO_2
O12	12	6		ring-NO_2	6		ring-NO_2
N4	16	7($40°$)	8,9($35°$)	ring-NO_2	9($33°$)	12	p,ring-NO_2
N5	17	8($33°$)	12 ($0°$)	p,ring-NO_2	7($40°$)	8,9	ring-NO_2
N6	18	9($60°$)	8,9($35°$)	ring-NO_2	8($55°$)	8,9	ring-NO_2
C8	26	10		ring	15		ring-CH_3
C9	27	11		ring	16		ring
C10	28	12		ring	18		ring
C11	29	13		ring	20		ring
C12	30	14		ring	21		ring
C13	31	15		ring	19		ring
C14	32	16		ring-CH_3	17		ring
H6	38	17		ring	11		-CH_3
H7	39	18		ring	10		-CH_3
H8	40	19		-CH_3	12		-CH_3
H9	41	20		-CH_3	14		ring
H10	42	21		-CH_3	13		ring

Table A.5: Mapping Tetryl site notation from published crystal structure[260] to this work. Also shown are optimized structures N site numbers. The approximate rotation of nitro groups in degrees is shown in parenthesis.

crystal	this work		position
	(crystal)	(opt)	
C(1)	1		ring
C(2)	2		ring
C(3)	3		ring
C(4)	4		ring
C(5)	5		ring
C(6)	6		ring
C(7)	7		ring
N(1)	$8(25^o)$	$8,9(35^o)$	ring-NO_2
N(2)	$9(23^o)$	$12(0^o)$	p,ring-NO_2
N(3)	$10(44^o)$	$8,9(35^o)$	ring-NO_2
N(4)	11	1	ring-N-
N(5)	$12(65^o)$	$19(0^o)$	-NO_2
O(1)	13		ring-NO_2
O(2)	14		ring-NO_2
O(3)	15		ring-NO_2
O(4)	16		ring-NO_2
O(5)	17		ring-NO_2
O(6)	18		ring-NO_2
O(7)	19		-NO_2
O(8)	20		-NO_2
H(1)	21		ring-H
H(2)	22		ring-H
H(3)	23		ring-N-CH_3
H(4)	24		ring-N-CH_3
H(5)	25		ring-N-CH_3

APPENDIX B

LETTER OF PERMISSION

ACS PUBLICATIONS DIVISION GUIDELINES
FOR THESES AND DISSERTATIONS
ATTN: STUDENTS, STUDENT ADVISORS, AND TEACHERS

Permission is now automatically granted to include your paper(s) or portions of your paper(s) in your thesis; please pay special attention to the implication paragraph below. The Joint Board/Council Committees on Copyrights and Publications recently approved the following:

Copyright permission for published and submitted material from thesis and dissertations ACS extends blanket permission to students to include in their theses and dissertations their own articles, or portions thereof, that have been included in ACS journals or submitted to ACS journals for publication, provided that the ACS copyright credit line is noted on the appropriate page(s).

Publishing implications of electronic publication of theses and dissertation material Students and their mentor should be aware that posting of theses and dissertation material on the Web prior to submission of material from that thesis/dissertation to an ACS journal may affect publication in that journal. Whether Web posting is considered prior publication may be evaluated on a case-by-case basis by the journal's editor. If an ACS journal editor considers Web posting to be "prior publication", the paper will not be accepted for publication in that journal.

If your paper has not yet been published by ACS, we have no objection to your including part or all of it in your theses in print and microfilm formats; please note, however, that electronic distribution or Web posting of the unpublished paper as part of your thesis in electronic formats might jeopardize publication of you paper by ACS. Please print the following credit line on the first page of your article: "Reproduced (or 'Reproduced in part') with permission from [JOURNAL NAME], in press (or 'submitted for publication'). Unpublished work copyright [CURRENT YEAR] American Chemical Society." Include appropriate information.

If your paper has already been published by ACS and you want to include part or all of it in your thesis or dissertation, please print the ACS copyright credit line on the first page of your article: "Reproduced (or 'Reproduced in part') with permission from [FULL REFERENCE CITATION.] Copyright [YEAR] American Chemical Society." Include appropriate information.

Note: If you plan to submit your thesis to UMI or to another dissertation distributor, you should not include the unpublished ACS paper in your thesis if the thesis will be disseminated electronically, until ACS has published your paper. After publication of the paper by ACS, you may release the entire thesis for electronic dissemination. ACS's copyright credit line should be printed on the first page of the ACS paper.

Permission is not granted to post any published or unpublished ACS articles on any Web site.

Questions? Call ACS Publications Division Copyright Office staff at 202/872-4368, or e-mail us at copyright@acs.org.

VITA

On February 1, 1974, Chris Robert Harwell was born in Oldsmar, Florida. Chris attended Oldsmar Elementary, Safety Harbor Middle and East Lake High School. In 1985 he became a member of the Boy Scouts of America, where he worked his way to Eagle Scout in 1991 by building a playground for the Oldsmar Community United Method Church. In June 1992, he graduated from East Lake High School. He won a Presidential Scholarship from High Point University, located in the furniture and hosiery capital of the world, High Point, North Carolina. During the summer of 1995 in Baton Rouge, Louisiana, he first got a taste of computational chemistry at a National Science Foundation Research Experience for Undergraduates held at Louisiana State University. He graduated from High Point University *magna cum laude* in May 1996, majoring in chemistry and minoring in math. In August 1996, he accepted a Board of Regents Fellowship to attend graduate school at Louisiana State University, where he is presently a candidate for the degree of Doctor of Philosophy in the Department of Chemistry.

In 1998 he was cited for Superior Performance and Productivity in Chemical Research by the Chemistry Department of Louisiana State University. During 1999 and 2000 he built a Beowulf parallel computer for the Chemistry Department using Linux, an open source operating system, and commodity off-the-shelf hardware.
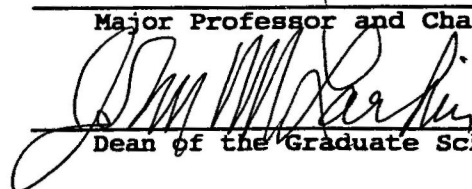
DOCTORAL EXAMINATION AND DISSERTATION REPORT

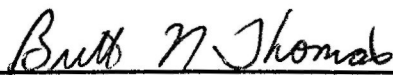**Candidate:** Chris Harwell

Major Field: Chemistry

Title of Dissertation: Theoretical Prediction of Nuclear Quadrupole Resonance Spectra of Aluminum, Bromine and Nitrogen Compounds Via First Principles Calculations

Approved:

_____
Major Professor and Chairman

_____
Dean of the Graduate School

EXAMINING COMMITTEE:

_____

_____

_____

_____

_____

_____

_____

Date of Examination:

June 13, 2000